

**CATALYTIC PARAMETERS FOR PHENOL
HYDROXYLATION AND ARYLBORONIC ACID
HOMOCOUPLING**



**A Thesis Submitted in Partial Fulfillment of the Requirements for the
Degree of Doctor of Philosophy in Chemistry
Suranaree University of Technology
Academic Year 2014**

ปัจจัยที่มีผลต่อการเร่งปฏิกิริยาการเติมหมู่ไฮดรอกซิลบนพีนอล
และการเกิดโซโม่คัปปลิงของกรดแอริลโบโรนิก



วิทยานิพนธ์นี้เป็นส่วนหนึ่งของการศึกษาตามหลักสูตรปริญญาวิทยาศาสตรดุษฎีบัณฑิต
สาขาวิชาเคมี
มหาวิทยาลัยเทคโนโลยีสุรนารี
ปีการศึกษา 2557

CATALYTIC PARAMETERS FOR PHENOL HYDROXYLATION AND ARYLBORONIC ACID HOMOCOUPLING

Suranaree University of Technology has approved this thesis submitted in partial fulfillment of the requirements for the Degree of Doctor of Philosophy.

Thesis Examining Committee

(Asst. Prof. Dr. Sanchai Prayoonpokarach)

Chairperson

(Assoc. Prof. Dr. Jatuporn Wittayakun)

Member (Thesis advisor)

(Asst. Prof. Dr. Thanaporn Manyum)

Member

(Asst. Prof. Dr. Juthamas Jitchareon)

Member

(Assoc. Prof. Dr. Nurak Grisdanurak)

Member

(Prof. Dr. Sukit Limpijumnong)

Vice Rector for Academic Affairs
and Innovation

(Assoc. Prof. Dr. Prapun Manyum)

Dean of Institute of Science

อสรุจรงค์ โสภิพันธ์ : ปัจจัยที่มีผลต่อการเร่งปฏิกิริยาการเติมหมู่ไฮดรอกซิลบนฟีนอลและการเกิดไฮโมคัปปลิงของกรดแอริลโบโรนิก (CATALYTIC PARAMETERS FOR PHENOL HYDROXYLATION AND ARYLBORONIC ACID HOMOCOUPLING)
อาจารย์ที่ปรึกษา : รองศาสตราจารย์ ดร.จตุพร วิทยาคุณ, 183 หน้า.

วัตถุประสงค์ของวิทยานิพนธ์นี้เพื่อเข้าใจคุณสมบัติของตัวเร่งปฏิกิริยาซึ่งมีส่งผลต่อประสิทธิภาพการเติมหมู่ไฮดรอกซิลบนฟีนอลและการเกิดไฮโมคัปปลิงของกรดแอริลโบโรนิก สำหรับการเติมหมู่ไฮดรอกซิลบนฟีนอล เหล็กเป็นตัวเร่งปฏิกิริยา ซีโอไลต์บีตา และเอ็มซีเอ็ม -22 ในรูปแอมโมเนียม (NH_4BEA และ $\text{NH}_4\text{MCM-22}$) และรูปโปรตอน (HBEA และ HMCM-22) เป็นตัวรองรับ โดยเติมเหล็กบนตัวรองรับซีโอไลต์โดยวิธีการทำให้เอิบซุ่ม วิธีการแลกเปลี่ยนไอออนในสถานะของเหลว และวิธีการผสมทางกายภาพ พบว่าปริมาณเหล็กที่เติมลงไปโดยวิธีการแลกเปลี่ยนไอออนในสถานะของเหลวเป็นเฟส Fe_2O_3 ซึ่งอยู่ภายในรูพรุนของซีโอไลต์ และมีปริมาณน้อยกว่าที่เติมโดยวิธีการทำให้เอิบซุ่มและวิธีการผสมทางกายภาพ โดยเหล็กบนตัวเร่งปฏิกิริยาที่เตรียมจากวิธีการทำให้เอิบซุ่มและการผสมทางกายภาพเป็นอนุภาคของ Fe_2O_3 กระจายบนผิวหน้าของซีโอไลต์จากการเร่งปฏิกิริยาการเติมหมู่ไฮดรอกซิลบนฟีนอล พบว่าตัวเร่งปฏิกิริยาที่เตรียมจากวิธีการแลกเปลี่ยนไอออนในสถานะของเหลวมีประสิทธิภาพในการเร่งปฏิกิริยาสูงสุด โดยมีอัตราการเร่งปฏิกิริยาเร็วที่สุด และมีการสูญเสียมวลน้อยที่สุดในการเกิดปฏิกิริยา มีค่าการแปลงผันของฟีนอลประมาณร้อยละ 55 - 65 และค่าจำเพาะต่อผลิตภัณฑ์ (แคทริคอลและไฮโดรควิโนน) รวมเท่ากับร้อยละ 70 ประสิทธิภาพที่ดีเยี่ยมของตัวเร่งปฏิกิริยาที่เตรียมได้จากวิธีการแลกเปลี่ยนไอออนในสถานะของเหลวมาจาก Fe_2O_3 ที่อยู่ภายในรูพรุนของซีโอไลต์

เพื่อศึกษาอิทธิพลของปริมาณอะลูมิเนียมในตัวรองรับ ได้กำจัดอะลูมิเนียมในซีโอไลต์บีตาโดยใช้กรดไนตริกเกิดเป็น D-BEA และเติมเหล็กเข้าไปในช่องว่างเตตระฮีดรัลที่เกิดขึ้นในตัวรองรับโดยวิธีการแลกเปลี่ยนไอออนในสถานะของเหลว การกำจัดอะลูมิเนียมมีผลทำให้เกิดการหดตัวของแลตทิซของซีโอไลต์ และการเติมเหล็กมีผลทำให้เกิดการขยายตัวกลับของแลตทิซ โดยส่วนมากเฟสของ Fe_2O_3 ใน D-BEA อยู่ที่ตำแหน่งการแลกเปลี่ยนไอออน อัตราการเกิดปฏิกิริยาการเติมหมู่ไฮดรอกซิลลดลงตามการเพิ่มขึ้น ของเวลาที่ใช้ในการกำจัดอะลูมิเนียมจนถึง 180 นาที

จากนั้นอัตราการเกิดปฏิกิริยาเพิ่มขึ้น ณ เวลาที่ใช้ในการกำจัดอะลูมิเนียมที่ 240 นาที เนื่องจากการรุกรานซีโอไลต์มีขนาดเพิ่มขึ้น เมื่อเปรียบเทียบกับตัวเร่งปฏิกิริยาเหล็กบนตัวรองรับซีโอไลต์บีตา พบว่าตัวเร่งปฏิกิริยาเหล็กบนตัวรองรับ D-BEA สามารถเพิ่มความจำเพาะต่อผลิตภัณฑ์แคทลิกอลและไฮโดรควิโนนเป็นร้อยละ 80 และมีการสูญเสียมวลน้อยที่สุดในการเกิดปฏิกิริยา

เพื่อเข้าใจสาเหตุของการสูญเสียมวลในปฏิกิริยาการเติมหมู่ไฮดรอกซิลบนพีนอล ตัวเร่งปฏิกิริยาที่ใช้เร่งปฏิกิริยาแล้วถูกนำศึกษาต่อโดยเทคนิคการเกิดออกซิเดชัน โดยที่มีการควบคุมการเปลี่ยนแปลงอุณหภูมิ ปริมาณ ไล่กจากการเกิดออกซิเดชัน โดยที่มีการควบคุมการเปลี่ยนแปลงอุณหภูมิมีความสอดคล้องอย่างดีกับการสูญเสียมวลของคาร์บอนจากปฏิกิริยา นอกจากนี้ปริมาณและธรรมชาติของโค้กขึ้นอยู่กับปริมาณเหล็กบนตัวเร่งปฏิกิริยา ซอฟโค้กเกิดจากตัวเร่งปฏิกิริยาที่เตรียมจากวิธีการทำให้เอิบซุ่มและวิธีการผสมทางกายภาพ นอกจากนี้ยังพบกรดอินทรีย์จากปฏิกิริยาออกซิเดชันของแคทลิกอล ไฮโดรควิโนน และเบนโซควิโนน โดยไฮโดรเจนเปอร์ออกไซด์ซึ่งทดสอบและยืนยันจากเทคนิค Attenuated total internal reflectance spectrometry (ATR) และเทคนิคโครมาโตกราฟีของเหลวสมรรถนะสูง (HPLC)

สุดท้ายนี้ การเกิดไฮโมคัปปลิงของกรดแอรลิโบโรนิกของตัวเร่งปฏิกิริยาอัลลอยด์นาโนคลัสเตอร์ของทองและแพลเลเดียมบนตัวรองรับโคโคซานถูกศึกษาพบว่าตัวเร่งปฏิกิริยา $Au_{0.81}Pd_{0.19}$:chit มีประสิทธิภาพในการเร่งปฏิกิริยาสูงกว่าเมื่อเปรียบเทียบกับตัวเร่งปฏิกิริยา Au:chit และจากความสัมพันธ์ของค่า Hammett แสดงให้เห็นว่าปฏิกิริยาเกิดผ่านกลไกแบบหลากหลายหรือมีความหลากหลายของตำแหน่งการเกิดปฏิกิริยาบนตัวเร่งปฏิกิริยานี้

สาขาวิชาเคมี ลายมือชื่อนักศึกษา _____

ปีการศึกษา 2557

ลายมือชื่ออาจารย์ที่ปรึกษา _____

ONSULANG SOPHIPHUN : CATALYTIC PARAMETERS FOR PHENOL
HYDROXYLATION AND ARYLBORONIC ACID HOMOCOUPLING.

THESIS ADVISOR : ASSOC. PROF. JATUPORN WITTAYAKUN, Ph.D.

183 PP.

IRON/ ZEOLITE BEA/ DEALUMINATED-BEA/ ZEOLITE MCM-22/ INCIPIENT
WETNESS IMPREGNATION/ LIQUID STATE ION EXCHANGE/ PHYSICAL
MIXING/ PHENOL HYDROXYLATION/ CHITOSAN/ GOLD-PALLADIUM/
OXIDATIVE HOMOCOUPLING OF ARYLBORONIC ACID.

The objective of this thesis was to understand properties of catalysts and influence the catalytic performance in phenol hydroxylation and oxidative homocoupling of arylboronic acid. For phenol hydroxylation, Fe was employed as an active metal; zeolite BEA and MCM-22 in ammonium form (NH_4BEA and $\text{NH}_4\text{MCM-22}$) and proton form (HBEA and HMCM-22) were used as supports. Fe was introduced onto the zeolite supports by incipient wetness impregnation (IWI), liquid state ion-exchange (LSIE) and physical mixing (PM). Fe loading in LSIE catalysts was much lower than that in IWI and PM catalysts with isolated Fe_2O_3 inside the pore of zeolite. The Form of Fe in IWI and PM catalysts was Fe_2O_3 particles on the external surface of zeolite. From the phenol hydroxylation testing, the catalyst prepared from LSIE was the most active as it gave the fastest reaction rate and the lowest mass loss. The conversion of phenol was about 55 - 65% while the product selectivity (CAT and HQ) was 70%. The superior property of the catalyst from LSIE came from the presence of isolated Fe_2O_3 inside the pore of zeolite. To further study

the influence of the Al content in support, the zeolite HBEA was dealuminated by HNO_3 producing D-BEA and replaced with Fe in the T-vacant site by LSIE method. The dealumination resulted in a contraction of the zeolite lattice and the Fe insertion resulted in an expansion. The isolated Fe_2O_3 at the ion-exchange position was favored on the D-BEA. The reaction rate decreased with the dealumination time until 180 min, then increased at the dealumination time of 240 min attributing to the opening of zeolite pore. Compared to Fe supported on BEA, the Fe supported on D-BEA raised the product selectivity (CAT and HQ) to 80% and reduced the mass loss.

To understand the cause of the carbon mass loss after phenol hydroxylation, the spent catalysts were studied by temperature programmed oxidation (TPO). The amount of coke from TPO was in good agreement with the carbon mass loss. The amount and nature of coke was depended on the Fe loading method. Softer coke was produced from IWI and PM catalysts. Besides the deep oxidation of CAT, HQ and BQ by H_2O_2 , formation of organic acids was suspected and then confirmed by Attenuated Total Internal Reflectance Spectrometry (ATR) and High Performance Liquid Chromatography (HPLC).

Finally, the homocoupling of arylboronic acid over bimetallic Au/Pd alloy nanoclusters stabilized by chitosan was studied. The catalyst $\text{Au}_{0.81}\text{Pd}_{0.19}:\text{chit}$ was the most active, particularly in comparison with monometallic Au:chit. The observed Hammett correlation indicates that the reaction is likely to occur by multiple mechanisms or multiple catalytic sites probably involved in bimetallic catalysis.

School of Chemistry

Student's Signature _____

Academic Year 2014

Advisor's Signature _____

ACKNOWLEDGEMENTS

Foremost, I would like to express my sincere gratitude to my advisor Assoc. Prof. Dr. Jatuporn Wittayakun for his patience, motivation and immense knowledge throughout the course of my graduate. His best wish and understanding are very much appreciated. Besides I am also very thankful to the thesis examining committee including Asst. Prof. Dr. Juthamas Jitchareon, Assoc. Prof. Dr. Nurak Grisdanurak, Asst. Prof. Dr. Sanchai Prayoonpokarach and Asst. Prof. Dr. Thanaporn Manyum.

For my research experience abroad, I would like to thank Prof. Dr. Hidehiro Sakurai and Dr. Raghu Nath Dhital at Institute for Molecular Science (IMS), Japan; Asst. Prof. Dr. Karin Föttinger, Dilek Demir and Astrid Wolfbeisser at Vienna University of Technology (TU), Austria; and members from both groups.

I would like to thank past and present research group members in Thailand including Nattawut Osakoo, Wina Rongchapo, Saowanee Manadee, Suriyan Rakmae, Chalermpan Kiewkamay, Dr. Piaw Pathai, Dr. Supattra Khabuanchalad, Dr. Kamolwan Rinramee, Sudarat Sombatsri, Narongrit Sosa, Krittanun Deekomwong and others for their help and friendship. Moreover, I would like to thank Dr. Sirinuch Loiha, Dr. Pongtanawat Khemthong and Dr. Sittichai Kulawong for teaching me the synchrotron techniques and phenol hydroxylation.

Furthermore, I would like to deeply thank my parents and family for their inspiration and love. Particularly, the special thanks for their warm and impressive encourage.

Importantly, the financial support from the Thai government under the Program Strategic Scholarships for Frontier Research through the Commission of Higher Education Commission. Additional support was from a cooperation research fund from JENESYS Programmed organized by the Japan Society for the Promotion of Science (JSPS).

Onsulang Sোধiphun



CONTENTS

	Page
ABSTRACT IN THAI.....	I
ABSTRACT IN ENGLISH.....	III
ACKNOWLEDGEMENTS.....	V
CONTENTS.....	VII
LIST OF FIGURES	XV
LIST OF TABLES	XXIII
LIST OF SCHEME.....	XXV
CHAPTER	
I INTRODUCTION.....	1
1.1 Research objectives	2
1.2 Scope and limitation of the study.....	3
II LITERATURE REVIEW.....	5
2.1 Hydroquinone.....	5
2.2 Synthesis of hydroquinone.....	6
2.3 Phenol hydroxylation.....	8
2.4 Catalyst for phenol hydroxylation.....	9
2.4.1 Supported Fe catalyst.....	11
2.4.2 Rice husk silica (RHS).....	15
2.4.3 Zeolite BEA.....	16

CONTENTS (Continued)

	Page
2.4.4 Zeolite MCM-22.....	18
2.4.5 Fe loading.....	19
2.5 References.....	20
III INFLUENCE OF IRON LOADING METHOD ON ZEOLITE BEA ON THE CATALYTIC PERFORMANCE IN PHENOL HYDROXYLATION.....	28
3.1 Abstract.....	28
3.2 Introduction.....	29
3.3 Experiment.....	31
3.3.1 Chemicals.....	31
3.3.2 Preparation of rice husk silica (RHS).....	31
3.3.3 Preparation of zeolite BEA.....	32
3.3.4 Preparation of supported Fe catalyst.....	32
3.3.5 Catalyst characterization.....	33
3.3.6 Catalytic testing on phenol hydroxylation.....	35
3.4 Results and discussion.....	37
3.4.1 Characterization of zeolite BEA and supported Fe catalysts	30
3.4.2 Catalytic performance of supported Fe catalysts in phenol hydroxylation	43
3.5 Conclusions.....	50
3.6 References.....	51

CONTENTS (Continued)

		Page
IV	INFLUENCE OF DEALUMINATION OF ZEOLITE BEA ON THE CATALYTIC PERFORMANCE IN PHENOL HYDROXYLATION.....	57
	4.1 Abstract	57
	4.2 Introduction.....	58
	4.3 Experiment.....	59
	4.3.1 Chemicals.....	59
	4.3.2 Dealumination of zeolite BEA.....	59
	4.3.3 Preparation of supported Fe catalysts.....	60
	4.3.4 Catalyst characterization.....	60
	4.3.5 Catalytic testing on phenolhydroxylation.....	61
	4.4 Results and discussion.....	61
	4.4.1 Characterization of dealuminated BEA and supported Fe catalysts.....	61
	4.4.2 Catalytic performance in phenol hydroxylation.....	66
	4.5 Conclusions.....	70
	4.6 References.....	71
V	INFLUENCE OF IRON LOADING METHOD ON ZEOLITE MCM-22 IN PHYSICOCHEMICAL PROPERTY AND CATALYTIC PERFORMANCE IN PHENOL HYDROXYLATION.....	75

CONTENTS (Continued)

	Page
5.1 Abstract.....	75
5.2 Introduction.....	76
5.3 Experiment.....	77
5.3.1 Chemicals.....	77
5.3.2 Preparation of zeolite MCM-22 supports.....	77
5.3.3 Preparation of supported Fe catalysts.....	78
5.3.4 Characterization of zeolite MCM-22 and supported Fe catalyst.....	79
5.3.5 Catalytic testing in phenol hydroxylation.....	79
5.4 Results and discussion.....	80
5.4.1 Characterization of zeolite MCM-22 and supported Fe catalysts.....	80
5.4.2 Catalytic performance in phenol hydroxylation.....	86
5.5 Conclusions.....	94
5.6 References.....	94
 VI	
STUDY OF MASS LOSS IN PHENOL HYDROXYLATION	
OOOVER IRON CATALYST SUPPORTED ON ZEOLITE	
MCM-22 BY ATTENUATED TOTAL INTERNAL	
REFLECTANCE WITH FOURIER TRANSFORM INFRARED	
SPECTROSCOPY.....	99
6.1 Abstract.....	99

CONTENTS (Continued)

	Page
6.2 Introduction.....	100
6.3 Experiment.....	101
6.3.1 Preparation of zeolite MCM-22 supports and supported Fe catalysts.....	101
6.3.2 Batch reactor for phenol hydroxylation.....	101
6.3.3 Instrument setting for ATR-FT-IR.....	102
6.3.4 Phenol adsorption by ATR-FT-IT technique.....	103
6.3.5 Phenol hydroxylation by ATR-FT-IR technique.....	103
6.4 Results and discussion.....	104
6.4.1 IR spectra for aromatic hydrocarbons.....	104
6.4.2 Phenol adsorption by ATR-FT-IR.....	107
6.4.3 Phenol hydroxylation on bare ZnSe monitored by ATR-FT-IR.....	108
6.4.4 Optimization the phenol hydroxylation for ATR-FT-IR techniques.....	109
6.4.4.1 Effect of catalyst content on the phenol hydroxylation under static condition.....	109
6.4.4.2 Effect of reaction condition on the phenol hydroxylation.....	110
6.4.4.3 Effect of flow rate of reactant mixture on the phenol hydroxylation.....	111

CONTENTS (Continued)

	Page
6.4.4.4 Effect of phenol/H ₂ O ₂ of reactant mixture on the phenol hydroxylation	112
6.4.4.5 Effect of reaction temperature on the phenol hydroxylation.....	113
6.4.5 The phenol hydroxylation by ATR-FT-IR technique over Fe supported catalyst on zeolite MCM-22.....	115
6.4.6 The oxidation of HQ, CAT and BQ by ATR-FT-IR technique over supported Fe catalyst on zeolite MCM-22	119
6.4.7 Change of solution pH after phenol hydroxylation in a batch reactor.....	120
6.4.8 Phenol hydroxylation analyzed by HPLC over Fe/HMCM-22-IWI on zeolite MCM-22.....	121
6.5 Conclusion	124
6.6 References.....	124
VII GOLD/PALLADIUM BIMETALLIC ALLOY NANOCCLUSERS STABILIZED BY CHITOSAN AS HIGHLY EFFICIENT AND SELECTIVE CATALYST FOR HOMOCOUPING OF ARYLBORONIC ACID.....	127
7.1 Abstract.....	127
7.2 Introduction.....	127
7.3 Experiment.....	129

CONTENTS (Continued)

	Page
7.3.1 Chemicals.....	129
7.3.2 Preparation of Au/Pd: chit.....	129
7.3.3 Characterization of Au/Pd:chit.....	130
7.3.4 Procedure for the homocoupling of arylboronic acid (1) by Au/Pd:chit.....	130
7.4 Results and discussion.....	131
7.4.1 Characterization of Au/Pd:chit	131
7.4.2 Catalytic performance of Au/Pd:chit in homocoupling of phenylboronic acid.....	135
7.5 Conclusions.....	141
7.6 References.....	142
VII CONCLUSION	146
APPENDICES	150
APPENDIX A CALIBRATION CURVE OF ELEMENTAL ANALYSIS BY ICP-OES TECHNIQUE.....	151
APPENDIX B CALIBRATION CURVE OF PRODUCTS AND REACTANCE FOR PHENOL HYDROXYLATION	156
APPENDIX C DATA FROM N ₂ ADSORPTION-DESORPTION...	163

CONTENTS (Continued)

	Page
APPENDIX D GOLD/PALLADIUM BIMETALLIC ALLOY NANOCLUSTERS STABILIZED BY CHITOSAN AS HIGHLY EFFICIENT AND SELECTIVE CATALYST FOR HOMOCOUPLING OF ARYLBORONIC ACID.....	176
CURRICULUM VITAE.....	183



LIST OF FIGURES

Figure	Page
2.1 Synthesis of HQ from various reagents. Conditions: (a) QP1.1/pKD12.138; (b) HOCl or $\text{Ag}_3\text{PO}_4/\text{K}_2\text{S}_2\text{O}_8$; (c) HNO_3 , H_2SO_4 ; (d) Cu/SiO_2 , H_2 ; (e) MnO_2 , H_2SO_4 ; (f) Fe^0 ; (g) prop-1-ene, HZSM-12; (h) (i) O_2 , NaOH, (ii) H_2SO_4 ; (i) HCO_2H , HCO_3H (Ran, David, Draths and Frost, 2001).....	6
2.2 Synthesis mechanism of HQ by Hock oxidation (Weissermel and Arpe, 2003).....	7
2.3 Phenol hydroxylation mechanism by Fe catalyst (Choi et al., 2006).....	9
2.4 Stereo view of the framework structure of polymorph A (left) and polymorph B (right) viewed along [010] and [110], respectively (Newsam, Treacy, Koetsier and Gruyter, 1998).....	16
2.5 Zeolite BEA in various forms A) sodium form B) ammonium form C) proton form.	18
2.6 The framework structure of zeolite MCM-22 (Leonowicz et al., 1994)	19
3.1 A) XRD patterns of NH_4BEA and HBEA , B) XRD patterns of supported Fe catalysts; $\text{Fe}/\text{MCM-22-IWI}$, $\text{Fe}/\text{HMCM-22-LSIE}$, $\text{Fe}/\text{NH}_4\text{MCM-22-LSIE}$ and $\text{Fe}/\text{HMCM-22-PM}$	38

LIST OF FIGURES (Continued)

Figure	Page
3.2 A) Nitrogen adsorption desorption isotherm of NH ₄ BEA and Fe/NH ₄ BEA-LSIE B) Nitrogen adsorption desorption isotherm of HBEA, Fe/HBEA-IWI, Fe/HBEA-LSIE and Fe/HBEA-PM.....	39
3.3 A) XANES spectra of Fe standards B) XANES spectra of Fe/HBEA, Fe/HBEA-LSIE, Fe/NH ₄ BEA-LSIE and Fe/HBEA-PM and Fe ₂ O ₃	40
3.4 DR-UV-Vis spectra of A) Fe/HBEA-IWI, B) Fe/HBEA-LSIE, C) Fe/NH ₄ BEA-LSIE and D) Fe/HBEA-PM	42
3.5 NH ₃ -TPD profiles of supported Fe catalysts.....	43
3.6 Phenol conversion during the phenol hydroxylation reaction at 70 °C with the reaction time of Fe/HBEA-IWI, Fe/HBEA-LSIE, Fe/NH ₄ BEA-LSIE B and Fe/HBEA-PM.....	46
3.7 Product yields during the phenol hydroxylation at 90 min of Fe/HBEA-IWI, Fe/HBEA-LSIE, Fe/NH ₄ BEA-LSIE and Fe/HBEA-PM.....	46
3.8 Images of fresh (1) and spent (2) catalyst for A) Fe/HBEA-IWI, B) Fe/HBEA-LSIE C) Fe/NH ₄ BEA-LSIE and D) Fe/HBEA-PM.....	47
3.9 CO ₂ temperature programmed oxidation of spent catalyst of Fe/HBEA-IWI, Fe/HBEA-LSIE, Fe/NH ₄ BEA-LSIE B and Fe/HBEA-PM catalysts.....	48

LIST OF FIGURES (Continued)

Figure	Page
3.10 FTIR spectra of spent catalyst in a series of zeolite BEA A) before the oxidation at 25 °C and B) after the oxidation at 450 °C.....	49
4.1 XRD patterns of A) D-BEA and B) Fe/D-BEA catalysts.....	62
4.2 DR-UV-Vis spectra of Fe/D-BEA catalysts.....	63
4.3 XANES spectra for A) Fe standards with different oxidation states B) Fe/D-BEA.....	64
4.4 NH ₃ -TPD profiles of A) D-BEA and B) Fe/D-BEA catalysts.....	66
4.5 Phenol conversions for Fe/D-BEA catalysts at A) 3 min and B) various times.....	67
4.6 Product yields during the phenol hydroxylation at 45 min of Fe/D-BEA-30, Fe/D-BEA-120, Fe/D-BEA-180 and Fe/D-BEA-240.....	69
4.7 Product yields during the phenol hydroxylation over Fe/HBEA-LSIE (from chapter III) and Fe-D-BEA-30 (this chapter).....	70
5.1 XRD patterns of zeolite MCM-22 and supported Fe catalysts: Fe/MCM-22-IWI, Fe/HMCM-22-LSIE, Fe/NH ₄ MCM-22-LSIE and Fe/HMCM-22-PM.....	81
5.2 N ₂ adsorption-desorption isotherms of A) NH ₄ MCM-22 and Fe/NH ₄ MCM-22-LSIE; B) HMCM-22, Fe/HMCM-22-IWI, Fe/HMCM-22-LSIE and Fe/HMCM-22-PM	82

LIST OF FIGURES (Continued)

Figure	Page
5.3 SEM images of A) HMCM-22, B) Fe/HMCM-22-IWI, C) Fe/HMCM-22-LSIE, D) Fe/HMCM-22-PM, E) NH ₄ MCM-22-LSIE and F) Fe/NH ₄ MCM-22-LSIE	83
5.4 DR-UV-Vis spectra of supported Fe catalysts: Fe/MCM-22-IWI, Fe/HMCM-22-LSIE, Fe/NH ₄ MCM-22-LSIE and Fe/HMCM-22-PM	84
5.5 A) XANES spectra of Fe standards: Fe, FeO, Fe ₃ O ₄ and Fe ₂ O ₃ , B) XANES spectra of supported Fe catalysts: Fe/MCM-22-IWI, Fe/HMCM-22-LSIE, Fe/NH ₄ MCM-22-LSIE and Fe/HMCM-22-PM	85
5.6 Phenol conversions on the supported Fe catalysts at 70°C, phenol:H ₂ O ₂ mole ratio of 1:1 and stirring condition	87
5.7 Product selectivities during phenol hydroxylation at reaction time of 90 min.....	89
5.8 Color change of reaction solution during the phenol hydroxylation by a batch.....	90
5.9 Images of fresh (1) and spent (2) catalyst for A) Fe/HMCM-22-IWI, B) Fe/HMCM-22-LSIE C) Fe/NH ₄ MCM-22-LSIE and D) Fe/HMCM-22-PM.....	90

LIST OF FIGURES (Continued)

Figure	Page	
5.10	Temperature programmed oxidation profiles of spent supported Fe catalysts after one cycle of the phenol hydroxylation. Spent catalysts were calcined with the heating rate of 5 °C/min under the flowing of 3% O ₂ /Ar with the total flow rate 40 mL/min.....	92
5.11	FTIR spectra of spent catalyst in a series of zeolite BEA A) before the oxidation at 25 °C and B) after the oxidation at 450 °C.....	93
6.1	ATR-FT-IR setup: A) ZnSe on a preparation holder, B) catalyst coated on ZnSe, C) assembling of the ATR cell, D) ATR cell and E) positioning of ATR cell in the IR spectrometer.....	103
6.2	A) Aromatic hydrocarbon standards on catalyst coated IRE at 40 °C, B) reaction sample of phenol hydroxylation from batch process on bare ZnSe at 40 °C. The phenol hydroxylation condition: phenol/H ₂ O ₂ molar ratio of 1/1 under stirring of 700 rpm at 70 °C.....	105
6.3	IR spectra of organic acid solution by Abbas et al. (2008).....	106
6.4	Phenol adsorption on Fe/NH ₄ MCM-22 catalyst at 40 °C at different adsorption time in minute a) 0, b) 30, c) 60, d) 120, e) 180, f) 240 and g) 300 min.....	107
6.5	Phenol hydroxylation with phenol/H ₂ O ₂ of 1/3 on bare ZnSe at 40 °C the reaction time in minute a) 0, b) 30, c) 60, d) 120, e) 180, f) 240 and g) 300 min	108

LIST OF FIGURES (Continued)

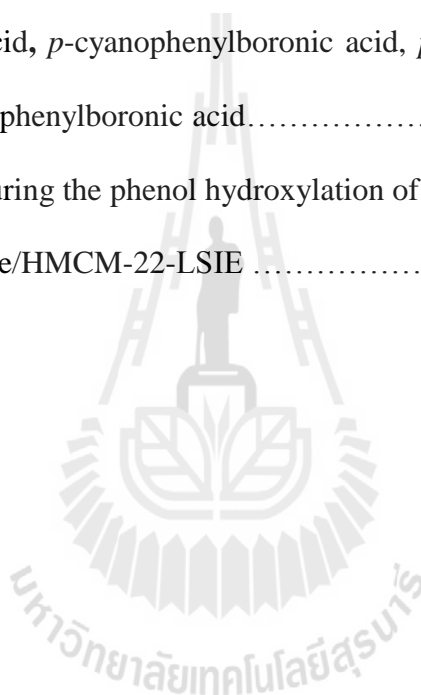
Figure	Page
6.6 Phenol hydroxylation on Fe/NH ₄ MCM-22-LSIE with phenol/H ₂ O ₂ of 1/3 under static condition at 40 °C with catalyst weight of A) 12.5 mg, B) 25.0 mg and C) 40.0 mg at the reaction time in minute: a) 0, b) 30, c) 60, d) 120, e) 180, f) 240 and g) 300 min	110
6.7 Phenol hydroxylation on Fe/NH ₄ MCM-22-LSIE with phenol/H ₂ O ₂ of 1/3 at 40 °C under A) static, B) flow condition at the reaction time in minute: a) 0, b) 30, c) 60, d) 120, e) 180, f) 240 and g) 300 min.....	111
6.8 Phenol hydroxylation with phenol/H ₂ O ₂ of 1/3 on Fe/NH ₄ MCM-22-LSIE catalyst at 40 °C under flow condition with the flow rate of A) 0.5 mL/min, B) 0.1 mL/min and C) 0.05 mL/min at the reaction time in minute: a) 0, b) 30, c) 60, d) 120, e) 180, f) 240 and g) 300 min.....	112
6.9 Phenol hydroxylation on Fe/NH ₄ MCM-22-LSIE at 40 °C under flowing condition with the phenol/H ₂ O ₂ ratio of reactant mixture A) 1:1 and B) 1:3 at the reaction time in minute: a) 0, b) 30, c) 60, d) 120, e) 180, f) 240 and g) 300 min.....	113
6.10 Phenol hydroxylation on Fe/NH ₄ MCM-22-LSIE with the phenol/H ₂ O ₂ molar ratio of 1/1 under flowing condition at the reaction temperature of A) 40 °C and B) 70 °C at the reaction time a) 0, b) 15, c) 30, d) 45, e) 60, f) 75 and g) 90 h) 105 and i) 120 min	114

LIST OF FIGURES (Continued)

Figure	Page
6.11 Phenol hydroxylation under flowing condition at the reaction temperature of 40 °C on Fe supported catalyst at the reaction time in minute: a) 0, b) 30, c) 60, d) 120, e) 180, f) 240 and g) 300 min.	117
6.12 IR spectra for the oxidation of the reaction intermediates by H ₂ O ₂ with the phenol/H ₂ O ₂ molar ratio of 1 at 40 °C under flowing condition 0.1 ml/min using Fe/NH ₄ MCM-22 as catalyst A) HQ B) CAT and C) BQ at the reaction time in minute: a) 0, b) 30, c) 60, d) 120, e) 180, f) 240 and g) 300 min.	120
6.13 Chromatogram of standards for phenol hydroxylation.....	122
6.14 Chromatogram of reaction mixture from phenol hydroxylation in a batch reactor at different reaction times.....	123
7.1 Uv-vis absorption spectra of A) Au _{0.91} Pd _{0.09} :chit, Au _{0.86} Pd _{0.14} :chit Au _{0.81} Pd _{0.19} :chit in reference with Au:chit, B) Au _{0.77} Pd _{0.23} :chit and Au _{0.72} Pd _{0.28} :chit in reference with Au:chit.....	133
7.2 Transmission electron microscopy images of (a) Au _{0.91} Pd _{0.09} :chit (b) Au _{0.86} Pd _{0.14} :chit (c) Au _{0.81} Pd _{0.19} :chit (d) Au _{0.77} Pd _{0.23} :chit (e) Au _{0.72} Pd _{0.28} :chit.....	134
7.3 UV-Vis absorption spectra of (a) Au _{0.60} Pd _{0.40} :chit, freshly prepared and after one day, (b) Au _{0.50} Pd _{0.50} :chit, freshly prepared and after one day.....	135

LIST OF FIGURES (Continued)

Figure	Page
7.4 The relationship between reaction rates of oxidative homocoupling of phenylboronic acid (1a) by a series of bimetallic Au/Pd nanoparticles	138
7.5 Hammett plot for homocoupling of substituted arylboronic acids; <i>p</i> -methyl phenylboronic acid, <i>p</i> -methoxyphenylboronic acid, phenylboronic acid, <i>p</i> -cyanophenylboronic acid, <i>p</i> -chlorophenylboronic acid and <i>p</i> -fluorophenylboronic acid.....	141
8.1 Product yields during the phenol hydroxylation of Fe/HBEA-LSIE, Fe/D-BEA and Fe/HMCM-22-LSIE	148



LIST OF TABLES

Table	Page
3.1 Fe contents and N ₂ adsorption-desorption analysis results of synthesized zeolite BEA and supported Fe catalysts.....	37
3.2 Linear combination fitting results of supported Fe catalysts.....	40
3.3 Product selectivity at various reaction times of supported Fe catalysts	45
3.4 Characteristic of infrareds assignments.....	49
4.1 Details of <i>d</i> ₃₀₂ spacing.....	62
4.2 Linear combination fitting results Fe/D-BEA	65
4.3 Product selectivity during the phenol hydroxylation.....	68
5.1 Fe contents and N ₂ adsorption-desorption analysis results of synthesized MCM-22 zeolite and supported Fe catalysts	80
5.2 Linear combination fitting results and pre-edge data of supported Fe catalysts.....	86
5.3 Phenol conversions and product selectivity at various reaction times of supported Fe catalysts.....	88
5.4 Characteristic of infrareds assignments.....	93
6.1 Characteristic of infrareds assignments of phenolic compounds.....	106
6.2 Results of phenol hydroxylation and pH value of the reaction mixture	121
6.3 Retention time of standards for phenol hydroxylation from chromatogram.....	122

LIST OF TABLES (Continued)

Table	Page
7.1 Calculated and actual Au and Pd fraction, mean cluster size, rate constant (k) and rate constant by surface area (k').....	132
7.2 Oxidative homocoupling of various <i>para</i> -substituted arylboronic acids catalyzed by Au _{0.81} Pd _{0.19} :chit	139



LIST OF SCHEMES

Scheme	Page
4.1 Dealumination of zeolite BEA and insertion of Fe by LSIE, adapted from Tang et al. (2014).....	59
6.1 Proposed phenol hydroxylation by Fenton's reagent by Zazo et al. (2005).....	118



CHAPTER I

INTRODUCTION

The overall objective of this thesis was to understand the properties of catalysts in terms of their activity and selectivity in the reactions. This thesis was divided into 4 main parts. The first part involved the investigation of the influence of the iron loading method on zeolite BEA and MCM-22 on the physicochemical properties and catalytic performance in phenol hydroxylation, particularly, to improve hydroquinone selectivity. The catalysts for the reaction were iron (Fe) supported on zeolite BEA and MCM-22. This part involved the synthesis of both zeolites by hydrothermal method. Both of zeolites in ammonium form (NH_4BEA and $\text{NH}_4\text{MCM-22}$) and proton form (HBEA and HMCM-22) were used in the preparation of catalysts that on which Fe was loaded by incipient wetness impregnation, liquid state ion exchange and physical mixing methods. The second part demonstrated the effect of dealumination of zeolite BEA to the phenol hydroxylation. The Fe was loaded on the dealuminated support by liquid state ion exchange method. The third part was the study on carbon mass loss of the iron catalysts supported on zeolite MCM-22 during phenol hydroxylation through the formation of coke and organic acids. The fourth part dealt with gold/palladium bimetallic alloy nanoclusters stabilized by chitosan as highly efficient and selective catalyst for homocoupling of arylboronic acid. A series of bimetallic Au/Pd alloy nanoclusters stabilized by chitosan were prepared and used as catalysts. The effect of ratio of Au/Pd alloy nanoclusters was studied on the catalytic activity and selectivity.

Besides their action mechanism was proposed according to the catalytic results. The catalysts from both parts were characterized by several techniques to obtain necessary information for explaining their roles in the reaction.

1.1 Research objectives

- 1.1.1 To prepare and characterize zeolite BEA and MCM-22.
- 1.1.2 To load Fe onto zeolite BEA and MCM-22 by incipient wetness impregnation (IWI), liquid state ion exchange (LISE) and physical mixing (PM) methods for use as catalysts for phenol hydroxylation.
- 1.1.3 To study the effect of supports and catalyst preparation methods to improve hydroquinone selectivity.
- 1.1.4 To study the effect of dealumination of zeolite BEA on phenol hydroxylation.
- 1.1.5 To study the formation of coke on the spent catalysts by temperature programmed oxidation technique (TPO).
- 1.1.6 To study the formation of organic acids during the phenol hydroxylation by attenuated total internal reflectance with Fourier transformed infrared spectroscopy (ATR-FT-IR).
- 1.1.7 To prepare a series of bimetallic Au/Pd alloy nanoclusters stabilized by chitosan for use as catalysts for homocoupling of arylboronic acid.
- 1.1.8 To study the effect of Au/Pd ratio to enhance the catalytic activity.

1.2 Scope and limitation of the study

- 1.2.1 Rice husk silica was used in the NaBEA synthesis. It was extracted from rice husk through a hydrochloric treatment, calcined at 550 °C and dissolved in NaOH solution to produce sodium silicate.
- 1.2.2 Both NaBEA and NaMCM-22 were synthesized by hydrothermal methods according to the procedures described by Loiha, Prayoonpokarach, Songsiriritthigun and Wittayakun (2009) and Corma, Corell and Parez-Pariente (1995).
- 1.2.3 The dealumination of zeolite BEA was carried out by HNO₃ treatment according to the procedure done by Baran, Millot, Onfroy, Krafft and Dzwigaj (2012).
- 1.2.4 The zeolite supports and catalysts were characterized by several techniques including XRD, ICP-OES, N₂ adsorption desorption, XANES, DR-UV-Vis and NH₃-TPD techniques. The spent catalysts were studied by TPO, TPO-FTIR techniques.
- 1.2.5 The phenol hydroxylation was carried out in a batch reactor using the following condition: temperature, 70 °C; catalyst amount, 0.05 g; mole ratio of phenol/H₂O₂, 1/1 and solvent, H₂O₂ under stirring. The reaction mixture was analyzed by gas chromatography with flame ionized detector and high performance liquid chromatography techniques.
- 1.2.6 The phenol hydroxylation was carried out by ATR-FT-IR measurement with various conditions.
- 1.2.7 The bimetallic Au/Pd alloy nanoclusters stabilized by chitosan were characterized by UV-Vis and HR-TEM.

1.2.8 The homocoupling of arylboronic acid was performed in a batch reactor using the following condition: temperature, 30 °C; catalyst amount, 2 atom % Au/Pd alloy nanoclusters stabilized by chitosan and acetate buffer pH 4.0 under stirring. The crude product was purified by PTLC and further analyzed by $^1\text{H-NMR}$.



CHAPTER II

LITERATURE REVIEW

2.1 Hydroquinone

Hydroquinone (HQ; 1,4-dihydroxybenzene) is an aromatic organic compound having a white crystalline with the chemical formula $C_6H_4(OH)_2$. It has two hydroxyl groups bonded at a *para* position of the benzene ring. HQ often coexists with catechol (1,2-dihydroxybenzene, CAT), an *ortho* position isomer (Cui, He and Zhao, 1999). However, HQ is industrially more important than CAT (Weissermel and Arpe, 2003). HQ is used extensively as a reducing agent in black and white photography, lithography and x-ray films; as an antioxidant in the manufacture of rubber; as a polymerization inhibitor for acrylic acid, vinyl acetate, methyl methacrylate monomer, and other monomers those are susceptible to radical-initiated polymerization (Roza, Vogel and Delft, 2003). Moreover, the disodium diphenolate salt of HQ is used as an alternating comonomer in a production of the poly etheretherketone (PEEK) polymer. For human medicine, HQ is used as an ingredient of dermatologic preparations for hyperpigmented area treatment (Briganti, Camera and Picardo, 2003).

Several utilizations reflect that HQ is one of the important chemicals that have gained interest from many researchers. There are a lot of efforts on catalyst synthesis development for improving the phenol conversion and HQ selectivity.

2.2 Synthesis of hydroquinone

HQ can be found in nature as a natural antioxidant in many foods, as the glucose conjugate arbutin and as free HQ in plants or plant-derived products (Deisinger, Hill and English, 1996). Moreover, it occurs in cigarette smoke (Hoffmann and Wynder, 1986). HQ can be synthesized from benzene through various chemical reactions as shown in Figure 2.1.

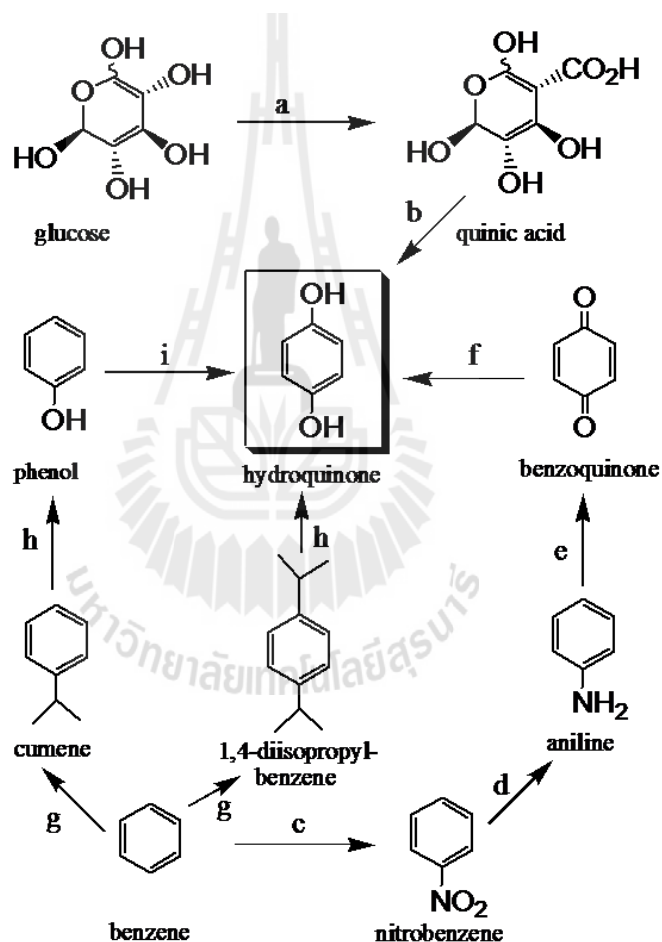


Figure 2.1 Synthesis of HQ from various reagents. Conditions: (a) QP1.1/pKD12.138; (b) HOCl or $\text{Ag}_3\text{PO}_4/\text{K}_2\text{S}_2\text{O}_8$; (c) HNO_3 , H_2SO_4 ; (d) Cu/SiO_2 , H_2 ; (e) MnO_2 , H_2SO_4 ; (f) Fe^0 ; (g) prop-1-ene, HZSM-12; (h) (i) O_2 , NaOH, (ii) H_2SO_4 ; (i) HCO_2H , HCO_3H (Ran, Knop, Draths and Frost, 2001).

HQ can be synthesized by oxidation of aniline with a stoichiometric amount of MnO_2 or CrO_3 in a solution acidified with H_2SO_4 . Then, the obtained quinone is reduced to HQ by Fe^0 (Ran et al., 2001).

Besides, HQ can be synthesized by Hock oxidation of 1,4-diisopropylbenzene, byproduct obtained from cumene process (Ran et al., 2001). As shown in Figure 2.2, 1,4-diisopropylbenzene is oxidized to dihydroperoxide by oxygen molecule or NaOH and converted to acetone and HQ by acidic cleavage. In addition, HQ can be synthesized in high yield by oxidation of quinic acid, obtained from glucose fermented process with HOCl or $\text{Ag}_3\text{PO}_4/\text{K}_2\text{S}_2\text{O}_8$ (Ran et al., 2001).

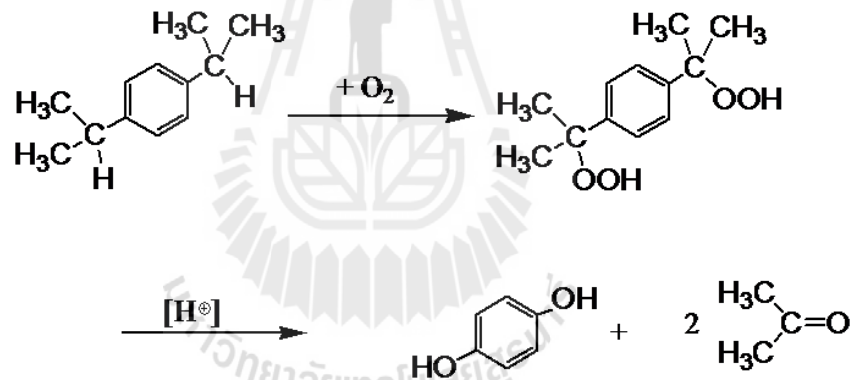


Figure 2.2 Synthesis mechanism of HQ by Hock oxidation (Weissermel and Arpe, 2003).

Another by-product of cumene process, isopropylbenzene can be oxidized to phenol in the same way with 1,4-diisopropylbenzene before converted to HQ. All HQ syntheses above require several steps and eliminations of by product salt stream can

increase the product cost and caused environmental problems. Industrially, HQ can be synthesized via the phenol hydroxylation by H_2O_2 as mentioned in the next section.

2.3 Phenol hydroxylation

Phenol hydroxylation has become an important industrial process to synthesize HQ and CAT. This process involves the reaction of phenol with H_2O_2 which is simple and environmental friendly. The reaction has been widely investigated using various homogenous and heterogeneous catalysts. Phenol is very reactive toward electrophilic aromatic substitution. The hydroxyl group of phenol is a strong electron donating group which can activate the *ortho*- and *para*- directing substitution to produce CAT and HQ, respectively (Dubey, Rives and Kannan, 2002). In general, the *ortho*-directing substitution is more favorable than the *para*-one.

The heterogeneous catalysts are preferred over the homogeneous ones because they give a high phenol conversion with high product selectivity and can be separated easily from the reaction mixture. Among several heterogeneous catalysts, supported Fe is widely used. In the reaction mechanism proposed by Choi, Yoon, Jang and Ahn, (2006), Fe is involved in the generation of hydroxyl radical ($\bullet\text{OH}$) known as Fenton type reaction. The hydroxyl radical is an electrophile which attacks at *ortho*- and *para*- positions of phenol to produce CAT and HQ. Moreover, HQ can be oxidized further to BQ by excess H_2O_2 . BQ is a kinetic product which gradually disappears with the reaction time.

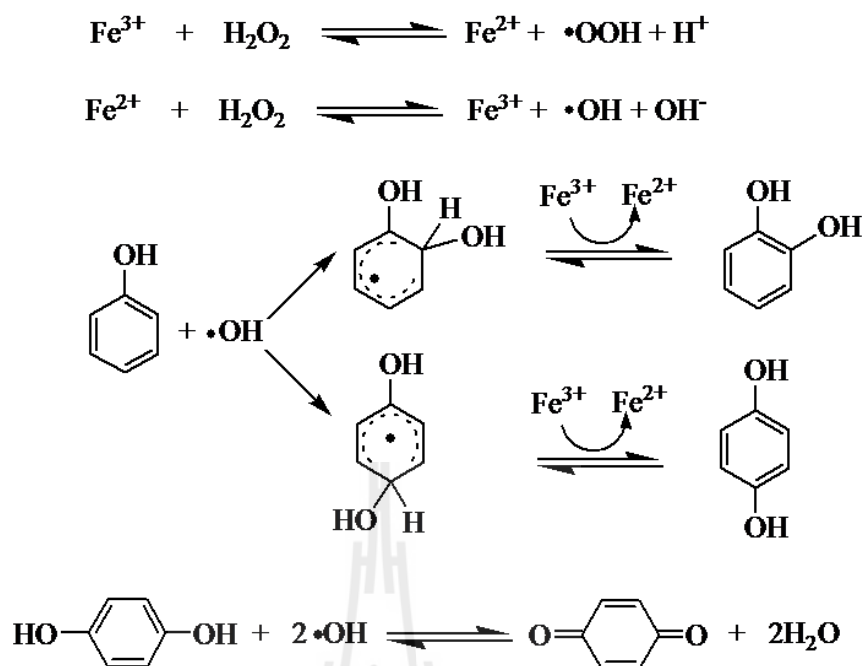


Figure 2.3 Phenol hydroxylation mechanism by Fe catalyst (Choi et al., 2006).

2.4 Catalysts of phenol hydroxylation

Several transition metals in various oxide forms have been used as catalysts for phenol hydroxylation based on their redox properties. Yu, Xiao, Wang, Sun, Liu, Pang, Feng, Qiu, Xu, and Fang (1999) studied the phenol hydroxylation over a novel complex oxide $\text{H}_x\text{V}_2\text{Zr}_2\text{O}_9\text{H}_2\text{O}$ with V^{4+} and V^{5+} mixed-valence and the V^{5+} species was suggested to be the active site. The reaction carried out at 80 °C for 6 h provided the phenol conversion of 13.6% with the selectivity of CAT and HQ of 60.0 and 35.3%, respectively. Mal and Ratnaswclq (1999) prepared Sn-silicailte-1 as a catalyst in phenol hydroxylation. At an optimum condition, the phenol conversion was less than 20% with the selectivity of CAT and HQ of 61.7 and 35.9%, respectively within 6 h. Noreña, Hernandez, Aguilar and Maubert (2002) studied the phenol

hydroxylation in acetonitrile media at 70 °C for 1 h by employing Cu-modified MCM-41 mesoporous catalysts. The catalyst with 30%wt Cu gave the highest HQ selectivity of 83.17% at moles of phenol converted per mole of copper of 7.13 but the activity was low. Dubey, Rives and Kannan (2002) carried out the phenol hydroxylation over ternary hydrotalcites (anionic clay) containing Cu, Ni and Al. Among the catalysts studied, CuNiAl3-5 ((Cu+Ni)/Al = 3.0, Cu/Ni = 5.0) showed the phenol conversion of 23.7% with the selectivity of CAT and HQ of 14.1 and 9.6%, respectively within 2 h. However, the presence of Ni and Al did not improve the reaction significantly. Liu, Ye, Zhan and Wu (1996) investigated the phenol hydroxylation catalyzed by iron(II) 1,10 - phenanthroline at 40 °C for 3 h. The catalyst showed the phenol conversion of 29.5% with the selectivity of CAT and HQ of 29.5 and 28.2%, respectively when water was a solvent. Abbo and Titinchi (2009) prepared Cu(II), Ni(II), Zn(II), Cr(II), Bi(II), Fe(III) and V(IV) ion-exchanged zeolite NaY and tested for phenol hydroxylation at 80 °C for 6 h. The catalysts demonstrated a range of activities depending on the metal center in the following order, V > Cr = Ni > Fe > Zn > Cu > Bi with different metal loading, the Fe(III)-NaY with the lowest metal loading showed a high phenol conversion and the highest HQ selectivity. They concluded that Fe(III)-NaY was the best catalyst to obtain high HQ yield.

From the literature reviews, Fe has been a catalyst of interest for the reaction over other metals because it gives high phenol conversion at mild reaction conditions and high product selectivity. Moreover, Fe is more environmental friendly than other solids containing oxidizing catalysts like Ni, Cu or V (Baldia, Escibano, Amores, Milella and Busca, 1998). There are several ways to improve the catalytic performance of Fe catalysts. In this work, the dispersion of Fe was improved by using

zeolite BEA and MCM-22 as supports. A higher dispersion resulted in higher active sites for the reaction.

2.4.1 Supported Fe catalyst

Letaïef, Casal, Aranda, Martin and Ruiz (2003) studied the phenol hydroxylation at 50 °C for 2 h by using Fe-Al-pillared clays (Fe-Al-PILCs) derived from two natural smectites: Wyoming SWy-1 and Tunisia-Gafsa VI (an iron-rich sample). The catalyst prepared from Tunisia-Gafsa VI gave the phenol conversion of 42% with CAT and HQ selectivity of 65 and 35%, respectively. Over the Fe³⁺ site in catalyst structure, the presence of Brønsted acid centers favors the transformation of Fe³⁺ to Fe²⁺ which is a Fenton type reaction and the •OH radicals are formed on Fe²⁺ species by reaction with the H₂O₂.

From the work by Li, Wu and Hu (2011), a series of microporous carbon-based catalysts for the phenol hydroxylation were prepared by acidification and/or oxidation treatment of a commercial carbon molecular sieve (CMS). Catalysts composed of CMS-I (non-modified CMS), CMS-Cl (CMS-I treated by 37% wt hydrochloric acid), CMS-N (CMS-I treated by 60% wt nitric acid), CMS-F (CMS-I treated by acid mixture composing of 47% wt hydrofluoric acid and 37% wt hydrochloric acid in 1:1 ratio (v/v)) and CMS-F(P) (CMS-F immersed in 30% wt H₂O₂). Among these CMSs catalysts, CMS-F(P) showed the highest activity, phenol conversion reached 29.6% and the selectivity to CAT and HQ were 47.6 and 37.5%, respectively. Although it contained 0.12% wt Fe, the surface acidity of CMSs is one of the important factor influencing their catalytic activities for the reaction.

Dai, Petty, Ingram and Szostak (1996) investigated the catalytic activities of FeAPO-11, ALPO₄-11 (aluminophosphate molecular sieve), SAPO-11 (silicon

aluminophosphate molecular sieve) and MgAPO-11 (magnesium-substituted aluminophosphate molecular sieve) for the phenol hydroxylation with H_2O_2 at 80 °C for 15 h. The FeAPO-11 was the most active one giving the phenol conversion of 26.2% with CAT and HQ selectivities of 51.1 and 48.9%, respectively. The superior performance of FeAPO-11 was attributed to the presence of Fe. Because the catalyst based on ALPO-11 gave a low phenol conversion and took a long reaction time, it was not suitable for the reaction. Other researchers studied the phenol hydroxylation by using Fe catalysts supported on other porous materials such as mesoporous silicas and zeolites.

Mesoporous silica presents regular arrayed of uniform channels along structure with pore size distribution in the range of 20 Å to 500 Å. The most common types are MCM-41 and SBA-15. Both materials present 2-dimensional hexagonally ordered mesopores but SBA-15 exhibits a larger pore size and interconnected through irregular small pores (Zhao, Huo, Feng, Chmelka and Stucky, 1998; Roth and Vartuli, 2005). Because of their uniform size and shape as well as thermal stability, the mesoporous silicas have gained considerable attention as catalysts and supports in various reactions including phenol hydroxylation.

Choi et al. (2006) synthesized Fe-MCM-41, in which Fe atoms were incorporated in the MCM-41 framework through a hydrothermal process. The Fe-MCM-41 was used as a catalyst for the phenol hydroxylation at the reaction temperature of 70 °C. For comparison, the reactions were carried out using $\text{FeO}_x/\text{MCM-41}$ (prepared from impregnation of Fe-salt on MCM-41), Fe-NPs (Fe_2O_3 nanoparticles) and Fe-NPs/SBA-15. The Fe-MCM-41 had a superior performance over other catalysts providing the phenol conversion of 60% with CAT and HQ

selectivities of 68 and 32%, respectively within 10 min. The FeO_x/MCM-41 gave a lower phenol conversion and longer reaction time than the Fe-MCM-41 indicating that octahedral extraframework Fe species was less active than tetrahedral coordinated one. In cases of Fe-NPs and Fe-NPs/SBA-15, they exhibited quite similar phenol conversions but took about 50 time longer reaction times than Fe-MCM-41. The Fe-NPs was covered by surfactant layer to prevent aggregation. The diffusion of substrates was hence hindered.

Zeolites are inorganic crystalline solids with aluminosilicate framework structures made from corner sharing SiO₄ and AlO₄ tetrahedral with small pores (1-20 Å in diameter) running throughout the solid. The presence of aluminum in zeolite framework gave negative charges in the zeolite structure which can be balanced by cations. If the cations are protons, they are called Brønsted acid sites. Furthermore, aluminums in zeolite also act as Lewis acid sites. Due to their porosity and acid properties, zeolites have been catalysts of interest for phenol hydroxylation.

Kulawong, Prayoonpokarach, Niramittagapong and Wittayakun (2011) synthesized NaMOR and modified it by acid leaching (AMOR), base leaching (BMOR) and both (ABMOR). All modified zeolites had increased surface area and were used as supports for 5% wt Fe catalyst in phenol hydroxylation at 70 °C for 1 h. A high Fe loading was obtained when Fe was loaded on all MOR samples, and the fastest reaction occurred on 5Fe/ABMOR with the highest phenol conversion of 60% and selectivity of CAT and HQ of 57.5 and 42.5%, respectively. Park et al. (2006) studied the phenol hydroxylation by using Fe-NaY, Co-NaY and Fe-Co-NaY catalysts. The Fe-Co-NaY was the best catalyst with phenol conversion of 21.8% and selectivity of CAT and HQ of 44.8 and 16.5%, respectively at 70 °C for 4 h. Villa,

Caro and Correa (2005) studied the effect of mineralizing agent (ammonium fluoride) in Fe-ZSM-5 synthesis through hydrothermal method. The obtained Fe-ZSM-5 with mineralizing agent (Fe-Z-f) was tested for the phenol hydroxylation at reaction temperature of 80 °C for 4 h in comparison with the Fe-ZSM-5 without mineralizing agent (Fe-Z-s). The Fe-Z-f catalyst had a superior activity with phenol conversion of 32.9% and selectivity of CAT and HQ of 60.5 and 39.5%, respectively. On the other hand, Fe-Z-s catalysts exhibited very low activity (less than 1% conversion). It was suggested that NH_4F in the synthesis gel was appropriate for the generation of Fe^{3+} in the zeolite framework and extraframework. In their work, the most active Fe-ZSM-5 catalyst contained extraframework iron.

Besides the above zeolites, BEA zeolite has been used as a catalyst for this reaction. Atoquchi, Kanougi, Yamamoto and Yao (2004) studied the phenol hydroxylation with H_2O_2 and H_2SO_4 over H-MFI, H-MOR, H-USY and H-BEA in the presence of diethyl ketone at 100 °C. The reactions without diethylketone were also investigated for comparison without diethyl ketone, the reaction yields (CAT+HQ) were in the order of H-BEA > H-USY >> H-MFI > H-MOR corresponding to a large pore and moderate strength of acid sites of H-BEA which could prevent a coke formation. The addition of diethyl ketone could improve the reaction yield and HQ selectivity for all zeolites. The yields reached 89.18% over H-BEA catalyst with the CAT and the HQ selectivities of 49.32 and 39.85%, respectively within 5 min.

Wang, Park, Wei and Lee (2003) investigated the phenol hydroxylation with hydrogen peroxide over Fe^{2+} , Co^{2+} ion-exchanged zeolite NaBEA. All catalysts showed high catalytic activity at room temperature within 3h. FeCoNaBEA was found to be an active and selective catalyst. The phenol conversion was 21% with CAT and

HQ selectivity of 51.4 and 17.6%, respectively at a molar ratio of phenol to hydrogen peroxide of 1:3 in an aqueous medium.

In case of zeolite MCM-22, it was expected to improve the HQ selectivity because of its narrow pore structure. To my knowledge, there exists no report on the utilization of zeolite MCM-22 in phenol hydroxylation. From the work by Sad, Padró and Apesteguía (2010), the gas-phase alkylation of phenol with methanol was studied on zeolite BEA, ZSM-5 and MCM-22. The particular pore structure of zeolite MCM-22 promoted the selective formation of *para*-cresol over other primary products of phenol methylation and drastically suppressed the consecutive reactions leading to secondary products.

According to the literature review above, the Fe incorporated zeolite BEA and zeolite MCM-22 in various forms are promising catalysts for the phenol hydroxylation with hydrogen peroxide.

2.4.2 Rice husk silica (RHS)

Thailand is an agricultural country where an abundance of rice is produced for consumption and export. Large quantities of rice husks are generated annually as a major byproduct in rice milling process. Rice husks contain about 13-29% of inorganic constituent, of which 87-97% is silica in an amorphous form (Shinohara and Kohyama, 2004). To extract silica from rice husks, the most widely used method is acid treatment followed by thermal treatment (Kurama and Kurama, 2008; Khemthong, Wittayakun and Preyoonpokarach, 2007). The RHS can be used as silica source for preparation of many porous material such as MCM-41 (Grisdanurak, Chiarakorn and Wittayakun, 2003), zeolite LSX (Khemthong et al., 2007), zeolite

ZSM-5 (Vempati, Borade, Hegde and Komarneni, 2006; Mohamed, Zidan and Tabet, 2008) and zeolite BEA (Loiha, Prayoonpokarach and Wittayakun 2009).

2.4.3 Zeolite BEA

Zeolite BEA is a high silica material with a large pore diameter of 0.76 nm×0.64 nm, first synthesized by Wadlinger, Kerr and Rosinski (1967) using tetraethylammonium hydroxide as templating agent. Its structure consists of an intergrowth of two polymorphs (Higgins, Lapierre, Schlenker, Rohrman, Wood, Kerr and Rohrbaugh, 1988). Polymorph A has space group $P4_122$ or $P4_322$, while polymorph B has space group $C2/c$. In both polymorphs, there are 12-membered ring pore system with three-dimensional and two straight channels. Each channel has a cross section of 0.76 nm × 0.64 nm, parallel to [100] and [010] and a tortuous channel of 0.55 nm × 0.55 nm, which runs along the [001] direction. The channel along [001] is formed by the intersection of the two linear channel systems. The framework density of BEA is 15.1 T/1000 Å³ and the ideal composition of the unit cell is Na⁺ [Al₇Si₅₇O₁₂₈]. In the BEA unit cell, nine different crystallographic sites for the T-atoms are present. The framework structures of the polymorphs A and B are shown in Figure 2.4.

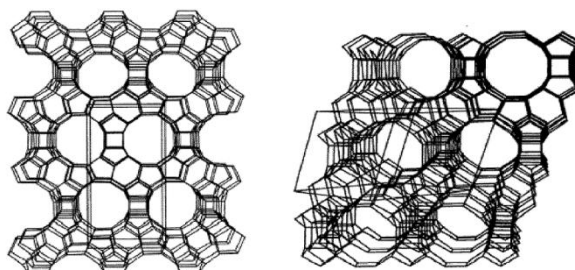


Figure 2.4 Stereo view of the framework structure of polymorph A (left) and polymorph B (right) viewed along [010] and [110], respectively (Newsam, Treacy, Koetsier and Gruyter, 1998).

Zeolite BEA can be synthesized from various silica sources including silica gel, fume silica, colloidal silica, tetraethylorthosilicate, etc. One of the most interested silica sources is RHS. Loiha et al. (2009) synthesized zeolite BEA from rice husk silica through a hydrothermal treatment at 135 °C and completed crystallization in 3 days. Tetraethylammonium hydroxide was also used as templating agent in the synthesis and the products with gel Si/Al ratios of 8-20 contained only the pure phase of BEA. The highest crystallinity and the largest crystal size were observed in the sample with the gel Si/Al ratio of 13. The obtained zeolite BEA in sodium form zeolite (NaBEA) could be ion-exchanged with ammonium nitrate aqueous solution to produce zeolite BEA in ammonium form (NH₄BEA). Further calcination of NH₄BEA produced zeolite BEA in proton form (HBEA). Figure 2.5 shows the comparison of zeolite BEA in various forms.

The NH₄BEA and HBEA exhibit different types and concentrations of structural Si-OH-Al groups (Bortnovsky, Melichar and Sobal, 2001) that might affect the efficiency of metal loading. Moreover, there is a report about the surface areas of the zeolite BEA in different forms (Amine, Akhtar and Rai, 2010). When the NH₄BEA was calcined to convert to HBEA, the surface area decreased 26.2% from its original ammonium form. Because the change in surface area might affect the metal dispersion, both NH₄BEA and HBEA are used as supports for Fe loading in this work.

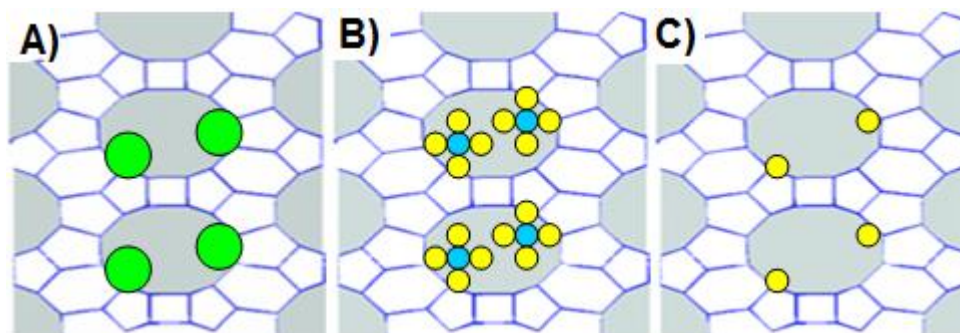


Figure 2.5 Zeolite BEA in various forms A) sodium form B) ammonium form C) proton form.

2.4.4 Zeolite MCM-22

In recent years, MCM-22 has been used as a promising catalyst for several organic reactions such as alkylation and isomerization (Sad et al., 2010). The structure of MCM-22 has been classified in MWW family according to the International Zeolite Association (IZA) structure commission. As shown in Figure 2.6, it has a pore structure that consists of two independent pore systems including the two dimensional channels with 10-membered ring openings and the large super cages of 12-membered ring with dimensions of $7.1 \text{ \AA} \times 7.1 \text{ \AA} \times 18.2 \text{ \AA}$. Both pore systems extend in the same direction but there is no direct access between these two pore systems (Leonowicz et al., 1994). MCM-22 is synthesized by using a hexamethyleneimine (HMI) as an organic template through hydrothermal method (Rubin and Chu, 1990). The obtained MCM-22 zeolites are very thin plates with large external surface area (Lawton, Leonowicz, Partridge, Chu and Rubin, 1998). Such pore structures of MCM-22 with narrow pore structures seem to be compatible with the structure of *para*-isomer. Thus, the utilization of MCM-22 is expected to improve the selectivity of HQ in the phenol hydroxylation.

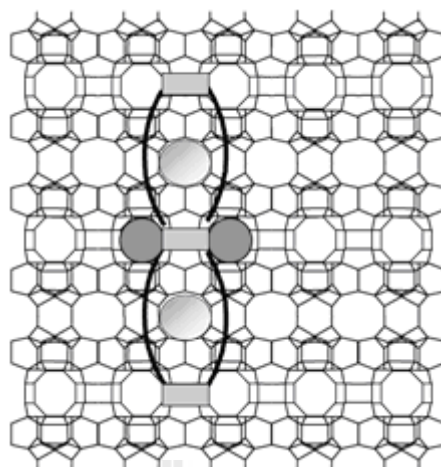


Figure 2.6 Framework structure of zeolite MCM-22 (Leonowicz et al., 1994).

2.4.5 Fe loading

There exist several techniques to incorporate Fe into zeolites. The most widely use methods are incipient wetness impregnation (IWI) and ion-exchange. In IWI method, a solution of metal precursor with a desired loading is dropped on the support before drying and calcination. The maximum loading is limited by the solubility of the precursor in the solution. It is a convenient method to prepare catalysts with high Fe loading but the higher loading can cause blocking of the zeolite pore which caused a decreasing of specific surface area (Balle, Geiger and Kureti, 2009). In liquid state ion-exchange method (LSIE), the cation in zeolite can be exchanged with Fe ions. The exchange capacity depends on the zeolite Si/Al ratio and this method is not suitable to prepare catalyst with high Fe loading. However, the method normally generates a strong metal-support interaction which leads to a high Fe dispersion (Lin, Schwartz and Butt, 1986). The zeolite is suspended in the solution of active metal precursor under agitation and heat condition. The counter cations (Na^+ , H^+ , NH_4^+) of zeolite framework are be replaced by the active metal ions (Bortnovsky

et al., 2001). There are many factors that affect the degree of ion-exchange. The first is steric constraints phenomena which is the formation of bulky hydration shells of the exchangeable cation. The other one is thermodynamic equilibrium which makes it necessary to repeat the exchange procedure several times to reach high exchange levels (Barrer, 1979). LSIE results in a strong metal-support interaction implying a good catalytic stability and a high metal dispersion leading to high amount of active sites for a reaction (Lin, Schwartz and Butt, 1986).

In physical mixing method (PM), the process is carried out by calcination the physical mixture of zeolite and active metal precursor at high temperature under atmosphere (Jia, Beaunier and Massiani, 1998) or flowing inert gas (He, Wang, Cheng, Lambert and Yang, 2009). The ion-exchange is taken place during the calcination. An advantage of PM is that a high metal loading is obtained in a one-step treatment.

2.5 References

- Abbo, H. S. and Titinchi, S. J. J. (2009). Di-, tri- and tetra-valent ion-exchanged NaY zeolite: Active heterogeneous catalysts for hydroxylation of benzene and phenol. **Applied Catalysis A: General**. 356: 167-171.
- Amin, N. A. S, Akhtar, J. and Rai, H. K. (2010). Screening of combined zeolite-ozone system for phenol and COD removal. **Chemical Engineering Journal**. 58: 520-527.
- Atoguchi, T., Kanougi, T., Yamamoto, T. and Yao, S. (2004). Phenol oxidation into catechol and hydroquinone over H-MFI, H-MOR, H-USY and H-BEA in the

- presence of ketone. **Journal of Molecular Catalysis A: Chemical**. 220: 183-187.
- Baldia, M., Escribano, V. S., Amores, J. M. G, Milella, F. and Busca, G. (1998). Characterization of manganese and iron oxide as combustion catalysts for propane and propene. **Applied Catalysis B: Environmental**. 17: L175-L182.
- Balle, P., Geiger, B. and Kureti, S. (2009). Selective catalytic reduction of NO_x by NH₃ on Fe/HBEA zeolite catalysts in oxygen-rich exhaust. **Applied Catalysis B: Environmental**. 85: 109-119.
- Barrer, R. M. (1979). **Zeolites and Clay Materials**. Academic Press, London.
- Bortnovsky, O., Melichar, Z. and Sobal, Z. (2001). Quantitative analysis of aluminium and iron in the framework of zeolites. **Microporous and Mesoporous Materials**. 46: 265-275.
- Briganti, S., Camera, E. and Picardo, M. (2003). Chemical and instrumental approaches to treat hyperpigmentation. **Pigment Cell Research**. 16: 101-110.
- Capek, L., Kreibich, V., Decek, J., De, Grygar, T., Wichterlova, B., Sobal, Z., Martens, J. A., Brosius, R. and Tokarova, V. (2005). Analysis of Fe species in zeolites by UV–VIS–NIR, IR spectra and voltammetry. Effect of preparation, Fe loading and zeolite type. **Microporous and Mesoporous Materials**. 80: 279-289.
- Centi, G., Genovese, C., Giordano, G., Katovic, A. and Perathoner, S. (2004). Performance of Fe-BEA catalysts for the selective hydroxylation of benzene with N₂O. **Catalysis today**. 91-92: 17-26.
- Choi, J-S., Yoon, S-S., Jang, S-H. and Ahn, W-S. (2006). Phenol hydroxylation using Fe-MCM-41 catalysts. **Catalysis Today**. 111: 280-287.

- Clearfield, A., Saldarriaga, C. H. and Buckley, R. C. (1973). J. B. Uytterhoeven (Ed.), Third International Conference on Molecular Sieves: 130, University of Leuven.
- Cui, H., He, C. X. and Zhao, G. W. (1999). Determination of polyphenols by high-performance liquid chromatography with inhibited chemiluminescence detection. **Journal of Chromatography A**. 855: 171-179.
- Dai, P-S. E., Petty, R. H., Ingram, C. W. and Szostak, R. (1996). Metal substituted aluminophosphate molecular sieves as phenol hydroxylation catalysts. **Applied Catalysis A: General**. 143: 101-110.
- Deisinger, P. J., Hill, T. S. and English, J. C. (1996). Human exposure to naturally occurring hydroquinone. **Journal Toxicological and Environmental Health**. 47: 31-46.
- Dubey, A., Rives, V. and Kannan, S. (2002). Catalytic hydroxylation of phenol over ternary hydrotalcites containing Cu, Ni and Al. **Journal of Molecular Catalysis A: Chemical**. 181: 151-160.
- Grisdanurak, N., Chiarakorn, S. and Wittayakun, J. (2003). Utilization of Mesoporous Molecular Sieves Synthesized from Natural Source Rice Husk Silica to Chlorinated Volatile Organic Compounds (CVOCs) Adsorption. **Korean Journal of Chemical Engineering**. 20: 950-955.
- He, C., Wang, Y., Cheng, Y., Lambert, C-K. and Yang, R. T. (2009). Activity, stability and hydrocarbon deactivation of Fe/Beta catalyst for SCR of NO with ammonia. **Applied Catalysis A: General**. 368: 121-126.

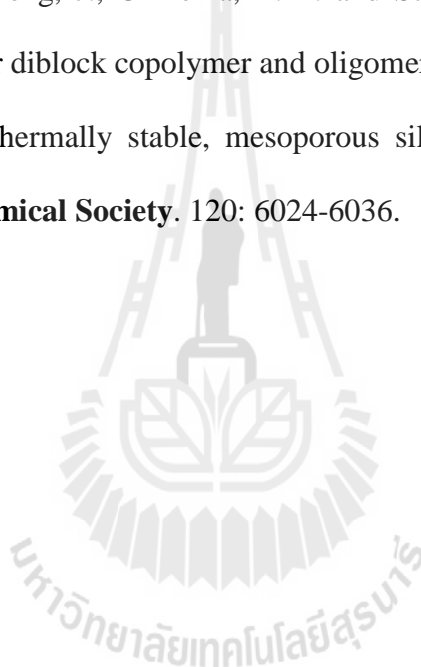
- Higgins, J. B., Lapierre, R. B., Schlenker, J. L., Rohrman, A. C., Wood, J. D., Kerr, G. T. and Rohrbaugh, W. J. (1988). The framework topology of zeolite beta. **Zeolites**. 8: 446-452.
- Hoffmann, D. and Wynder, E. L. (1986). Chemical constituents and bioactivity of tobacco. **IARC Scientific Publications**. 74: 145-165.
- Jia, C., Beaunier, P. and Massiani, P. (1998). Comparison of conventional and solid-state ion exchange procedures for the incorporation of lanthanum in H-beta zeolite. **Microporous and Mesoporous Materials**. 24: 69-82.
- Khemthong, P., Wittayakun, J. and Prayoonpokarach, S. (2007). Synthesis and characterization of zeolite LSX from rice husk silica. **Suranaree Journal of Science and Technology**. 14: 367-739.
- Kulawong, S., Prayoonpokarach, S., Neramittagapong, A. and Wittayakun, J. (2011). Mordenite modification and utilization as supports for iron catalyst in phenol hydroxylation. **Journal of Industrial and Engineering Chemistry**. 17: 346-351.
- Kurama, S. and Kurama, H. (2008). The reaction kinetics of rice husk based cordierite ceramics. **Ceramics International**. 34: 269-272.
- Lawton, S. L., Leonowicz, M. E., Partridge, R. D., Chu, P. and Rubin, M. K. (1998). Twelve-ring pockets on the external surface of MCM-22 crystals. **Microporous Mesoporous Materials**. 23: 109-117.
- Leonowicz, M. E., Lawton, J. A., Lawton, S. L. and Rubin, M. K. (1994). MCM-22: A molecular sieve with two independent multidimensional channel system. **Science**. 264: 1910-1913.

- Letaïef, S., Casal, B., Aranda, P., Martin-Luengo, M. A. and Ruiz-Hitzky, E. (2003). Fe-containing pillared clays as catalysts for phenol hydroxylation. **Applied Clay Science**. 22: 263-277.
- Li, S., Li, G., Li., Wu, G. and Hu, C. (2011). Microporous carbon molecular sieve as a novel catalyst for the hydroxylation of phenol. **Microporous and Mesoporous Materials**. 143: 22-29.
- Lin, T-A., Schwartz, L. H. and Butt, J. B. (1986). Iron alloy Fischer-Tropsch catalysis: V, Fe Co on Y. **Journal of Catalysis**. 97: 177-187.
- Liu, C., Ye, X., Zhan, R. and Wu, Y. (1996). Phenol hydroxylation by iron(II) phenanthroline: The reaction mechanism. **Journal of Molecular Catalysis A: Chemical**. 112: 15-22.
- Loiha, S., Prayoonpokarach, S., Songsiriritthigun, P. and Wittayakun, J. (2009). Synthesis of zeolite beta with pretreated rice husk silica and its transformation to ZSM-12. **Materials Chemistry and Physics**. 115: 637-640.
- Mal, N. K. and Ratnasweli, A. V. (1996). Hydroxylation of phenol over Sn-silicalite-1 molecular sieve: solvent effect. **Journal of Molecular Catalysis A**. 105: 149-158.
- Mohamed, M. M., Zidan, F. and Tabet, I. M. (2008). Synthesis of ZSM-5 zeolite from rice husk ash: Characterization and implications for photocatalytic degradation catalysts. **Microporous and Mesoporous Materials**. 108: 193-203.
- Najjar, W., Azabou, S., Sayadi, S. and Ghorbe, A. (2009). Screening of Fe-BEA catalysts for wet hydrogen peroxide oxidation of crude olive mill wastewater under mild conditions. **Applied Catalysis B: Environmental**. 88: 299-304.

- Newsam, J. M., Treacy, M. M. J., Koetsier, W. T. and Gruyter, C. B. De. (1998) Structural characterization of zeolite beta. **Proceeding of The Royal Society of London, Series A: Mathematical and Physical Sciences**. 420: 375-405.
- Noreña-Franco, L., Hernandez-Perez, I., Aguilar-Pliego, J. and Maubert-Franco, A. (2002). Selective hydroxylation of phenol employing Cu-MCM-41 catalysts. **Catalysis Today**. 75: 189-195.
- Park, J-N., Wang, J., Choi, K. Y., Dong, W-Y., Hong, S-I. and Lee, C. W. (2006). Hydroxylation of phenol with H₂O₂ over Fe²⁺ and/or Co²⁺ ion-exchanged NaY catalyst in the fixed-bed flow reactor. **Journal of Molecular Catalysis A: Chemical**. 247: 73-79.
- Rabo, J. A., Poutsma, M. L. and Skeel, G. W. (1973). J. W. High tower (Ed.) **Proceedings of the Fifth International Congress on Catalysis**. North-Holland, New York. 1353.
- Ran, N., Knop D. R., Draths, K. M. and Frost, J. W. (2001). Benzene-free synthesis of hydroquinone. **Journal of the American Chemical Society**. 123: 10927-10934.
- Roth, W. J. and Vartuli, J. C. (2005). Synthesis of mesoporous molecular sieves. **Studies in Surface Science and Catalysis**. 157: 91-110.
- Roza, L., de Vogel, N. and van Delft, J. H. (2003). Lack of clastogenic effects in cultured human lymphocytes treated with hydroquinone. **Food and Chemical Toxicology**. 41: 1299-1305.
- Rubin, M. and Chu, P. (1990). U. S. Patent 4,954,325.
- Sad, M. E., Padró, C. L. and Apesteguía, C. R. (2010). Study of the phenol methylation mechanism on zeolites HBEA, HZSM5 and HMCM22. **Journal of Molecular Catalysis A: Chemical**. 327: 63-72.

- Kumar, G. S., Saravanamurugan, S., Hartmann, M., Palanichamy, M. and Murugesan, V. (2007). Synthesis, characterisation and catalytic performance of HMCM-22 of different silica to alumina ratios. **Journal of Molecular Catalysis A: Chemical**. 272: 38-44.
- Shinohara, Y. and Kohyama, N. (2004). Quantitative analysis of tridymite and cristobalite crystallized in rice husk ash by heating. **Industrial Health**. 42: 277-285.
- Vempati, R. K., Borade, R., Hegde, R. S. and Komarneni, S. (2006). Template free ZSM-5 from siliceous rice hull ash with varying C contents. **Microporous and Mesoporous Materials**. 93: 134-140.
- Villa, A. L., Caro, C. A. and Correa, C. M. de. (2005). Cu- and Fe-ZSM-5 as catalysts for phenol hydroxylation. **Journal of Molecular Catalysis A: Chemical**. 228: 233-240.
- Villaseñor, J., Reyes, P. and Pecchi, G. (2002). Catalytic and photocatalytic ozonation of phenol on MnO₂ supported catalysts. **Catalysis Today**. 76: 121-131.
- Wadlinger, R. L., Kerr, G. T. and Rosinski, E. J. (1967). US Patent 3 308 069; reissued US Patent Re. 28 341 (1975).
- Wang, J., Park, J. N., Wei, X. Y. and Lee, C. W. (2003). Room-temperature heterogeneous hydroxylation of phenol with hydrogen peroxide over Fe²⁺, Co²⁺ ion-exchanged NaBEA zeolite. **Chemical Communications**. 7: 628-629.
- Weissermel, K. and Arpe, H. J. (2003). **Industrial Organic Chemistry Book**. Fourth Edition. Wiley-VCH.

- Wu, Y., Ren, X., Lu, Y. and Wang, J. (2008). Rapid synthesis of zeolite MCM-22 by acid-catalyzed hydrolysis of tetraethylorthosilicate. **Materials Letters**. 62: 317-319.
- Yu, R., Xiao, F. S., Wang, D., Sun, J., Liu, Y., Pang, G., Feng, S., Qiu, S., Xu, R. and Fang, C. (1999). Catalytic performance in phenol hydroxylation by hydrogen peroxide over a catalyst of V-Zr-O complex. **Catalysis Today**. 51: 39-46.
- Zhao, D., Huo, Q., Feng, J., Chmelka, B. F. and Stucky, G. D. (1998). Non ionic triblock and star diblock copolymer and oligomeric surfactant syntheses of highly ordered, hydrothermally stable, mesoporous silica structures. **Journal of the American Chemical Society**. 120: 6024-6036.



CHAPTER III

INFLUENCE OF IRON LOADING METHODS ON ZEOLITE BEA ON THE CATALYTIC PERFORMANCE IN PHENOL HYDROXYLATION

3.1 Abstract

The goal of this chapter was to investigate physicochemical properties and catalytic performance for phenol hydroxylation of Fe on zeolite BEA in proton (Fe/HBEA) and ammonium form (Fe/NH₄BEA). Fe was loaded on HBEA by methods were incipient wetness impregnation (IWI), liquid state ion exchange (LSIE) and physical mixing (PM). For comparison, Fe was loaded on NH₄BEA by LSIE. The Fe content in Fe/HBEA-LSIE and Fe/NH₄BEA-LSIE were 1.45 and 3.12 wt%, respectively, lower than that in Fe/HBEA-IWI and Fe/HBEA-PM. Surface area of all catalysts were about 600 m²/g except that of Fe/HBEA-PM which was 478 m²/g. The main form of Fe in Fe/HBEA-LSIE and Fe/NH₄BEA-LSIE was Fe₂O₃ inside the zeolite cavities whereas that in Fe/HBEA-IWI and Fe/HBEA-PM were large Fe₂O₃ particles on external surface. For phenol hydroxylation all catalyst gave phenol conversion about 60% with catechol as a major product. With lower Fe loading, the catalysts from LSIE were considered more active. The carbon deposition spent catalysts was further confirmed by temperature-programmed oxidation. With lower

amount of heavy coke, Fe/NH₄BEA-LSIE was more suitable than Fe/HBEA-LSIE for phenol hydroxylation.

3.2 Introduction

Catechol (CAT) and hydroquinone (HQ) are important chemicals which are synthesized industrially by phenol hydroxylation (Varagnat et al., 1976). The annual global production capacities for CAT and HQ were 30 kt/a and 55 kt/a, respectively (Clerici and Kholdeeva, 2013). By a catalyst with suitable properties, the yield of products and selectivity can be enhanced.

There are reports about utilization of zeolite BEA as a catalyst for phenol hydroxylation. Atoguchi et al. (2004) performed the reaction with hydrogen peroxide (H₂O₂) and sulfuric acid (H₂SO₄) over various zeolites in proton form including HMFI, HMOR, HUSY and HBEA in the presence of diethylketone at 100°C. The product yields (CAT+HQ) depended on the type of zeolite, namely, HBEA > HUSY >> HMFI > HMOR. The high performance of HBEA was attributed to a large pore size and moderate strength of acid sites which could prevent a coke formation. An addition of diethylketone could improve the reaction yield and HQ selectivity for all zeolites. The yields reached 89.18% over HBEA catalyst with the CAT and the HQ selectivities of 49.32 and 39.85%, respectively within 5 min.

Zeolite BEA was also used as a catalyst support. Wang et al. (2003) investigated phenol hydroxylation with H₂O₂ over Fe²⁺, Co²⁺ ion-exchanged zeolite NaBEA. All catalysts showed high catalytic activity at room temperature within 3h. At a mole ratio of phenol:hydrogen peroxide of 1:3 in an aqueous medium, FeCo/NaBEA was an active and selective catalyst providing the phenol conversion 21% with CAT and HQ

selectivity 51.4 and 17.6%, respectively. Despite several reports on catalytic performance of monometallic Fe on various supports for phenol hydroxylation, there is none on zeolite beta.

One of the most widely used methods to load Fe on zeolites is incipient wetness impregnation (IWI) in which a solution of a precursor with a desired amount of Fe is dropped on the support before drying and calcination. It is a convenient method to prepare catalysts with high Fe content but the higher loading can lead to the zeolite-pore blocking and lower surface area (Balle et al., 2009). Moreover, the maximum loading from IWI is limited by the solubility of the precursor. Another method is liquid state ion-exchange (LSIE) in which the zeolite is suspended in the solution of a metal precursor under agitation and heat. The zeolite charge balancing cation such as Na^+ , H^+ and NH_4^+ can be replaced by the metal ions (Bortnovsky et al., 2001). The exchange capacity is limited by the zeolite Si/Al ratio. Thus, a low Fe loading is obtained. The method normally gives high Fe dispersion due to a strong metal-support interaction (Lin et al., 1986). There are several factors affecting the degree of ion-exchange, for example, steric constraints from bulky hydration shells of the exchangeable cation and thermodynamic equilibrium which makes it necessary to repeat the exchange procedure many times to increase loading (Barrer, 1979). Moreover, physical mixing method (PM) can be carried out by calcination the physical mixture of zeolite and active metal precursor at high temperature under atmosphere (Jia et al., 1998) or flowing inert gas (He et al., 2009). The ion-exchange will take place during the calcination. An advantage of PM is that a high metal loading is obtained in a one-step treatment.

In this work zeolite NaBEA was synthesized using rice husk silica (RHS), transformed to HBEA and NH₄BEA and used as supports for Fe. The loading methods were IWI, LSIE and PM. Then the supported Fe catalysts were tested in phenol hydroxylation.

3.3 Experimental

3.3.1 Chemicals

Chemicals for preparation of zeolite BEA and supported Fe catalysts were concentrate HCl (37 %wt/wt, Carlo Erba), RHS, NaAlO₂ (55-56 wt%, Riedel-de Haën), NaOH (98 wt%, Prolabo), NaCl and KCl (Ajax Fine Chem), tetraethylammoniumhydroxide (TEAOH, 40 wt% in water, Alfa), NH₄NO₃ (99 wt%, Fluka) and Fe(NO₃)₃·9H₂O (99.9 wt%, QRëC). Chemicals for the phenol hydroxylation reaction testing were phenol (C₆H₅OH, 99.8%, BDH Prolabo), H₂O₂ (30 %wt/wt, Univar). Chemicals for the preparation of internal standard curve of the phenol hydroxylation were toluene (99.5% C₇H₈, QRëC™), phenol, pyrocatechol or CAT (C₆H₆O₂, 98 wt%, Fluka), hydroquinone or HQ (C₆H₆O₂, 99.8 wt%, Unilab) and 1, 4- benzoquinone or BQ (C₆H₄O₂, 99 wt%, ACRÖS Organic).

3.3.2 Preparation of rice husk silica

RHS with 98% purity was prepared by a procedure described from Wittayakun et al. (2008). The rice husks were from a local rice mill in Nakhon Ratchasima Province, Thailand. The 65 g of rice husks was refluxed with 125 mL of 3 M HCl at 65 °C for 6 h, decanted, washed with water until the filtrate was neutral, dried and calcined at 550 °C for 6 h producing RHS.

3.3.3 Preparation of zeolite BEA

Zeolite beta in sodium form (NaBEA) with a gel Si/Al ratio of 13 was synthesized by a method from the work of Loiha et al. (2009). Solution A was prepared by dissolving, 10 g of RHS in 15.11 mL of 0.14 M NaOH aqueous solution under a vigorous stirring. Solution B was prepared by dissolving, 0.61 g of NaAlO₂ in 5 mL of 0.14 M NaOH aqueous solution. Then, 6.77 mL of 0.45 M NaCl and 0.97 M KCl mixture alkali aqueous solution was mixed together with 29.42 mL of 40 wt% TEAOH in water before slowly added to solution A under vigorously stirring. The synthesis gel was stirred at room temperature for 24 h and crystallized under hydrothermal treatment in a Teflon-lined autoclave at 135 °C for 3 days. The NaBEA was separated, washed until neutral with DI water and dried at 100 °C overnight. Finally, the product was calcined to remove template at 550 °C for 6 h. The NaBEA was converted to NH₄BEA by ion-exchange three times with 20 wt% NH₄NO₃ solution at 80 °C for 8 h. The NH₄BEA was separated, washed and dried at 110 °C overnight. Some of dried NH₄BEA was calcined in air at 400 °C for 3 h to convert to HBEA.

3.3.4 Preparation of Supported Fe catalysts

Fe catalysts were loaded onto NH₄BEA and HBEA by incipient wetness impregnation (IWI), liquid state ion-exchange (LSIE) and physical mixing (PM) methods. Fe(NO₃)₃·9H₂O was used as Fe precursor. IWI was done according to a method from the literature (Balle et al., 2009). An Fe(NO₃)₃ aqueous solution was impregnated to HBEA with the wetness volume of 0.6 mL/g. The mixture was air dried at room temperature, at 110 °C for 6 h and calcined at 450 °C for 3 h. The obtained catalyst was named Fe/HBEA-IWI.

LSIE was carried out with a method from the literature (Dzwigaj et al., 2007). A 1.8×10^{-2} M $\text{Fe}(\text{NO}_3)_3$ aqueous solution was ion-exchanged with HBEA or NH_4BEA at room temperature for 24 h under stirring with the solution/solid ratio of 50 mL/g. The solid was separated by centrifugation, washed with DI water and dried overnight at 100 °C. The obtained solid was named Fe/HBEA-LSIE and Fe/ NH_4BEA -LSIE, respectively. The Fe/HBEA-LSIE was further calcined at 450 °C for 3 h.

PM was conducted with a method from the literature (Capek et al., 2005). Powder of $\text{Fe}(\text{NO}_3)_3 \cdot 9\text{H}_2\text{O}$ and HBEA were ground with a mortar and pestle for 20 min. The obtained solid was calcined at 550 °C for 6 h under an air flow rate of 50 mL/min, cooled down, washed with DI water and dried at 110 °C overnight. The obtained catalyst was named Fe/HBEA-PM.

3.3.5 Catalyst characterization

Fe content in each catalyst was determined by ICP-OES (PerkinElmer Optima 8000). The samples were prepared by microwave digestion (CEM, MAR5 model) through a method for zeolite. Firstly, samples were digested in the mixture of 37% HCl, 48% HF and 65% HNO_3 with the volumetric ratio of 2:1:3 at 210 °C for 15 min under the pressure of 896.3 kPa. Then 4% boric acid was added to the mixture with the volumetric ratio of 15 and continuously digested at 170 °C for 5 min under the pressure of 689.5 kPa. The digested sample solutions were diluted with 2% HNO_3 for ICP-OES measurement. Calibration curve for ICP-OES analysis could be found in Appendix A. The optical emission of Fe was monitored at wavelength 238.204 nm. Standard calibration curve of Fe was created to quantify the Fe content.

Powder X-ray diffraction (XRD) patterns were recorded on a Bruker AXS D5005 diffractometer using Cu K α radiation with nickel filtered at 40 mA and 40 kV in the 2 θ range of 5°-50° with an increment of 0.02° and the scan speed of 1s/step.

N₂ adsorption-desorption isotherms were obtained from a BELSORP mini II. Prior to the analysis, the samples were outgassed at 200 °C until the pressure reached 10⁻² mPa. Surface areas were calculated from the N₂ adsorption isotherm in a relative pressure range of 0.02 to 0.2 by Brunauer-Emmett-Teller (BET) method.

The oxidation states of supported Fe catalysts were determined by XANES at Beamline 8 of the Synchrotron Light Research Institute (SLRI). The storage ring is operated with the electron energy of 1.2 GeV and electron current between 90 and 140 mA. Double Ge (2 2 0) crystals were used as synchrotron X-ray monochromators. The photon energy was scanned from 7100 to 7180 eV with a step of 0.2 eV. The energy calibration was performed using Fe standard foil at Fe K-edge (7112.0 eV). Compositions of Fe phases in all samples were calculated from the XANES spectra by the Linear Combination Fit (LCF) in Athena program. Standards of Fe in various oxide forms are FeO, Fe₃O₄ and Fe₂O₃.

DR-UV-Vis spectra were recorded on a Perkin Elmer, Lambda 750. Spectra were collected in range of 190-700 nm at a resolution of 3 nm. BaSO₄ was used as non-absorbing standard.

Profiles from ammonia temperature-programmed desorption (NH₃-TPD) were obtained from a conventional flow reactor connected to a mass spectrometer (MS, Balzers). The sample (0.1 g) was pretreated by heating under vacuum at 300 °C for 3 h. Then 10 kPa of NH₃ was allowed to adsorb on the sample at 100 °C for 1 h. Afterward the physically adsorbed NH₃ was removed under vacuum until the MS

signals were constant. The desorption was begun by increasing the temperature from 100 °C to 700 °C with a heating rate of 5 °C/min. The MS signal of desorbed NH₃ ($m/z = 17$), NH₂ ($m/z = 16$) and NH ($m/z = 15$) were measured with the temperature. The NH₃-TPD profiles were the plot between the NH₃ of signals and temperatures. Peak areas corresponded to acidity of supported Fe catalysts.

Temperature-programmed oxidation (TPO) profiles of spent catalysts were obtained using a flow reactor connected to the mass spectrometer. The spent catalyst (0.05 g) and quartz sand (0.05 g) were mixed, packed in a quartz tube and heated from 30 °C to 700 °C with the heating rate of 5 °C/min. Meanwhile, 3% O₂/Ar was flowed through the spent catalyst with a total flow rate 40 mL/min. Signals of produced CO₂ ($m/z = 44$), CO ($m/z = 28$) were recorded with the temperature. The TPO profiles were the plot of produced CO₂ signals against temperature. Peak areas corresponded to amount of produced coke on the spent supported Fe catalysts.

Moreover, the TPO of the spent catalysts were also performed and monitored by FTIR technique. The pellet of spent catalyst (10 mg) was heated from 25 °C to 450 °C with the rate of 5 °C/min under O₂ (100 mbar) atmosphere. The FTIR measurement was done on a BRUKER FT-IR spectrophotometer, VERTEX series with the time.

3.3.6 Catalytic testing on phenol hydroxylation

The testing was performed in a batch reactor with an apparatus setup similar to the previous work (Chumee et al., 2009). Firstly, 0.05 g of catalyst was mixed with 25 mL of 0.3332 M phenol aqueous solution in a 50 mL three necked round bottom flask connected to a thermometer and a reflux condenser. Then the mixture was heated to 70 °C in a mineral oil bath and held for 30 min under stirring at

700 rpm. To start the reaction, 0.86 mL of 30% H₂O₂ was added into the mixture with the phenol:H₂O₂ mole ratio of 1:1. The total volume of the reaction mixture was 25.86 mL. The 0.4 mL of mixture was withdrawn by a glass syringe at 10, 15, 30, 60, 90, 120 and 180 min of reaction times. The products were analysed by a gas chromatograph (SHIMADZU 14A series) equipped with an ID-BP1 coated capillary column and a flame ionization detector. The initial column temperature was held at 65 °C for 1.0 min before increased to 180 °C with 10 °C/min. The injection temperature and detector temperature were set at 200 °C. Toluene was used as an internal standard. The retention time and peak area in the chromatogram were used for qualitative and quantitative analysis. Calibration curves of phenol, CAT, HQ and BQ can be found in Appendix B. The phenol conversions are calculated from Eq. (3.1). Appearance of solution mixture and catalysts was compared as a preliminary indication of tar formation and coking. The carbon balances by mole during the reaction are calculated from Eq. (3.2). Then, the product selectivity is calculated based on their moles as shown in Eq. (3.3).

$$\text{Phenol conversion(\%)} = \left(\frac{\text{Initial mole of phenol} - \text{Final mole of phenol}}{\text{Initial mole of phenol}} \right) \times 100 \quad (3.1)$$

$$\% \text{ Carbon loss (mole)} = \left(\frac{\text{spent phenol (mole)} - \sum \text{CAT+ HQ + BQ (mole)}}{\text{spent phenol (mole)}} \right) \times 100 \quad (3.2)$$

$$\text{Product selectivity (\%)} = \left(\frac{\text{mole of target product}}{\text{mole of CAT, HQ, BQ and other products}} \right) \times 100 \quad (3.3)$$

3.4 Results and discussion

3.4.1 Characterization of zeolite BEA and supported Fe catalysts

The Fe content in all catalysts determined by ICP-OES is included in Table 1. The Fe loading on catalysts from IWI and PM were higher than that from LSIE. The loading on NH₄BEA was higher than that on HBEA indicating that the ion exchange is favorable on the ammonium form. In general, a better dispersion can be obtained by LSIE method (Ma et al., 2012).

Table 3.1 Fe contents and N₂ adsorption-desorption analysis results of synthesized zeolite BEA and supported Fe catalysts.

Properties	% Fe (wt/wt)	Si/Al	S _{BET} (m ² /g)	V _{micropore} (cm ³ /g)
HBEA ^a	-	9.31	617	0.24
NH ₄ BEA ^a	-	9.77	613	0.25
Fe/HBEA-IWI	6.21	10.58	598	0.23
Fe/HBEA-LSIE	1.45	12.63	602	0.23
Fe/NH ₄ BEA-LSIE	3.12	13.05	610	0.23
Fe/HBEA-PM	7.70	10.92	478	0.18

XRD patterns of the HBEA, NH₄BEA and Fe supported catalysts are shown Figure 3.1. The pattern of all samples consisted of characteristic peaks of BEA at 7.8° and 22.4° (Cambor et al., 1991; Loiha et al., 2009). The peaks from Fe/HBEA-IWI and Fe/HBEA-PM had lower intensity than those from Fe/HBEA-LSIE and Fe/NH₄BEA-LSIE. The higher amount of Fe from IWI and PM method may hinder the scattering of the incident X-ray. However, peaks corresponding to various forms of Fe were not observed due to either good dispersion or low loading. In another work by Li et al. (2008), XRD peaks of iron oxides were not observed from the samples containing 5-6 wt% Fe prepared by ion exchange on NaY.

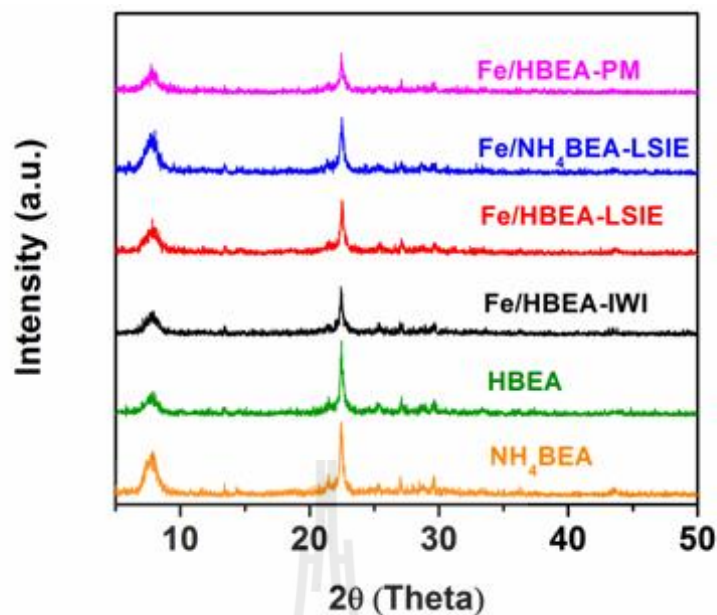


Figure 3.1 XRD patterns of NH_4BEA and HBEA, Fe/MCM-22-IWI, Fe/HMCM-22-LSIE, Fe/ $\text{NH}_4\text{MCM-22-LSIE}$ and Fe/HMCM-22-PM.

Nitrogen adsorption-desorption isotherms of zeolite BEA and the supported Fe catalysts are shown as Figure 3.2. The numeric data is compiled in Appendix C. All isotherms were type I according to IUPAC classification which is characteristic of microporous materials (Condon et al., 2006). Their surface area and volumes are summarized in Table 3.1 After loading with Fe, the surface area and pore volume were not significantly different from those of the bare zeolite indicating a good dispersion of Fe species. However, an exception was from Fe/HBEA-PM that the surface area and pore volume were significantly lower than that of HBEA. It was possible that particles of Fe species partially blocked the zeolite pores.

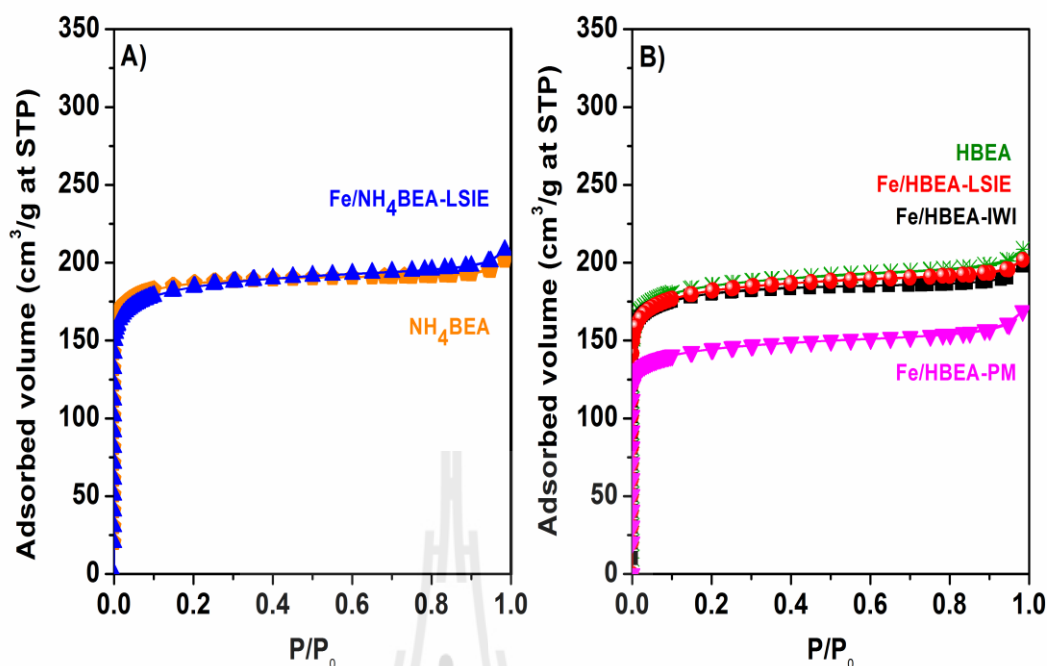


Figure 3.2 A) Nitrogen adsorption desorption isotherm of NH₄BEA and Fe/NH₄BEA-LSIE B) Nitrogen adsorption desorption isotherm of HBEA, Fe/HBEA-IWI, Fe/HBEA-LSIE and Fe/HBEA-PM.

Forms of Fe were determined by X-ray absorption spectroscopy. The X-ray absorption near edge structure (XANES) was a determinate region. XANES spectra of Fe standards with various oxidation states (Fe⁰, Fe²⁺, Fe^{2+/3+} and Fe³⁺) and supported catalysts at K-edge are shown in Figure 3.3. The spectra of all supported Fe catalysts were similar to that of Fe₂O₃ phase suggesting that Fe₂O₃ was the major phase. The only phase of Fe was also confirmed by Linear Combination Fitting (LCF) (Table 3.2). However, there was an exception from Fe/HBEA-PM which composed of trace amount of metallic Fe.

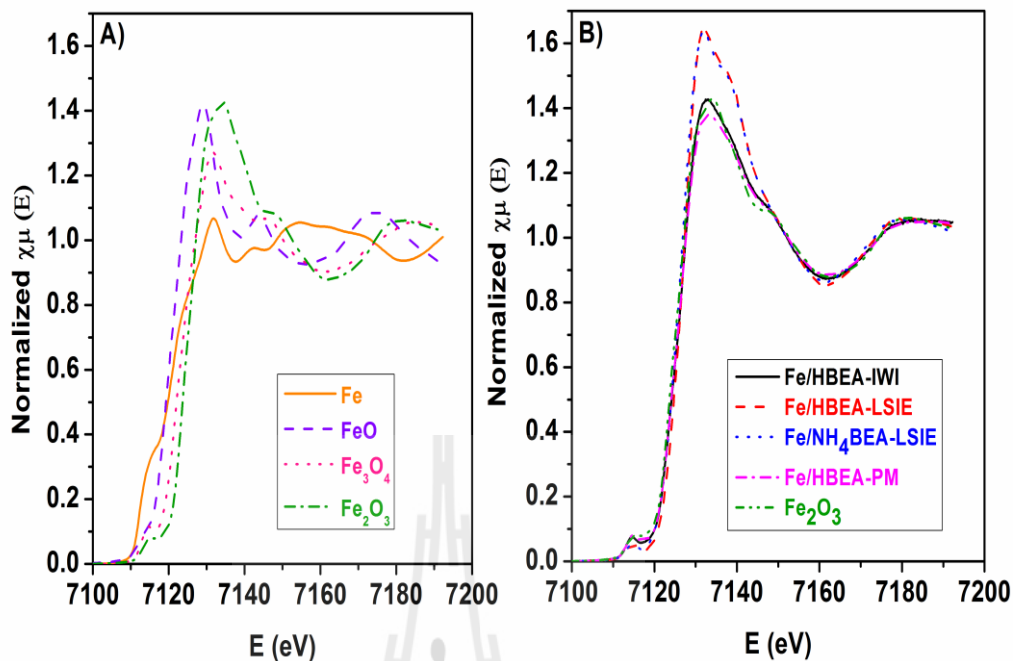


Figure 3.3 A) XANES spectra of Fe standards B) XANES spectra of Fe/HBEA, Fe/HBEA-LSIE, Fe/NH₄BEA-LSIE, Fe/HBEA-PM and Fe₂O₃.

Table 3.2 Linear combination fitting results of supported Fe catalysts.

Properties	Fe/HBEA-IWI	Fe/HBEA-LSIE	Fe/NH ₄ BEA-LSIE	Fe/HBEA-PM
Iron components				
Fe ₂ O ₃ (%)	100.0	100.0	100.0	98.9
Fe (%)	-	-	-	1.1
Reliability factor, R	0.0037	0.0385	0.0338	0.0040
Chi-square	0.25	3.31	2.77	0.27

DR-UV-Vis spectra of supported Fe catalysts with deconvolution are shown in Fig. 3.4. The absorption bands at 217 nm and 276 nm from Fe/HBEA-LSIE and Fe/NH₄BEA-LSIE were assigned to charge transfer from oxygen to monomeric Fe either at ion exchange site (Høj et al., 2009) or in the zeolite framework of zeolite beta (Boron' et al., 2015; Dzwigaj et al., 2007). Similar assignment was given to the first

two peaks of Fe/HBEA-IWI and Fe/HBEA-PM. Moreover, the peaks at 333, 448 nm from Fe/HBEA-IWI and at 320 and 438 nm from Fe/HBEA-PM were assigned to Fe with octahedral geometry which are oligomers on extraframework (Liang et al., 2013; Kumar et al., 2004; Schwidder et al., 2005; Hensen, 2005). In addition, the small peaks at 547 nm from Fe/HBEA-IWI and at 540 nm from Fe/HBEA-PM were assigned to Fe₂O₃ particles on the external surface of zeolite (Høj et al., 2009; Schwidder et al., 2005; Li et al., 2008; Li et al., 2011).

The results from DR-UV-Vis spectroscopy implied that Fe from LSIE was in the form of Fe₂O₃ which mainly located at the zeolite exchange position. Fe₂O₃ in the catalysts from IWI and PM were larger in particle sizes and located at both exchange position and on external surface. The larger particle size of Fe₂O₃ prepared by PM could attribute to more pore blocking and consequently, lower surface area, consistent with the results from N₂ adsorption-desorption.

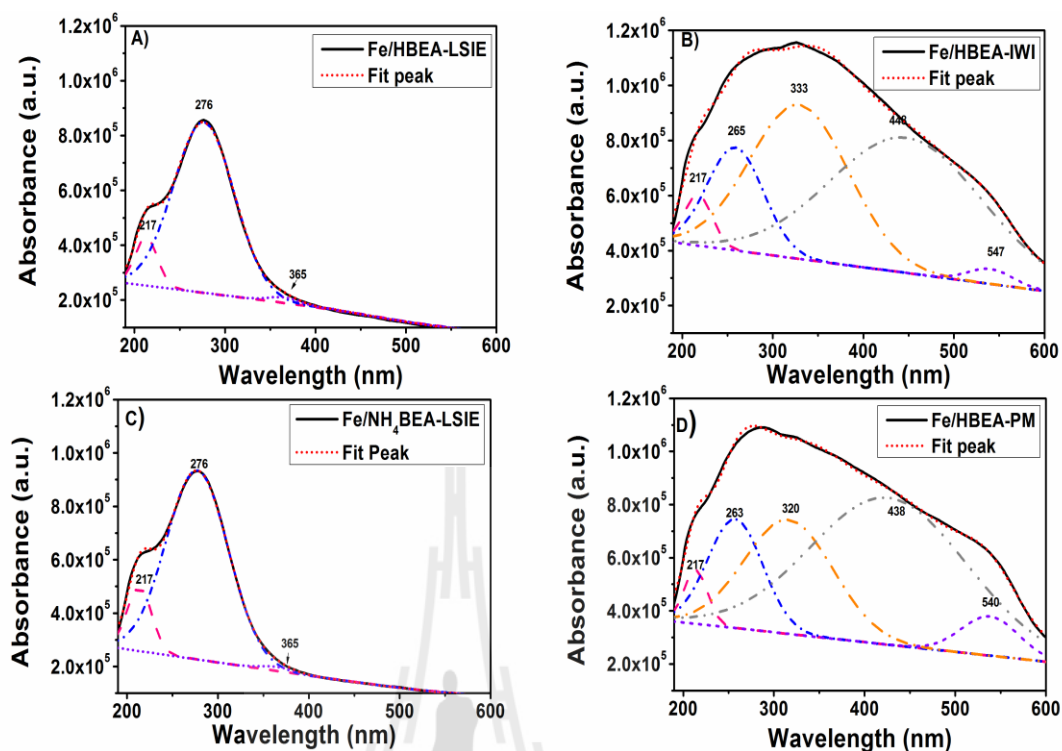


Figure 3.4 DR-UV-Vis spectra of A) Fe/HBEA-IWI B) Fe/HBEA-LSIE C) Fe/NH₄BEA-LSIE and D) Fe/HBEA-PM.

The NH₃-TPD profiles of all catalysts are shown in Figure 3.5. All samples exhibited two strong peaks at around 200 and 300 as well as a weak peak around 450 °C. The first peak was also observed in the NH₃-TPD profiles of HBEA with various Si/Al ratio (Loiha et al., 2009; Camiloti et al., 1999; Boron' et al., 2013; 2015). Thus, this signal could be assigned to the adsorption of NH₃ on silicon with unsaturated bonding and structural defect of zeolite (Boron' et al., 2013; 2015; Camiloti et al., 1999). In contrast, the second peak in bare zeolite was not strong. Thus, the second peaks from our samples were contributed from iron oxide. From the work of Boron' et al. (2015), the second peak from Fe/HBEA was higher than that of HBEA. Moreover, the third peak from IWI catalyst was weaker than that from LSIE and PM catalysts

indicating the lack of strong acid sites. This peak may contribute to Lewis acid sites generated from ion exchange. A similar observation, namely, a new peak at 470 °C from Ca/HBEA prepared by ion exchange was reported (Atoguchi and Kanougi, 2004).

Note that the release of NH_3 from Fe/ NH_4 BEA-LSIE in this work was from desorption of NH_3 from acid sites as well as decomposition of the remaining ammonium ion at the exchange position. Thus, it was not surprising that the signal of NH_3 released from Fe/ NH_4 BEA-LSIE was higher than that from Fe/HBEA-LSIE. Consequently, the TPD profile of Fe/ NH_4 BEA-LSIE was not discussed in detail.

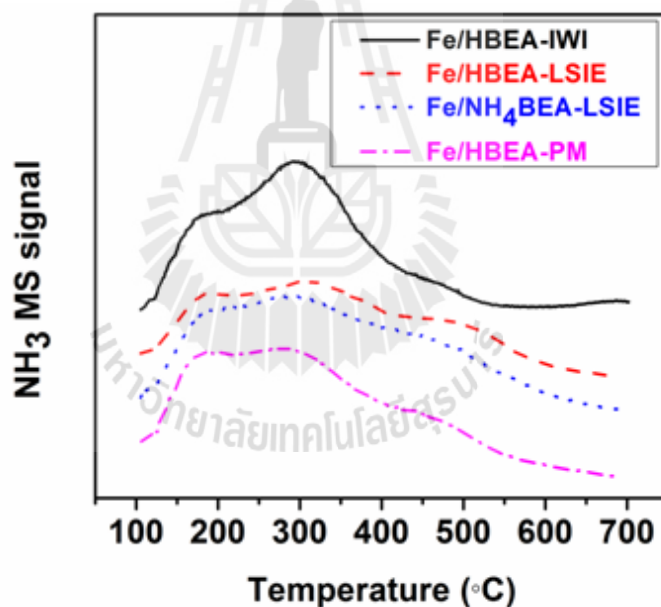


Figure 3.5 NH_3 -TPD profiles of supported Fe catalysts.

3.4.2 Catalytic performance of Supported Fe catalysts in phenol hydroxylation

Phenol conversions from hydroxylation are shown in Figure 3.6. All catalysts gave steady conversions of around 60% from the first point except

Fe/HBEA-IWI which took longer time to reach the steady values. Since Fe/HBEA-LSIE had the lowest Fe loading, it could be considered the most active catalyst. Thus, the active sites for this reaction are Fe_2O_3 at the zeolite exchange positions. However, HBEA was prepared by converting NaBEA to NH_4BEA by ion exchange with NH_4NO_3 followed by calcination which consumed more time and energy. Similar conversions between Fe/HBEA-LSIE and Fe/ NH_4BEA -LSIE suggested that NH_4BEA can be used directly to prepare the active catalyst.

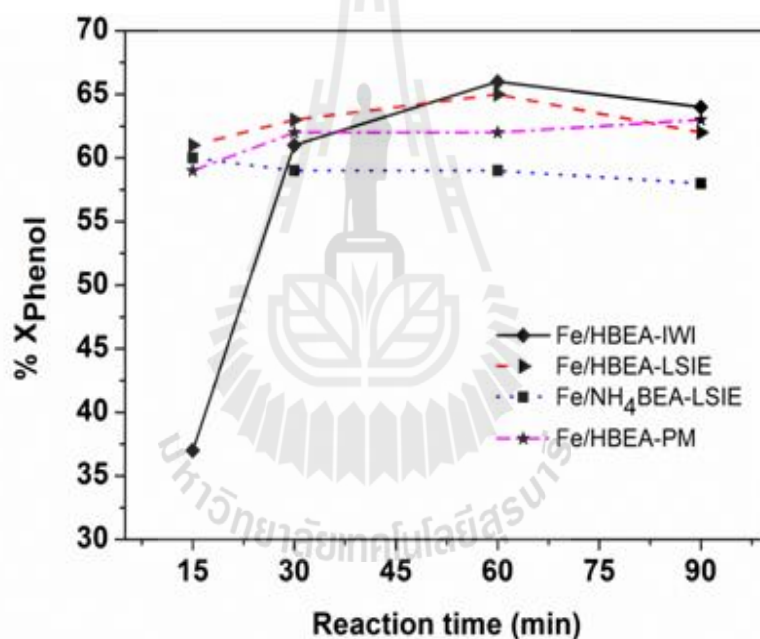


Figure 3.6 Phenol conversions during the phenol hydroxylation reaction at 70 °C with the reaction time of Fe/HBEA-IWI, Fe/HBEA-LSIE, Fe/ NH_4BEA -LSIE and Fe/HBEA-PM.

The product selectivity with the reaction time is concluded into Table 3.3. CAT was the major product from all catalysts followed by HQ. A small amount of BQ was detected at an early stage from Fe/HBEA-IWI. It was a kinetic product because

the concentration decreased with the time. Similar observation on the decrease of benzoquinone was reported for Fe on mordenite (Kulawong et al., 2011). Moreover, there were products not detected by GC but calculated on the basis of carbon balance by mole. The products were labeled “others”.

Table 3.3 Product selectivity and turnover number (TON) at various reaction times of supported Fe catalysts.

Catalyst	Reaction time (min)	%S _{products}				TON ^a
		CAT	HQ	BQ	Others	
Fe/HBEA-IWI	15	42	11	10	35	2.73
	30	42	21	0	35	4.50
	60	35	17	0	47	4.91
	90	37	17	0	46	4.78
Fe/HBEA-LSIE	15	44	22	0	34	16.56
	30	39	19	0	41	17.30
	60	36	18	0	44	17.76
	90	42	21	0	37	16.86
Fe/NH₄BEA-LSIE	15	42	21	0	37	8.20
	30	46	23	0	32	7.99
	60	46	23	0	32	8.05
	90	46	23	0	31	8.82
Fe/HBEA-PM	15	44	29	0	27	3.90
	30	41	22	0	36	3.91
	60	41	22	0	36	3.72
	90	37	25	0	37	3.96

TON^a was calculated from converted mole of phenol / mole of Fe catalyst.

Figure 3.7 shows the product yields at 90 min from all samples. Fe/NH₄BEA-LSIE gave the highest amount of CAT and HQ and the lowest amount of others. Therefore, the monomeric Fe resided in the zeolite pore was more active than other forms for the phenol hydroxylation. Base on the product yield, the straight pore

of BEA could not improve the HQ selectivity as expected. The yield of CAT and HQ were similar from all catalysts with CAT:HQ molar ratio around 2:1.

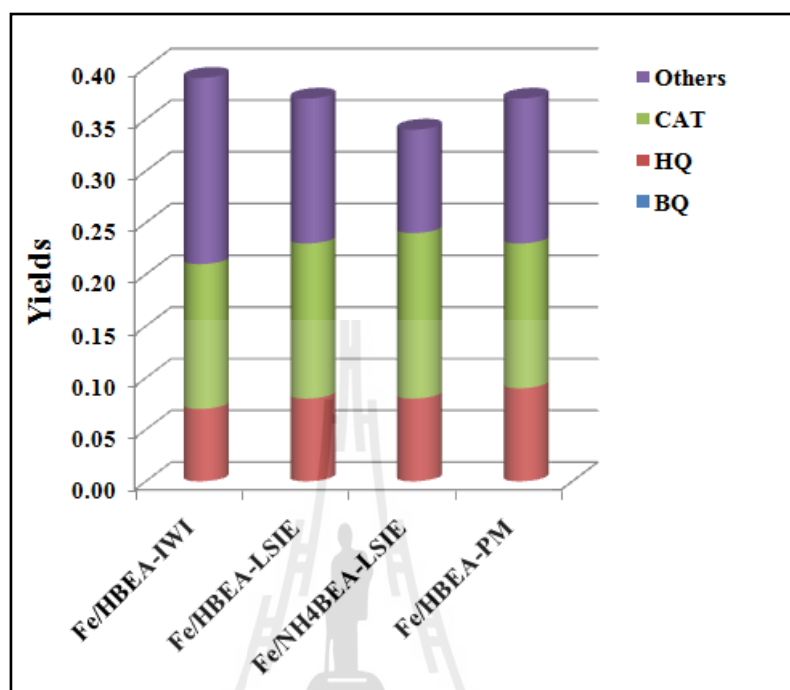


Figure 3.7 Product yields during the phenol hydroxylation at 90 min of Fe/HBEA-IWI, Fe/HBEA-LSIE, Fe/NH₄BEA-LSIE and Fe/HBEA-PM.

After the catalytic testing, the color of all catalysts was brown (See Figure 3.8) indicating that coke was produced. The more darkness could obtain on Fe/HBEA-IWI and Fe/HBEA-PM catalysts which contained high Fe content. Several researchers demonstrated that CAT, HQ and BQ could be oxidized further under the excess amount of H₂O₂ to produce tar (Liang et al., 2013; Karakhanov et al., 2010).

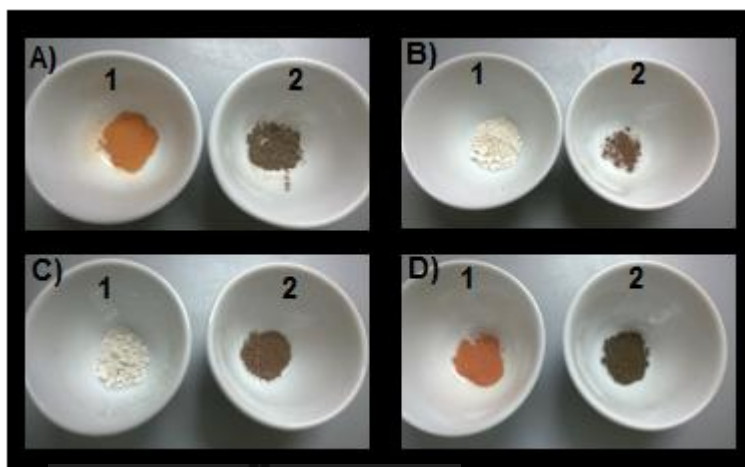


Figure 3.8 Images of fresh (1) and spent (2) catalyst for A) Fe/HBEA-IWI, B) Fe/HBEA-LSIE C) Fe/NH₄BEA-LSIE and D) Fe/HBEA-PM.

Temperature-programmed oxidation profiles of the spent catalysts are shown in Figure 3.9. The CO₂ signal arose from combustion of the coke deposited on the spent catalysts. The temperature reflects the length of carbon chain. The peaks represented between 250 and 450 °C were from light coke on the catalyst external surface. The peaks between 450 and 650 °C were from heavy coke generated within the zeolite cavity (Guisnet et al., 2009; Ibáñez et al., 2014). In addition, the peak area was proportional to the amount of coke.

Fe/HBEA-PM and Fe/HBEA-IWI exhibited a large signal in the region of light coke which may be generated from either weak or moderate acid sites on the external surface. The peak from Fe/HBEA-PM occurred at lower temperature than Fe/HBEA-IWI but had a larger area indicating that Fe/HBEA-PM produced a lighter coke but with a larger amount. In case of Fe/NH₄BEA-LSIE and Fe/HBEA-LSIE, they produced two types of coke which are heavier than that from the IWI and PM catalysts. The heavy coke from LSIE catalysts may be generated from the strong acid

sites. The Fe/NH₄BEA-LSIE produce higher amount of light coke but smaller amount heavy coke than Fe/HBEA-LSIE. The less amount of heavy coke from Fe/NH₄BEA-LSIE suggesting that it can be regenerated more easily, making it a more suitable catalyst for phenol hydroxylation.

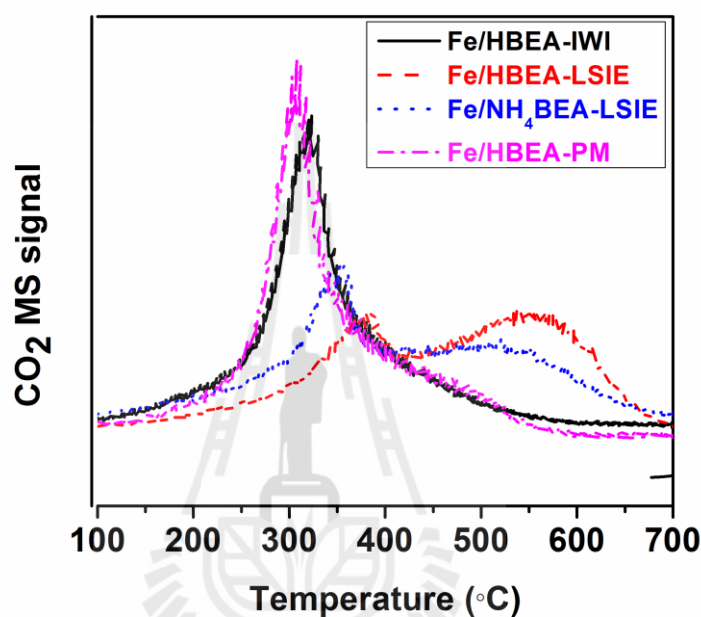


Figure 3.9 CO₂ temperature programmed oxidation of spent catalyst of Fe/HBEA-IWI, Fe/HBEA-LSIE, Fe/NH₄BEA-LSIE and Fe/HBEA-PM catalysts.

In addition, coke on the spent catalysts was also studied by TPO-FTIR as shown in figure 3.10. The peak assignments are concluded into Table 3.4. The characteristic bands of zeolite were observed at 1997, 1866 and 1263 cm⁻¹. The adsorbed H₂O on the zeolite was observed at 1634 cm⁻¹ and disappeared after the oxidation for all samples. For the spent catalysts before oxidation, they showed the peaks at 1720, 1629 and 1508 cm⁻¹ which all assigned to carbonaceous species or coke from the polymerization of reaction intermediates during the phenol hydroxylation. After the oxidation at 450 °C, those peaks assigned to coke were

decreased. In case of spent Fe/HBEA-LSIE, the peaks related to coke were still observed even after oxidation at high temperature indicating that the cokes were strongly interacted to zeolite support in proton form.

Table 3.4 Characteristic of infrareds assignments.

Phase	Bands (cm^{-1})	Assignments	Type of vibrations	Reference
HBEA and HMCM-22	1996, 1877	zeolite	Overtone lattice	Rintramee et al., 2012
	1263-1288	zeolite	Si-O-Si	Rintramee et al., 2012
	1634	adsorbed H_2O	δ O-H	Pechar and Rykl., 1979
Hydrocarbon deposited on zeolite	1721	carbonyl species	$\nu(\text{C}=\text{O})$	Smith et al., 1979
	1598	carbonaceous species	$\nu\text{C}=\text{C}$ cyclic	Abbas et al., 2008
	1508, 1501	formate	$\nu(\text{COO}-)$	Merayo et al., 2013
	1482, 1474, 1467	carbonaceous species	$\nu\text{C}=\text{C}$ cyclic	Garcia-C. et al., 2003

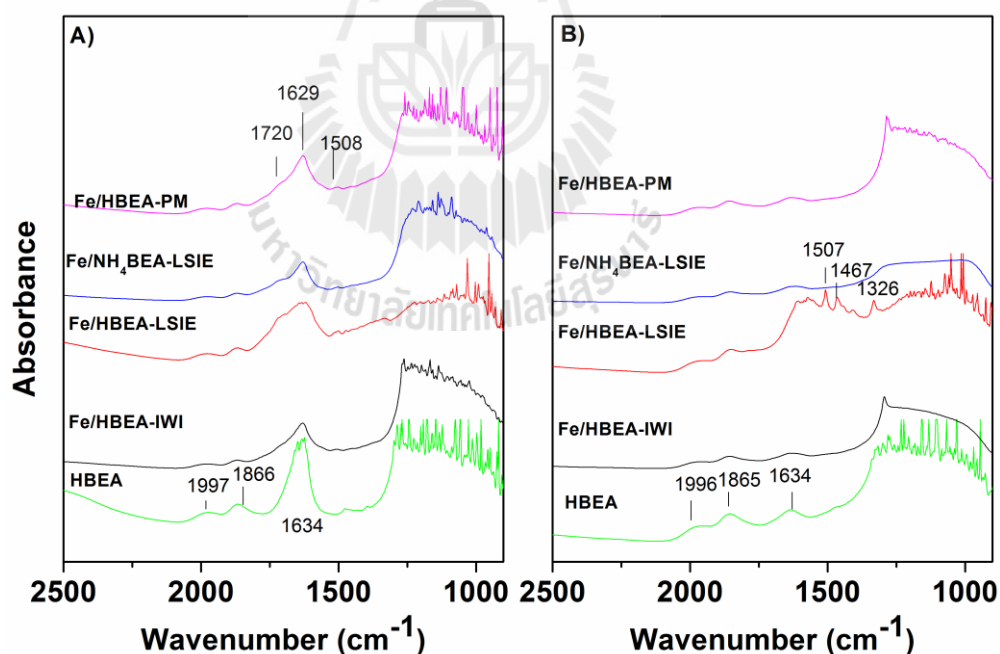


Figure 3.10 FTIR spectra of spent catalyst in a series of zeolite BEA A) before the oxidation at 25 °C and B) after the oxidation at 450 °C.

3.5 Conclusions

The Fe catalysts were loaded onto zeolite BEA by incipient wetness impregnation (IWI), liquid state ion-exchange (LSIE) and physical mixing (PM). The Fe loading by IWI and PM methods were 6-7 wt%. The resulting iron oxide mainly located as iron oligomers at zeolite extraframework and Fe_2O_3 particles on the zeolite surface. For LSIE method, the Fe loading was around 1-3 wt% by the isolated iron was mostly observed at the ion-exchange site of zeolite. For all catalysts, Fe_2O_3 was suggested as a main phase and well dispersed on supports except Fe/HBEA-PM catalyst.

The catalyst activities toward the phenol hydroxylation were tested. All catalysts showed a steady conversion of 60% from the first point of measurement except Fe/HBEA-IWI. HQ and CAT were the main products with CAT/HQ ratio of 2/1. In addition, BQ was detected as minor products. The Fe/HBEA-LSIE was the most active catalyst according to the highest TON.

The spent catalysts were further studied by TPO. Fe/HBEA-IWI and Fe/HBEA-PM showed the light cokes with large amount released from the external surface of the catalyst. In otherwise Fe/HBEA-LSIE and Fe/ NH_4 BEA-LSIE showed the heavy coke with less amounts released from the external surface and inside the pores of zeolite. With the lighter coke produced on Fe/ NH_4 BEA-LSIE accompanied by the less energy consuming for both catalyst preparation and regeneration over Fe/HBEA-LSIE, Fe/ NH_4 BEA-LSIE was the best catalyst chosen for the phenol hydroxylation.

3.6 References

- Abbas, O., Rebufa, C., Dupuy, N. and Kister, J. (2008). FTIR—Multivariate curve resolution monitoring of photo-Fenton degradation of phenolic aqueous solutions Comparison with HPLC as a reference method. **Talanta**. 77: 200.
- Ahmad, P. and Rasool, S. (2014). Emerging technologies of crop stress tolerance. **Biological techniques**. first ed. pp. 423
- Atoguchi, T. and Kanougi, T. (2004). Phenol oxidation over alkaline earth metal ion exchange beta zeolite in the presence of ketone. **Journal of Molecular Catalysis A: Chemical**. 222: 253-257.
- Atoguchi, T., Kanougi, T., Yamamoto, T. and Yao, S. (2004). Phenol oxidation into catechol and hydroquinone over H-MFI, H-MOR, H-USY and H-BEA in the presence of ketone. **Journal of Molecular Catalysis A: Chemical**. 220: 183-187.
- Balle, P., Geiger, B. and Kureti, S. (2009). Selective catalytic reduction of NO_x by NH₃ on Fe/HBEA zeolite catalysts in oxygen-rich exhaust. **Applied Catalysis B: Environmental**. 85: 109-119.
- Barrer, R. M. (1979). Zeolites and clay minerals as sorbents and molecular sieves. **Academic Press**, London.
- Boroń, P., Chmielarz, L., Gurgul, J., Łątka, K., Shishido, T., Krafft, J-M. and Dzwigaj, A. (2013). BEA zeolite modified with iron as effective catalyst for N₂O decomposition and selective reduction of NO with ammonia. **Applied Catalysis B: Environment**. 138-139: 434-445.
- Boroń, P., Chmielarz, L., Gurgul, J., Łątka, K., Gil, B., Marszałek, B. and Dzwigaj, A. (2015) Influence of iron state and acidity of zeolites on the catalytic activity of

FeHBEA, FeHZSM-5 and FeHMOR in SCR of NO with NH₃ and NO₂.

Microporous and Mesoporous Materials. 203: 73-85.

Bortnovsky, O., Sobalík, Z. and Wichterlová, B. (2001). Exchange of Co(II) ions in H-BEA zeolites: identification of aluminum pairs in the zeolite framework.

Microporous and Mesoporous Materials. 46: 265-275.

Camblor, M. A. and Pérez-Pariente, J. (1991). Crystallization of zeolite beta: Effect of Na and K ions. **Zeolites.** 11: 202-210.

Camiloti, A. M., Jahn, S. L., Velasco, N. D., Moura, L. F. and Cardoso, D. (1999). Acidity of Beta zeolite determined by TPD of ammonia and ethylbenzene disproportionation. **Applied Catalysis A: General.** 182: 107-113.

Capek, L., Kreibich, V., Decek, J. De, Grygar, T., Wichterlova, B., Sobalí, Z., Martens, J. A., Brosius, R. and Tokarova, V. (2005). Analysis of Fe species in zeolites by UV–VIS–NIR, IR spectra and voltammetry: Effect of preparation, Fe loading and zeolite type. **Microporous and Mesoporous Materials.** 80: 279-289.

Clerici, M. G. and Kholdeeva, O. A. (2013). Liquid Phase Oxidation via Heterogeneous Catalysis. **Organic Synthesis and Industrial Applications.** pp.546.

Chume, J., Gridanurak, N., Neramittagapong, S. and Wittayakun, J. (2009). Characterization of AlMCM-41 synthesized with rice husk silica and utilization as supports for platinum iron catalysts. **Brazilian Journal of Chemical Engineering.** 26: 367-373.

Condon, J. B. (2006). Surface Area and Porosity Determination by Physisorption: Measurement and Theory, Elsevier, Oxford, United Kingdom.

- Dzwigaj, S., Stievano, L., Wagner, F-E. and Che, M. (2007). Effect of preparation and metal content on the introduction of Fe in BEA zeolite, studied by DR UV-vis, EPR and Mossbauer spectroscopy. **Journal of Physics and Chemistry of Solids**. 68: 1885-1890.
- Garcia-Cortes, J. M., Perez-Ramirez, J., Rouzaud, J. N., Vaccaro, A. R., Illan-Gomez, M. J. and Salinas-Martinez De Lecea, C. (2003). On the structure sensitivity of deNO_x HC-SCR over Pt-beta catalysts. **Journal of Catalysis**. 218: 111-122.
- Gerei, S. V., Rozhkova, E. V. and Gorokhovatskii, Y. B. (1973). Propylene and oxygen chemisorption on cupric oxide and cuprous oxide catalysts. **Journal of catalysis**. 28: 341-350.
- Guisnet, M., Costa, L. and Ramôa R. F. (2009). Prevention of zeolite deactivation by coking. **Journal of Molecular Catalysis A: Chemical**. 305: 69-83.
- He, C., Wang, Y., Cheng, Y., Lambert, C. K. and Ralph, T. (2009). Activity, stability and hydrocarbon deactivation of Fe/Beta catalyst for SCR of NO with ammonia. **Applied Catalysis A: General**. 368: 121-126.
- Hensen, E., Zhu, Q., Janssen, R., Magusin, P., Kooyman, P. and Vansanten, R. (2005). Selective oxidation of benzene to phenol with nitrous oxide over MFI zeolites: 1. On the role of iron and aluminum. **Journal of Catalysis**. 233: 123-135.
- Høj, M., Beier, M. J., Grunwaldt, J-D. and Dahl, S. (2009). The role of monomeric iron during the selective catalytic reduction of NO over Fe-BEA zeolite catalysts. **Applied Catalysis B: Environmental**. 93: 166-176.
- Ibáñez, M., Artetxe, M., Lopez, G., Elordi, G., Bilbao, J., Olazar, M. and Castano, P. (2014). Identification of the coke deposited on an HZSM-5 zeolite catalyst

- during the sequenced pyrolysis–cracking of HDPE. **Applied Catalysis B: Environmental**. 436: 148-149.
- Jia, C., Beaunier, P. and Massiani, P. (1998). Comparison of conventional and solid-state ion exchange procedures for the incorporation of lanthanum in H-beta zeolite. **Microporous and Mesoporous Materials**. 24: 69-82.
- Kulawong, S., Prayoonpokarach, S., Neramittagapong, A. and Wittayakun, J. (2011). Mordenite modification and utilization as supports for iron catalyst in phenol hydroxylation. **Journal of Industrial and Engineering Chemistry**. 17: 346-351.
- Kumar, M. S., Schwidder, M., Brückner, A. and Grünert, W. (2004). On the nature of different iron sites and their catalytic role in Fe-ZSM-5 DeNO_x catalysts: new insights by a combined EPR and UV/VIS spectroscopic approach. **Journal of Catalysis**. 227: 384-397.
- Li, L., Shen, Q., Li, J., Hao, Z., Xu, Z-P. and Max Lu, G. Q. (2008). Iron-exchanged FAU zeolites: Preparation, characterization and catalytic properties for N₂O decomposition. **Applied Catalysis A: General**. 344: 131-141.
- Li, S., Li, G., Li, G., Wua, G. and Hua, C. (2011). Microporous carbon molecular sieve as a novel catalyst for the hydroxylation of phenol. **Microporous and Mesoporous Materials**. 143: 22-29.
- Liang, X., Yang, R., Li, G. and Hu, C. (2013). Phenol hydroxylation over Fe-incorporated mesoporous materials prepared by coprecipitation. **Microporous and Mesoporous Materials**. 182: 62-72.
- Lin, T.-A., Schwartz, L. H. and Butt, J. B. (1986). Iron alloy Fischer-Tropsch catalysts: V. FeCo on Y zeolite. **Journal of Catalysis**. 97: 177-187.

- Loiha, S., Prayoonpokarach, S., Songsiriritthigun, P. and Wittayakun, J. (2009). Synthesis of zeolite beta with pretreated rice husk silica and its transformation to ZSM-12. **Materials Chemistry and Physics**. 115: 637-640.
- Ma, L., Chang, H., Yang, S., Chen, L., Fu, L. and Li, J. (2012). Relations between iron sites and performance of Fe/HBEA catalysts prepared by two different methods for NH₃-SCR. **Chemical Engineering Journal**. 209: 652-660.
- Pechar, F. and Rykl, D. (1981). Infrared spectra of natural zeolites of the stilbite group. **Chemické Zvesti**. 35: 189-202.
- Rintramee, K., Föttinger, K., Rupprechter, G. and Wittayakun, J. (2012). Ethanol adsorption and oxidation on bimetallic catalysts containing platinum and base metal oxide supported on MCM-41. **Applied Catalysis B: Environmental**. 115-116: 225-235.
- Schwidder, M., Kumar, M. S., Klementiev, K., Pohl, M. M., Brückner, A. and Grünert, W. (2005). Selective reduction of NO with Fe-ZSM-5 catalysts of low Fe content I. Relations between active site structure and catalytic performance. **Journal of Catalysis**. 231: 314-330.
- Smith, A. L. (1979). Applied infrared spectroscopy: fundamentals, techniques, and analytical problem solving. **Wiley - Interscience**. pp. 336.
- Varagnat, J. (1976). Hydroquinone and pyrocatechol production by direct oxidation of phenol. **Industrial and Engineering Chemistry Product Research and Development**. 15: 212-215.
- Wang, J., Park, J. N., Wei, X. Y. and Lee, C. W. (2003) Room-temperature heterogeneous hydroxylation of phenol with hydrogen peroxide over Fe²⁺, Co²⁺ ion-exchanged Na β zeolite. **Chemical Communications**. 9: 628-629.

Wittayakun, J., Khemthong, P. and Prayoonpokrach S. (2008). Synthesis and characterization of zeolite Y from rice husk silica. **Korean Journal of Chemical Engineering**. 25: 861-864.



CHAPTER IV

INFLUENCE OF DEALUMINATION OF ZEOLITE BEA ON THE CATALYTIC PERFORMANCE IN PHENOL HYDROXYLATION

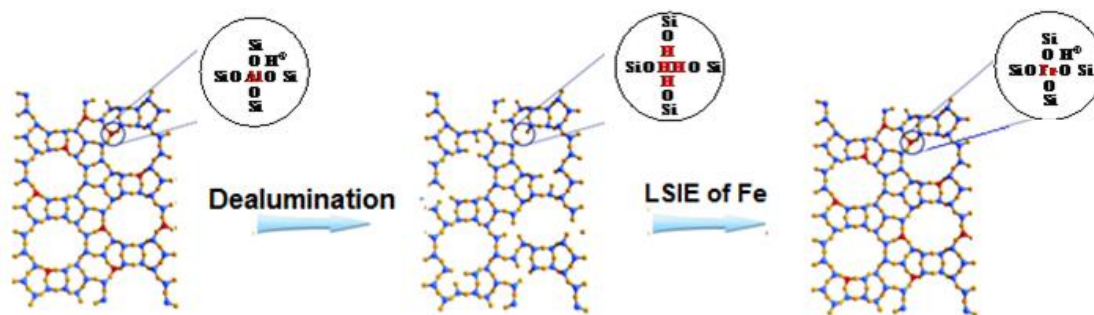
4.1 Abstract

This chapter focuses on the influence of dealumination of zeolite BEA for the phenol hydroxylation. The commercial HBEA (Si/Al = 25) was used as a precursor. It was dealuminated by HNO₃ aqueous solution for 30, 120, 180 and 240 min. The obtained dealuminated HBEA (D-BEA) was used as a support for Fe catalyst which was loaded by liquid state ion exchange method (LSIE). The dealuminated BEA and Fe supported catalyst were characterized by XRD, DR-UV-Vis, and NH₃-TPD and XANES technique. The Al was removed during the acid treatment and Fe was inserted into the T-vacant site as active species for phenol hydroxylation. The reaction testing was performed in a batch reactor at 70 °C with phenol: H₂O₂ molar ratio of 1:1. The reaction rate was monitored at 3 min. They were in the following order: Fe/D-BEA-30 > Fe/D-BEA-240 > Fe/D-BEA-120 > Fe/D-BEA-180. The steady state was reached in 45 min from all catalysts.

4.2 Introduction

Zeolite BEA is a three dimensional intersecting channel system; polymorphs A and B which are straight channels and a sinusoidal channel (Wadlinger et al., 1967). The BEA in proton form (HBEA) is pronounced as acid catalyst for many kinds of industrial reaction (Atoguchi et al., 2004; Dai et al., 1996). The presence of Al in zeolite framework results in Brønsted acid site as $-\text{Si}-(\text{OH})-\text{Al}-$. From the work of Atoguchi and Kanougi (2004), the formation of coke during the phenol hydroxylation depends on the amount of the Brønsted acid site (Atoguchi and Kanougi, 2004).

According to results from chapter III, coke was founded selectively for 40% over Fe supported catalyst on BEA in phenol hydroxylation. The presence of Al might affect the formation of tar. To clarify the hypothesis, the influence of Al in zeolite BEA continued to be studied in this chapter. Al content was varied by degree of dealumination through the acid treatment. HNO_3 was employed to dissolve Al with different period of times as shown in Scheme 4.1. Then the Fe was inserted to the T-vacant site by liquid state ion-exchange method. Series of Fe/D-BEA was used as catalysts for the phenol hydroxylation.



Scheme 4.1 Dealumination of zeolite BEA and insertion of Fe by LSIE, adapted from Tang et al. (2014).

4.3 Experiment

4.3.1 Chemicals

HBEA 25 (Si/Al = 12.5) was from Süd-Chemie AG. The chemicals for dealumination of zeolite BEA was concentrate HNO_3 (fuming, 99.5 % v/v HNO_3 , SIGMA - ALDRICH). The chemical for the preparation of supported Fe catalysts was ferric nitrate nonahydrate ($\text{Fe}(\text{NO}_3)_3 \cdot 9\text{H}_2\text{O}$, QR&C). The chemicals for the reaction testing for phenol hydroxylation and for the preparation of internal standard curves were similar to the details in topic 3.3.1 of chapter III.

4.3.2 Dealumination of zeolite BEA

HBEA was dealuminated according to an established procedure (Baran et al., 2012). The HBEA (Si/Al = 12.5) was treated with 6.5 M HNO_3 aqueous solution at 80 °C under the stirring (1400 rpm) for different times: 30, 120, 180 and 240 min. The ratio of solution/solid was 10 mL/g. After the acid treatment, the solid was separated by centrifugation, washed with DI water and dried overnight at 100 °C. The obtained solid was named D-BEA-30, D-BEA-120, D-BEA-180 and D-BEA-240, respectively. They were used as supports for Fe catalyst.

4.3.3 Preparation of Supported Fe catalysts

Fe catalysts were loaded onto the dealuminated supports by liquid state ion-exchange (LSIE). The LSIE was carried out with a method from the literature (Dzwigaj et al., 2007). A 1.8×10^{-2} M $\text{Fe}(\text{NO}_3)_3$ aqueous solution was ion-exchanged with D-BEA-30, D-BEA-120, D-BEA-180 or D-BEA-240 at room temperature for 24 h under stirring. The solution/solid ratio was 50 mL/g. The solid was separated by centrifugation, washed with DI water, dried and calcined at 450 °C for 3 h. The obtained catalysts were denoted as Fe/D-BEA-30, Fe/D-BEA-120, Fe/D-BEA-180 and Fe/D-BEA-240, respectively.

4.3.4 Catalyst characterization

The dealuminated BEA and the supported Fe catalysts were characterized by various techniques. The structure of zeolite BEA was confirmed by XRD. The oxidation states of the supported Fe catalysts were determined by XANES. The environment of Fe on dealuminated BEA was investigated by DR-UV-Vis. All details of the measurements were similar to those in topic 3.3.5 of chapter III. Moreover, the acidity of sample was measured by ammonia temperature-programmed desorption (NH_3 -TPD) using the chemisorption analyzer, BELCAT. The analysis steps were as follows; sample 50 mg was pretreated at 300 °C for 1 h under the flow of He with a rate of 50 mL/min. Then 35% NH_3/He was allowed to adsorb on a sample at 30 °C for 1h. Afterward, the physically adsorbed NH_3 was removed by flushing with He flowing of 50 mL/min at 150 °C for 1 h, and then the sample was cooled down to 30 °C. The NH_3 desorption was started by heating the samples from 30 to 700 °C. Signal of desorbed NH_3 is proportional to the acidity of sample was recorded by a TCD detector.

4.3.5 Catalytic testing on phenol hydroxylation

Catalytic testing in phenol hydroxylation was performed in a batch reactor by using the apparatus setup similar to those in the literature (Chumee et al., 2009). Details of the conditions and analysis procedures were described in topic 3.3.6 of Chapter III.

4.4 Results and Discussion

4.4.1 Characterization of dealuminated BEA and supported Fe catalysts

Figure 4.1 shows a series of XRD patterns for D-BEA and Fe/D-BEA. They reveal characteristic peaks of BEA structure at 7.8° and 22.4° (Camblore et al., 1991; Loiha et al., 2009). The acid treatment did not destroy the zeolite structure. However, the diffraction peak at 22.5° shifted to a higher degree upon the acid treatment. This was general taken as an evidence for lattice contraction/expansion of the BEA structure (Camblor et al., 1993). The d_{302} spacing was calculated from Bragg's law ($d = n\lambda/2\sin\theta$) and concluded in Table 4.1. The decrease of d_{302} spacing indicated the removal of Al from zeolite framework. After Fe loading, the d_{302} spacing increased suggesting that Fe was inserted into the zeolite framework (Dzwigaj and Che, 2006; Gurgul et al., 2013).

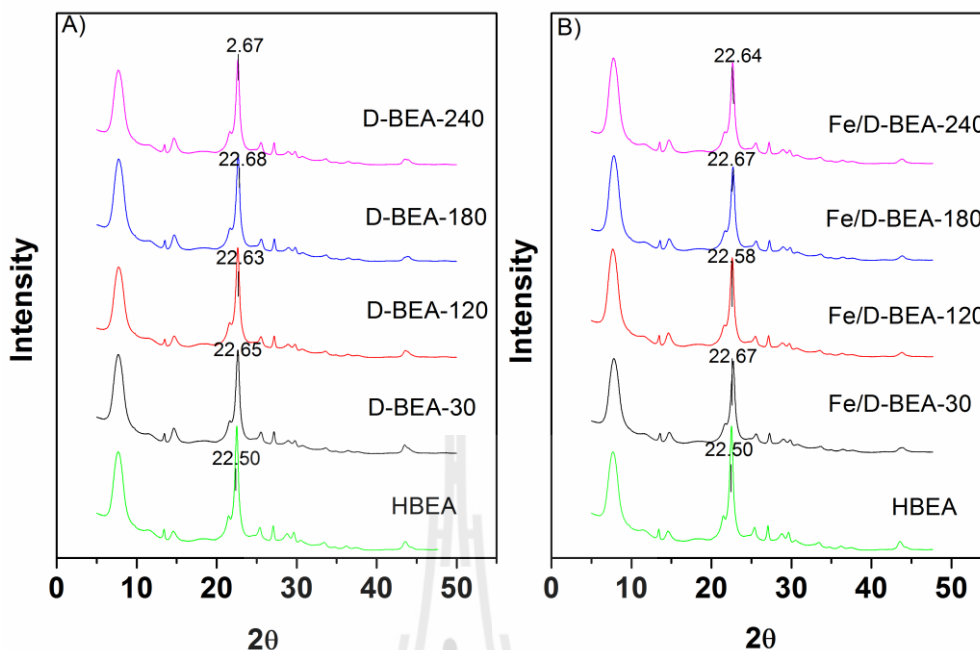


Figure 4.1 XRD patterns of A) D-BEA and B) Fe/D-BEA catalysts.

Table 4.1 Details of d_{302} spacing.

D-BEA	d_{302} spacing, Å	Fe/D-BEA	d_{302} spacing, Å
HBEA	3.9484	HBEA	3.9484
D-BEA-30	3.9226	Fe/D-BEA-30	3.9192
D-BEA-120	3.9260	Fe/D-BEA-120	3.9346
D-BEA-180	3.9175	Fe/D-BEA-180	3.9192
D-BEA-240	3.9192	Fe/D-BEA-240	3.9243

Figure 4.2 shows a series of DR-UV-Vis spectra for Fe/D-BEA catalysts. The main absorption bands at 216 and 265 nm were assigned to oxygen charge transfer to Fe (III) within tetrahedral coordination (Gurgul et al., 2013; Capek et al., 2005; Maier et al., 2011). Thus, Fe located at the T-vacant site in the zeolite framework consistent with the results from XRD. Moreover, a small band at around 445 nm was assigned to oxygen charge transfer to Fe (III) within octahedral coordination (Kumar et al., 2006) whereas the tetrahedral Fe inside the zeolite

framework could migrate to extraframework during the calcination (Gurgul et al., 2013).

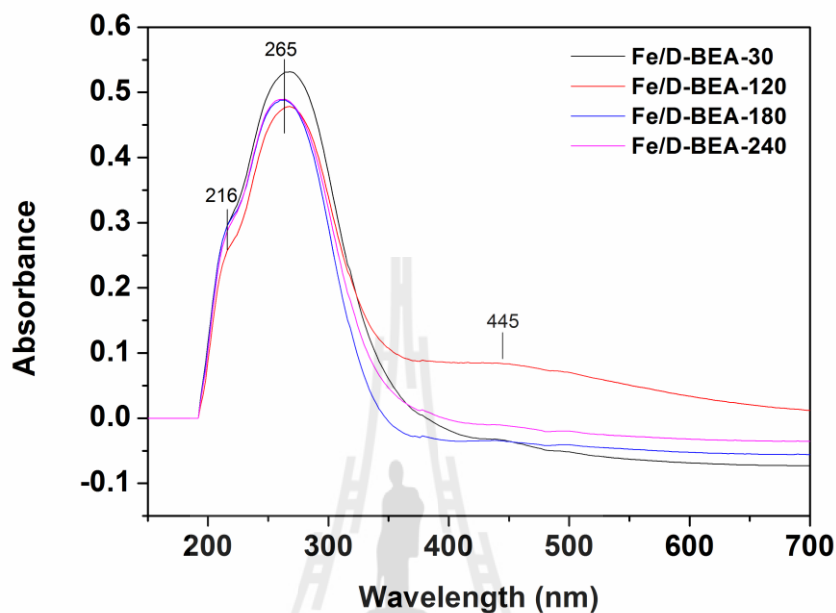


Figure 4.2 DR-UV-Vis spectra of Fe/D-BEA catalysts.

The XANES spectra of supported Fe catalysts are shown in Figure 4.3. All Fe/D-BEA catalysts exhibited similar spectra indicating that they had Fe in the same form. The pre-edge was observed for all samples indicated the Fe within the tetrahedral coordination.

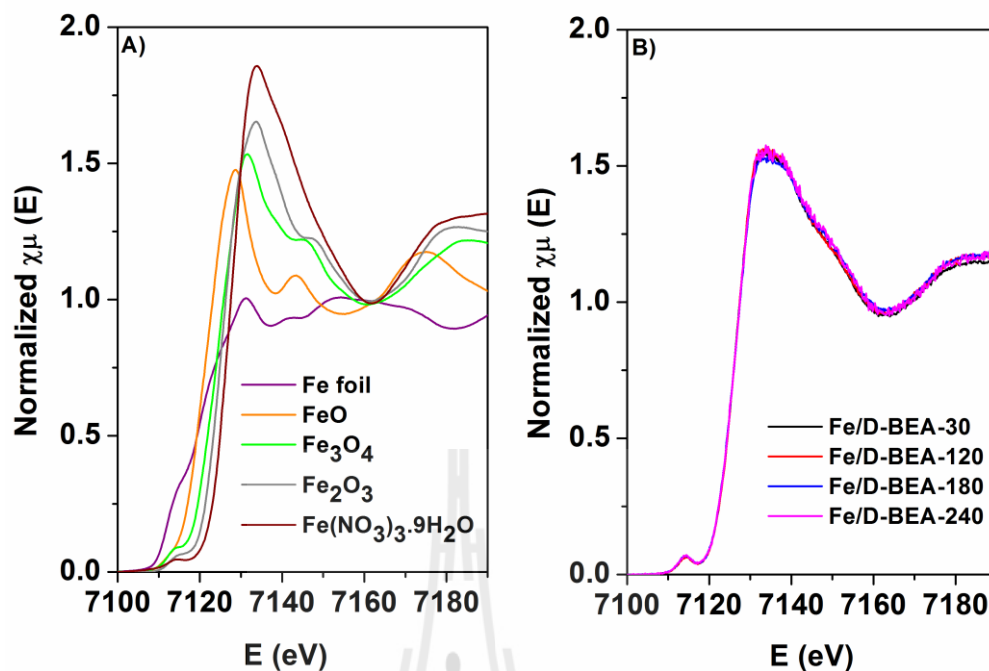


Figure 4.3 XANES spectra for A) Fe standards with different oxidation states B) Fe/D-BEA.

The composition of Fe phases was determined from Linear Combination Fitting (LCF) by comparing with spectrum of standards. The results are shown in Table 4.2. Fe(NO₃)₃ precursor was suggested to be a major phase. However, this results is debatable because Fe(NO₃)₃ can be decomposed completely by calcination in air at 400 °C to yield Fe₂O₃ (Ciurowa and Kozak, 1999). In this work, the calcination of Fe/D-BEA was carried out at 450 °C for 3 h in a hot air oven which should be enough to decompose the Fe(NO₃)₃. Besides, the presence of Fe(NO₃)₃ phase was not observed by XRD. Aritani and co-workers, (2002) studied the Fe substituted Al mordenite by XANES. The samples with various degree of Fe substituted were fitted well with NaFeO₃ and Fe(OH)₃ standards. The pre-edge was predominately observed proving the Fe in the zeolite framework (Aritani et al., 2002).

Table 4.2 Linear combination fitting results Fe/D-BEA.

Properties	Fe/D-BEA-30	Fe/D-BEA-120	Fe/D-BEA-180	Fe/D-BEA-240
Iron components				
Fe foil (%)	20	18	21	19
FeO (%)	0	0	0	0
Fe ₃ O ₄ (%)	0	2	0	3
Fe ₂ O ₃ (%)	19	16	16	12
Fe(NO ₃) ₃ .9H ₂ O	61	64	63	67
Reliability factor, R	0.0054	0.0050	0.0067	0.0059

The acidity was examined by NH₃-TPD technique. Figure 4.4 gives the TPD profiles of D-BEA and Fe/D-BEA. For parent HBEA, There were 3 desorption peaks observed at 164 and 462 and 600 °C related to weak, medium and strong acid site. After acid treatment, the peak at 164 °C obviously decreased because the removal of extraframework Al inside zeolite BEA (Srivastava et al., 2009). For high temperature desorption peaks at 462 and 600 °C, they drastically increased exhibiting the desorbed NH₃ from the T-vacant site of zeolite. When the framework Al was removed the hydroxyl was generated to maintain the charge balance and NH₃ could adsorb on these hydroxyls (Wang et al., 2001; Atoguchi and Kanougi, 2004; Marques et al., 2005). The more desorbed NH₃ at high temperature region reflects the more T-vacant sites generated in zeolite through the dealumination. In case of Fe/D-BEA, the acidity was drastically reduced especially for the high desorption temperature peak. The loaded Fe could locate inside the T-vacant site and obstruct the adsorption of NH₃.

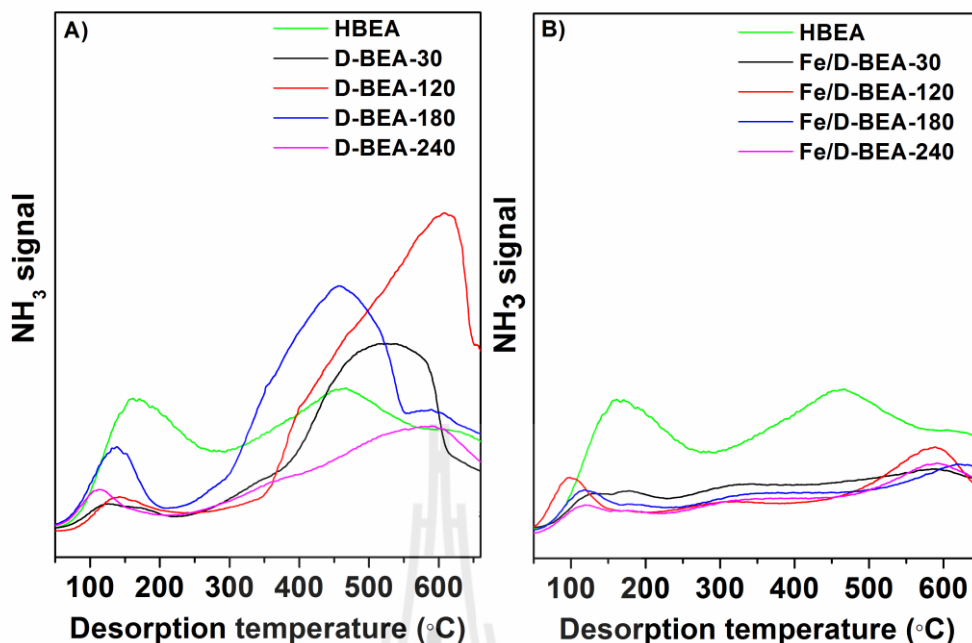


Figure 4.4 NH_3 -TPD profiles of A) D-BEA and B) Fe/D-BEA catalysts.

4.4.2 Catalytic performance in phenol hydroxylation

The initial rate could be observed from the conversions at 3 min as shown in Figure 4.5A). They were in the following order: Fe/D-BEA-30 > Fe/D-BEA-240 > Fe/D-BEA-120 > Fe/D-BEA-180. According to the work from Xiong and co-workers (2000), phenoxy radical is generated by a hydrogen abstraction on the acid center of solid catalyst. The generated phenoxy radical is reactive toward the phenol hydroxylation and immediately yielded CAT and HQ. In this work, the Al could be removed with the dealumination time. Consequently the initial reaction rate was lowered. Then, the conversion became increase for Fe/D-BEA-240 suggesting that the zeolite pore opening could occur and increase the reactant diffusion (Kullawong et al., 2014). As shown in Figure 4.5B, all catalysts reached the maximum conversion of 60% within 6 min except Fe/D-BEA-120 which took 30 min. According to the

reaction rate, Fe/D-BEA-30 is of interest to be used as a catalyst for the fixed bed flow reactor.

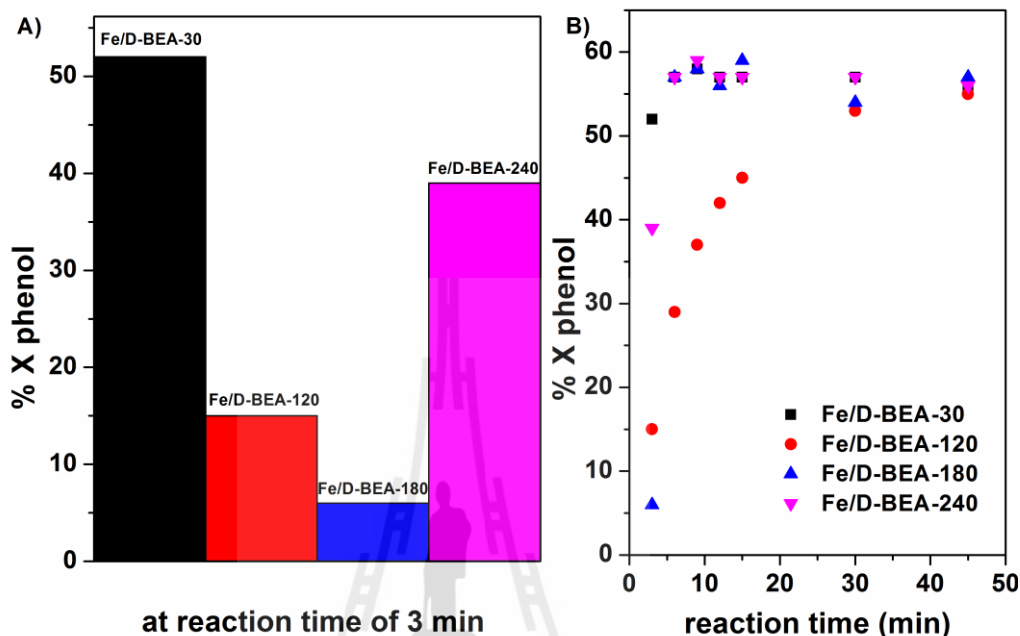


Figure 4.5 Phenol conversions for Fe/D-BEA catalysts at A) 3 min and B) various times.

The product selectivity is summarized into Table 4.2. CAT and HQ were observed as major products while BQ was observed as a kinetic product at the beginning of the reaction. For Fe/D-BEA-120, the BQ was increased with the conversion and no longer observed when the reaction reached the steady state. Mass loss during the reaction was suggested by the carbon balance. Cause of the mass loss could be coke deposition on catalyst because the catalyst had dark color after the reaction.

Table 4.3 Product selectivity during the phenol hydroxylation.

catalyst	Reaction time, min	%X phenol	%S CAT	%S HQ	%S BQ	%S Others
Fe/D-BEA-30	3	52	48	22	4	27
	6	57	49	27	0	24
	9	58	47	25	0	28
	12	57	49	27	0	24
	15	57	49	27	0	24
	30	57	50	28	0	22
	45	56	51	28	0	21
Fe/D-BEA-120	3	15	50	14	4	33
	6	29	44	11	16	29
	9	37	50	14	15	21
	12	42	50	17	10	23
	15	45	51	20	8	22
	30	53	52	25	1	23
	45	55	51	25	0	25
Fe/D-BEA-180	3	6	64	28	8	0
	6	57	48	21	1	30
	9	58	47	22	0	31
	12	56	51	27	0	22
	15	59	45	23	0	32
	30	54	53	28	0	19
	45	57	51	27	0	23
Fe/D-BEA-240	3	39	45	17	9	29
	6	57	49	25	0	25
	9	59	47	24	0	29
	12	57	49	26	0	25
	15	57	48	26	0	26
	30	57	50	27	0	23
	45	56	52	28	0	20

Figure 4.6 shows the product yields at 45 min for all catalysts. There was not significantly difference. The other products still observed with high contents. The obtained HQ/CAT was around 0.5. From the results, the dealumination degree did not affect the product yields but it played an important role only in the induction period for the phenol hydroxylation.

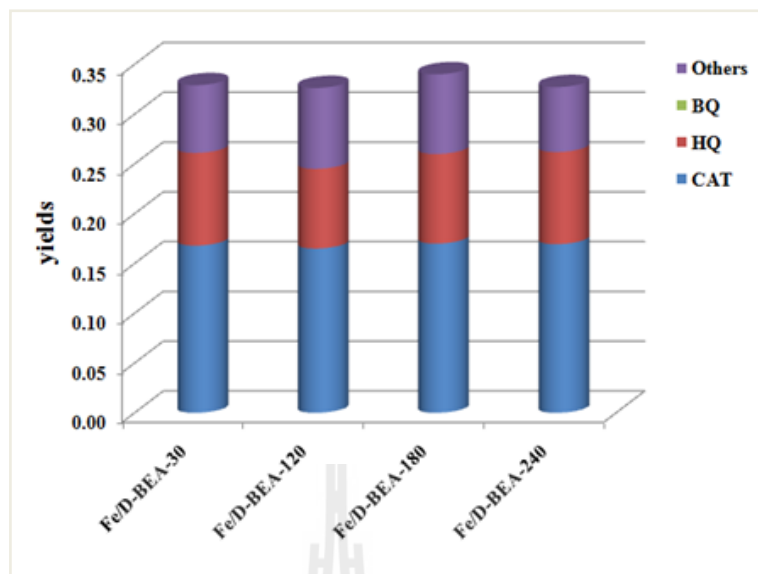


Figure 4.6 Product yields during the phenol hydroxylation at 45 min of Fe/D-BEA-30, Fe/D-BEA-120, Fe/D-BEA-180 and Fe/D-BEA-240.

To demonstrate the effect of dealumination, the catalytic activity of Fe/D-BEA-30 was compared with the Fe/HBEA-LSIE from chapter III. They were remarkably recognized that BEA from chapter III was a lab-made material whereas the BEA in this chapter was a commercial material. Figure 4.7 shows the product yields for Fe/HBEA-LSIE and Fe/D-BEA-30 in phenol hydroxylation. The Fe/D-BEA-30 gave higher CAT and HQ yields than Fe/HBEA-LSIE. For “others”, it relates to mass loss which was undetectable product by GC-FID during the testing. Fe/D-BEA-30 gave a lower mass loss than Fe/HBEA-LSIE. Therefore, dealumination could reduce the formation of tar as expected and in a good agreement with the results from Atoguchi and Kanougi (2004).

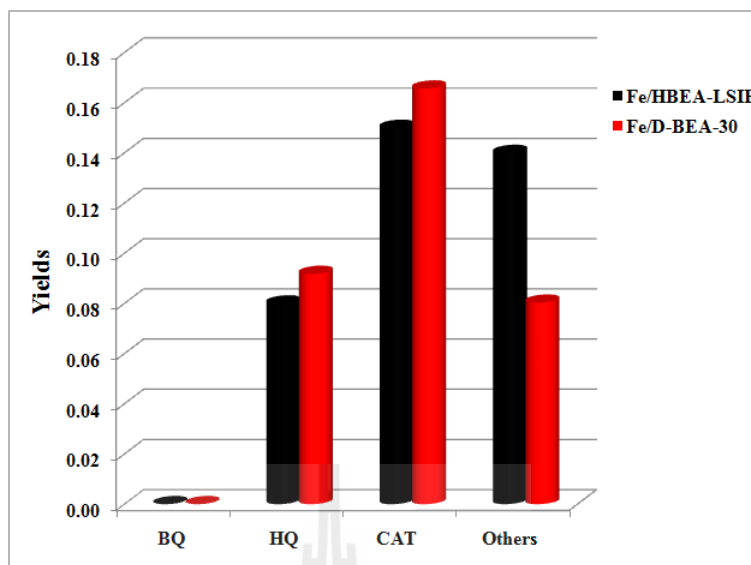


Figure 4.7 Product yields during the phenol hydroxylation over Fe/HBEA-LSIE (from chapter III) and Fe-D-BEA-30 (this chapter).

4.5 Conclusions

Dealumination of zeolite BEA for various times by HNO_3 was carried out. The BEA structure was contracted proving by the decrease of d_{302} spacing. The Fe was introduced into the T-vacant sites of modified BEA which were generated upon the dealumination. From DR-UV-Vis results, the Fe mostly appeared as Fe (III) with tetrahedral coordination resided in T-vacant site of BEA. A series of Fe/D-BEA was tested for phenol hydroxylation. Fe-D/BEA-30 was the most active catalyst reaching the maximum conversion of 52% within 3 min. It also provided the highest product yield; CAT and BQ. Finally, the dealumination of BEA support could reduce the formation of tar.

4.6 References

- Aritani, H., Nishimura, S., Tamai, M., Yamamoto, T., Tanaka, T. and Nakahira, A. (2002). Local structure of framework iron in Fe-substituted Al-mordenites by Fe K edge XAFS. **Chemistry of Materials**. 14: 562-567.
- Atoguchi, T. and Kanougi, T. (2004). Phenol oxidation over alkaline earth metal ion exchange beta zeolite in the presence of ketone. **Journal of Molecular Catalysis A: Chemical**. 222: 253-277.
- Atoguchi, T., Kanougi, T., Yamamoto, A. T. and Yao, S. (2004). Phenol oxidation into catechol and hydroquinone over H-MFI, H-MOR, H-USY and H-BEA in the presence of ketone. **Journal of Molecular Catalysis A: Chemical**. 220: 183-187.
- Baran, R., Millot, Y., Onfroy, T., Krafft, J-M. and Dzwigaj, S. (2012). Influence of the nitric acid treatment on Al removal, framework composition and acidity of BEA zeolite investigated by XRD, FTIR and NMR. **Microporous and Mesoporous Materials**. 163: 122-130.
- Camblor, M. A. and Pariente, J. P. (1991). Crystallization of zeolite beta: Effect of Na and K ions. **Zeolites**. 11: 202-210.
- Camblor, M., Corma, A. and Pariente, J. P. (1993). Synthesis of titanoaluminosilicates isomorphous to zeolite Beta, active as oxidation catalysts. **Zeolites**. 13: 82-87.
- Capek, L., Kreibich, V., decek, J. D., Grygar, T., Wichterlova, B., Sobal, Z., Martens, J. A., Brosius, R. and Tokarova, V. (2005). Analysis of Fe species in zeolites by UV-VIS-NIR, IR spectra and voltammetry. **Microporous and Mesoporous Materials**. 80: 279-289.

- Chumee, J., Grisdanurak, N., Neramittagapong, S. and Wittayakun, J. (2009). Characterization of AlMCM-41 synthesized with rice husk silica and utilization as supports for platinumiron catalysts. **Brazilian Journal of Chemical Engineering**. 26: 367-373.
- Dai, L. -X, Hayasaka, R., Iwaki, Y., Koyano, K. A. and Tatsumi, T. (1996). Vapour phase Beckmann rearrangement of cyclohexanone oxime catalysed by H β zeolite. **Chemical Communications**. 9: 1071-1072.
- Dzwigaj, s. and Che, M. (2006). Incorporation of Co(II) in Dealuminated BEA zeolite at lattice tetrahedral sites evidenced by XRD, FTIR, diffuse Reflectance UV-Vis, EPR, and TPR. **The Journal of Physical Chemistry B**. 110: 12490-12493
- Dzwigaj, S., Stievano, L., Wagner, F.-E. and Che, M. (2007). Effect of preparation and metal content on the introduction of Fe in BEA zeolite, studied by DR UV-vis, EPR and Mossbauer spectroscopy. **Journal of Physics and Chemistry of Solids**. 68: 1885-1890.
- Gurgul, J., Ła, K., Hnat, I., Rynkowski, J. and Dzwigaj, S. (2013). Identification of iron species in FeSiBEA by DR UV-vis, XPS and Mössbauer spectroscopy: Influence of Fe content. **Microporous and Mesoporous Materials**. 168: 1-6.
- Kullawong, S., Prayoonpokarach, S., Neramittagapong, A. and Wittayakun, J. (2011). Mordenite modification and utilization as supports for iron catalyst in phenol hydroxylation. **Journal of Industrial and Engineering Chemistry**. 17: 346-351.
- Kumar, M. S., Schwidder, M., Grünert, W. and Brückner, A. (2004) On the nature of different iron sites and their catalytic role in Fe-ZSM-5 DeNO_x catalysts: new

- insights by a combined EPR and UV/VIS spectroscopic approach. **Journal of Catalysis**. 227: 384-397.
- Loiha, S., Prayoonpokarach, S., Songsiriritthigun, P. and Wittayakun, J. (2009). Synthesis of zeolite beta with pretreated rice husk silica and its transformation to ZSM-12. **Materials Chemistry and Physics**. 115: 637-640.
- Maier, S. M., Jentys, A. and Lercher, J. A. (2011). Steaming of Zeolite BEA and its Effect on Acidity: A Comparative NMR and IR Spectroscopic Study. **The Journal of Physical Chemistry C**. 115: 8005-8013.
- Marques, J. P., Gener, I., Ayrault, P., Bordado, J. C., Lopes, J. M., Ribeiro, F. R. and Guisnet, M. (2005). Dealumination of HBEA zeolite by steaming and acid leaching: distribution of the various aluminic species and identification of the hydroxyl groups. **Crystalline and organized porous solids**. 8: 399-410.
- Srivastava, R., Iwasa, N., Fujita, S-I. and Arai, M. (2009). Dealumination of zeolite Beta catalyst under controlled conditions for enhancing its activity in acylation and esterification. **Catalysis Letters**. 130: 655-663.
- Tang, B., Dai, W., Sun, X., Guan, N., Li, L. and Hunger, M. (2014). A procedure for the preparation of Ti-Beta zeolites for catalytic epoxidation with hydrogen peroxide. **Green Chemistry**. 16: 2281-2291.
- Xiong, C., Chen, Q., Lu, W., Gao, H., Lu, W. and Gao, Z. (2000). Novel Fe-based complex oxide catalysts for hydroxylation of phenol. **Catalysis Letters**. 69: 231-236.
- Wadlinger, R. L., Kerr, G. T. and Rosinski, E. J. (1967). US Patent 3 308 069 **reissued US Patent Re.** 28 341 (1975).

Wang, H. and Xin, W. (2001). Surface acidity of H-beta and its catalytic activity for alkylation of benzene with propylene. **Catalysis Letters**. 76: 225-229.

Wieczorek-Ciurowa, K. and Kozak, A. J. (1999). The Thermal Decomposition of $\text{Fe}(\text{NO}_3)_3 \cdot 9\text{H}_2\text{O}$. **Journal of Thermal Analysis and Calorimetry**. 58: 645-65.



CHAPTER V

INFLUENCE OF IRON LOADING METHOD ON ZEOLITE MCM-22 ON PHYSICOCHEMICAL PROPERTY AND CATALYTIC PERFORMANCE IN PHENOL HYDROXYLATION

5.1 Abstract

In this chapter, iron (Fe) was loaded on HMCM-22 by incipient wetness impregnation (IWI), liquid state ion-exchange (LSIE) and physical mixing (PM). The LSIE was also done with NH₄MCM-22. The zeolite structure in all samples was confirmed. Their surface areas were slightly lower than the bare zeolite. The form of iron was Fe₂O₃. The locating of Fe₂O₃ from IWI and PM were mainly on the external surface of MCM-22 whereas that from LSIE was inside the cavities. From the catalytic testing for phenol hydroxylation in a batch reactor, the catalysts from LSIE were the most active showing the maximum conversions within 15 min giving phenol conversion of 54%, CAT selectivity of 46%, HQ selectivity of 28%. Moreover, other products of 26% were estimated from carbon mass balance suggesting catalyst deactivation by a formation of tar. The tar on the spent catalysts was analyzed by temperature program oxidation.

5.2 Introduction

Zeolite MCM-22 is one of interesting supports for various active metals. MCM-22 is classified in MWW family according to the International Zeolite Association (IZA) structure commission. It was first synthesized in 1990 by Mobil through a hydrothermal method (Rubin and Chu, 1990). The synthesis can be carried out from either static or stirring condition (Wu et al., 2008; Corma et al., 1995). Moreover, it can be synthesized in a wide range of Si/Al ratio (Delitala et al., 2009). The presence of Al in the MCM-22 framework generates the exchangeable position for Fe cation.

MCM-22 has a unique and narrow pore structure. It consists of two independent pore systems including twodimensional10-membered ring sinusoidal channels and other large supercages of $7.1 \text{ \AA} \times 7.1 \text{ \AA} \times 18.2 \text{ \AA}$. Both pore systems extend in the same direction but there was no intersection of these two pore systems (Leonowicz et al., 1994). MCM-22 zeolites are very thin plates with large external surface area (Lawton et al., 1998). The prominent properties of MCM-22 are high thermal stability, high acid tolerance and molecular shape selectivity (Cheng et al., 1999). With the narrow pore structure of MCM-22, it is expected to be compatible to the reactant shapes and improve the selectivity of HQ in the phenol hydroxylation.

In this chapter zeolite MCM-22 was selected as a support for Fe. Particular attention was on the influence of Fe loading method on the catalytic performance for phenol hydroxylation. Fe was loaded on MCM-22 through the three different methods; IWI, LSIE and PM.

5.3 Experiment

5.3.1 Chemicals

Chemicals for synthesis of zeolite MCM-22 in sodium form were sodium aluminate (55 – 56 wt% NaAlO_2 , Riedel-de Haën), sodium hydroxide (98 wt% NaOH , Prolabo), hexamethyleneimine; HMI (99% $\text{C}_6\text{H}_{13}\text{N}$, Sigma-Aldrich) and fumed silica (99.8 wt% SiO_2 , Sigma-Aldrich). Chemical for ion-exchange sodium form zeolites to ammonium form zeolites was ammonium nitrate (99 wt% NH_4NO_3 , Fluka). Chemical for the preparation of supported Fe catalysts was ferric nitrate nonahydrate (99.9 wt% $\text{Fe}(\text{NO}_3)_3 \cdot 9\text{H}_2\text{O}$, QRĕC). Chemicals for the reaction testing for phenol hydroxylation and for the preparation of internal standard curves are similar to the details in a topic 3.3.1 of Chapter III.

5.3.2 Preparation of zeolite MCM-22 supports

NaMCM-22 zeolite was synthesized by a hydrothermal method according to an established procedure (Corma et al., 1995). The 0.92 g of NaAlO_2 was dissolved in 124.20 mL of 0.10 M NaOH aqueous solution. Then, the 7.61 g of hexamethyleneimine (HMI) was added to the solution and stirred for a day. Finally, the 9.23 g of SiO_2 was slowly dissolved into the solution and stirred for 3 days. The gel solution was hydrothermally treated at 150 °C in 250 mL of Teflon-lined stainless steel autoclave under stirring (100 rpm) for 7 days. The obtained solid was separated from the colloidal and washed with DI water until the wash solution was neutral. Then it was dried and calcined at 580 °C for 3 h to remove the HMI templates.

To convert to proton form, NaMCM-22 was refluxed with NH_4NO_3 aqueous solution at 80 °C for 8 h for three times to convert to $\text{NH}_4\text{MCM-22}$. The

obtained solid (NH₄MCM-22.) was filtered, washed with DI water and dried at 110 °C overnight. One portion of NH₄MCM-22 was calcined at 400 °C for 3 h to convert to HMCM-22. Both of NH₄MCM-22 and HMCM-22 were used as supports for Fe catalyst.

5.3.3 Preparation of supported Fe catalysts

Fe/MCM-22 catalysts were prepared by incipient wetness impregnation (IWI), liquid state ion exchange (LSIE) and physical mixing (PM) by methods from literatures (Balle et al., 2009; Dzwigaj et al., 2007; Capek et al., 2005) using Fe(NO₃)₃·9H₂O as a precursor. In IWI method, Fe(NO₃)₃ aqueous solution was impregnated to HMCM-22 with the wetness volume of 0.3 mL/g. The mixture was air-dried at room temperature, at 110 °C for 6 h and calcined at 450 °C for 3 h. The obtained catalyst was named Fe/HMCM-22-IWI.

In LSIE method, 1.8 x 10⁻² M Fe(NO₃)₃ aqueous solution was ion-exchanged with HMCM-22 or NH₄MCM-22 at room temperature for 24 h under stirring. The solid was separated by centrifugation, washed with DI water and dried overnight at 100 °C. The obtained solid was named Fe/HBEA-LSIE and Fe/NH₄BEA-LSIE, respectively. The Fe/HBEA-LSIE was further calcined at 450 °C for 3 h.

In PM method, Fe(NO₃)₃·9H₂O and HMCM-22 were ground with a mortar and pestle for 20 min. The obtained solid was calcined at 550 °C for 6 h under an air flow rate of 50 mL/min, cooled down, washed with DI water and dried at 110 °C overnight. The obtained catalyst was named Fe/HMCM-22-PM.

5.3.4 Characterization of zeolite MCM-22 and supported Fe catalysts

The synthesized zeolite MCM-22 and the supported Fe catalysts were characterized by several techniques. The structure of zeolite MCM-22 was confirmed by XRD. The surface area and pore volume were measured by N₂ adsorption-desorption analysis. The scanning electron microscope images of zeolite MCM-22 and supported Fe catalysts were taken by a field emission scanning electron microscopy & EDS, JEOL (JSM-7800F) at the magnification of 2000 times. The elemental analysis was done by ICP-OES. The oxidation states of the supported Fe catalysts were determined by XANES. The environment of Fe on zeolite MCM-22 was investigated by DR-UV-Vis. NH₃-TPD of catalyst was analyzed in a flow reactor connected with mass spectrometer (Balzers). TPO profiles of spent catalysts were also performed in a flow reactor connected with mass spectrometer. TPO-FTIR spectra of spent catalysts were also carried out in a chamber with an O₂ atmosphere upon the heating. All details of the measurements were similar to those in a topic of 3.3.5 of Chapter III.

5.3.5 Catalytic testing in phenol hydroxylation

Catalytic testing in phenol hydroxylation was performed in a batch reactor by using the apparatus setup similar to those in the literature (Chumee et al., 2009). Details of the conditions and analysis procedure were described as a topic of 3.3.6 in Chapter III.

5.4 Results and discussion

5.4.1 Characterization of zeolite MCM-22 and supported Fe catalysts

The Fe contents in all catalysts determined by ICP-OES are included in Table 5.1. The Fe loading on the samples prepared by IWI and PM were similar to the calculated values. Thus, all Fe were on the supports and possibly locate mainly on the external surface. The amount of Fe from LSIE was around 1 wt%. The Fe content indicated that the $\text{NH}_4\text{MCM-22}$ had a higher degree of metal ion exchange than that of HMCM-22 . By LSIE, the Fe cations had a good dispersion and located at the exchange position in the zeolite cavities. Ammonium cation has lower charge density than proton and, thus, a weaker interaction with the zeolite framework.

Table 5.1 Fe contents and N_2 adsorption-desorption analysis results of synthesized MCM-22 zeolite and supported Fe catalysts.

Properties	% Fe (wt/wt)	Si/Al	a_{SBET} (m^2/g)	Total pore volume (cm^3/g)
$\text{HMCM-22}^{\text{a}}$	-	16.43	330	0.4147
$\text{NH}_4\text{MCM-22}^{\text{a}}$	-	16.49	318	0.4024
Fe/HMCM-22-IWI	6.05	16.08	302	0.3758
Fe/HMCM-22-LSIE	0.85	16.74	324	0.4084
$\text{Fe/NH}_4\text{MCM-22-LSIE}$	0.92	16.33	304	0.3850
Fe/HMCM-22-PM	6.50	16.69	297	0.3836

Figure 5.1 shows XRD patterns of zeolite MCM-22 in ammonium and proton forms together with those of all Fe supported catalyst. The characteristic peaks of MCM-22 were observed (Corma et al., 1995). Thus, zeolite MCM-22 was successfully synthesized and the Fe loading did not destroy the zeolite structure. For Fe/HMCM-22-LSIE , $\text{Fe/NH}_4\text{MCM-22-LSIE}$ and Fe/HMCM-22-IWI , they displayed well defined diffraction patterns. The XRD pattern of Fe/HMCM-22-PM had peaks

with lower intensity. With higher Fe loading (6.50 %wt) the secondary scattering by Fe_2O_3 may be responsible for the lower intensity. However, the presence of Fe species was not observed from XRD probably due to the low loading and good dispersion (Li et al., 2008; Machado et al., 2012).

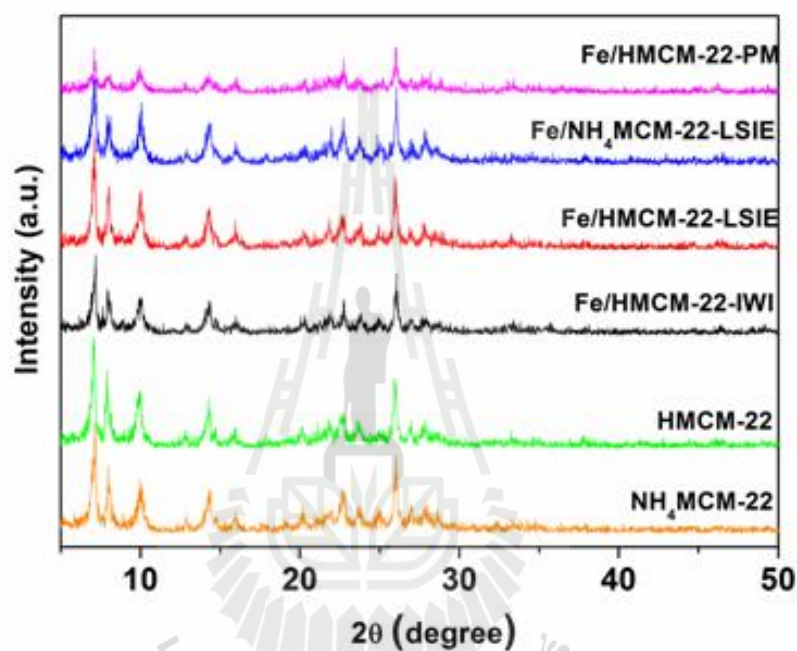


Figure 5.1 XRD patterns of zeolite MCM-22 and supported Fe catalysts: Fe/MCM-22-IWI, Fe/HMCM-22-LSIE, Fe/ NH_4 MCM-22-LSIE and Fe/HMCM-22-PM.

N_2 adsorption-desorption isotherms of zeolite MCM-22 and supported Fe catalysts are shown in Figure 5.2. The numerical data are compiled in appendix C. They were classified as type I which is a characteristic of microporous materials (Machado et al., 2012). The hysteresis loops were observed at the high pressure range indicating the interparticle of the agglomerated platelet structure for MCM-22. Their surface area, pore sizes and volumes are summarized into Table 5.1. The supported Fe

catalysts had slightly lower surface area and pore volume than the bare zeolite indicating a good Fe dispersion. Fe/MCM-22-PM had the lowest pore volume suggesting the most pore blocking.

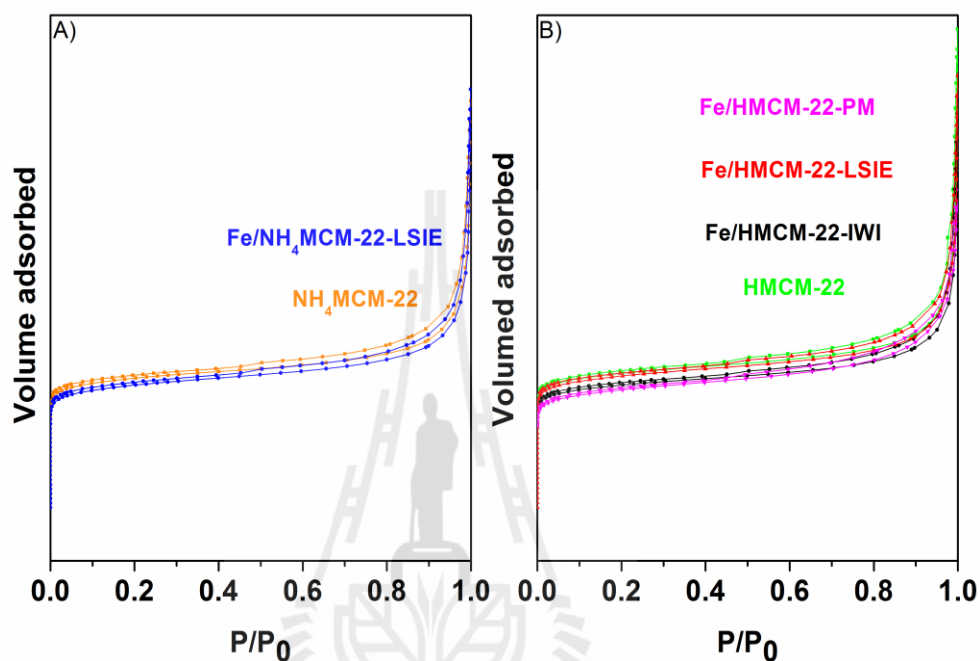


Figure 5.2 N₂ adsorption-desorption isotherms of A) NH₄MCM-22 and Fe/NH₄MCM-22-LSIE; B) HMCM-22, Fe/HMCM-22-IWI, Fe/HMCM-22-LSIE and Fe/HMCM-22-PM.

Figure 5.3 shows the morphology of MCM-22 and supported Fe catalysts. They had platelet structure which agglomerated to large particles. The particle diameters were varied from 2-13 μ m. After loaded with Fe catalysts, the platelet structure was still observed for all catalysts.

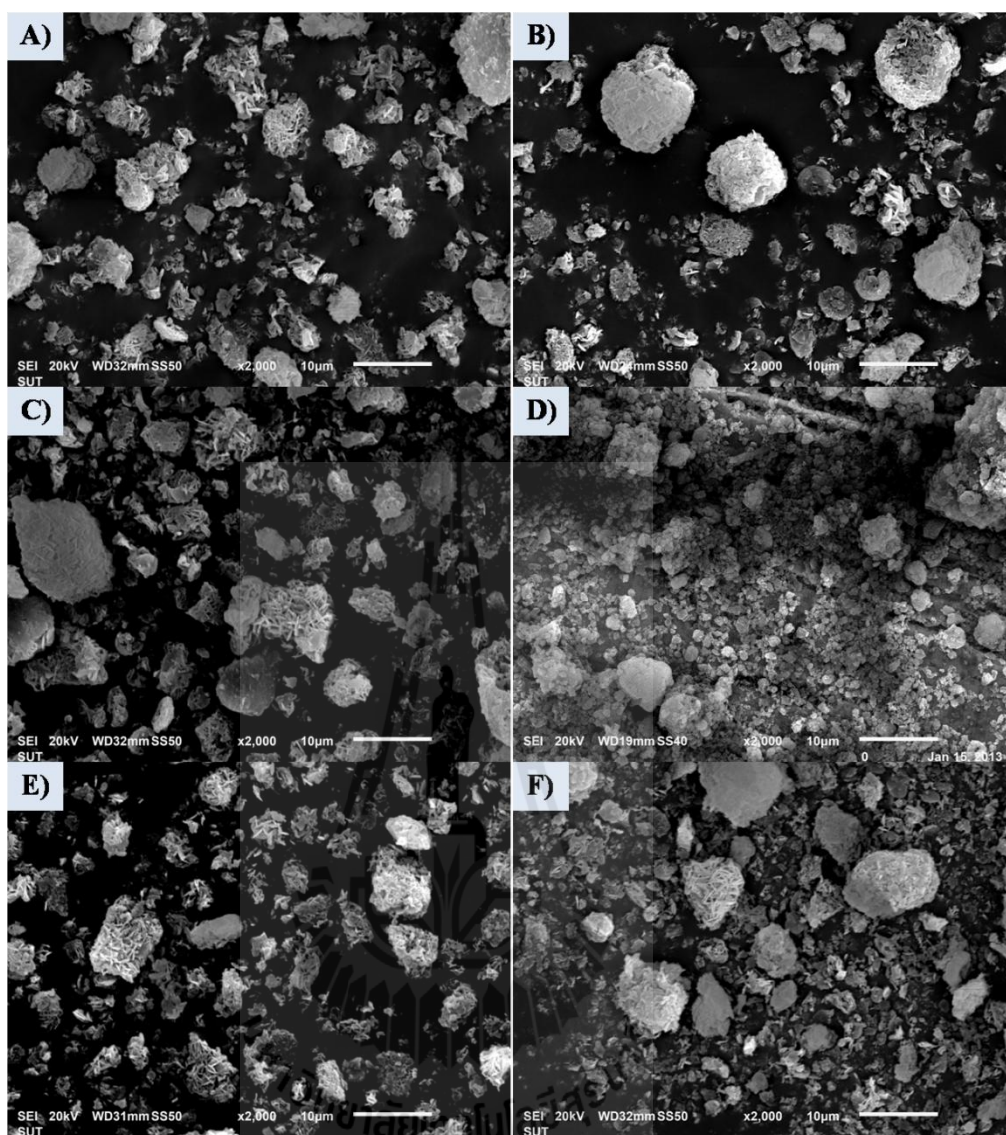


Figure 5.3 SEM images of A) HMCM-22, B) Fe/HMCM-22-IWI, C) Fe/HMCM-22-LSIE, D) Fe/HMCM-22-PM, E) NH₄MCM-22 and F) Fe/NH₄MCM-22-LSIE.

In order to understand the environment and location of Fe, all supported catalysts were analyzed by DR-UV-Visible spectroscopy. The DR UV-Vis spectra are shown as Figure 5.4. Fe/HMCM-22-LSIE and Fe/NH₄MCM-22-LSIE which had Fe contents < 1 %wt revealed the absorption bands at 211 and 273 corresponding to charge transfer from oxygen to Fe³⁺ at the ion exchangeable site of zeolite

(Høj et al., 2009; Dzwigaj et al., 2007; Kumar, 2004). Besides, a shoulder at 344 nm were assigned to charge transfer band from Fe oligomers with octahedral coordination (Høj et al., 2009; Liang et al., 2013; Esther Leena Preethi et al., 2007; Hensen, 2005). It was reported by Meloni et al. (2001) that the ion exchangeable site of the HMCM-22 was mainly (50 - 70%) in the supercages. Hence, Fe could exchange and incorporate inside the cavity of the zeolite by LSIE. In the case of Fe/HMCM-22-IWI and Fe/HMCM-22-PM which had Fe contents about 6%, the absorption bands at 211, 273, 344, 365 and 415 nm were assigned to Fe in monomer and oligomers. The additional broad band at around 518 nm was assigned to the formation of hematite particles on the external surface of the MCM-22 zeolite (Capek et al., 2005; Høj et al., 2009).

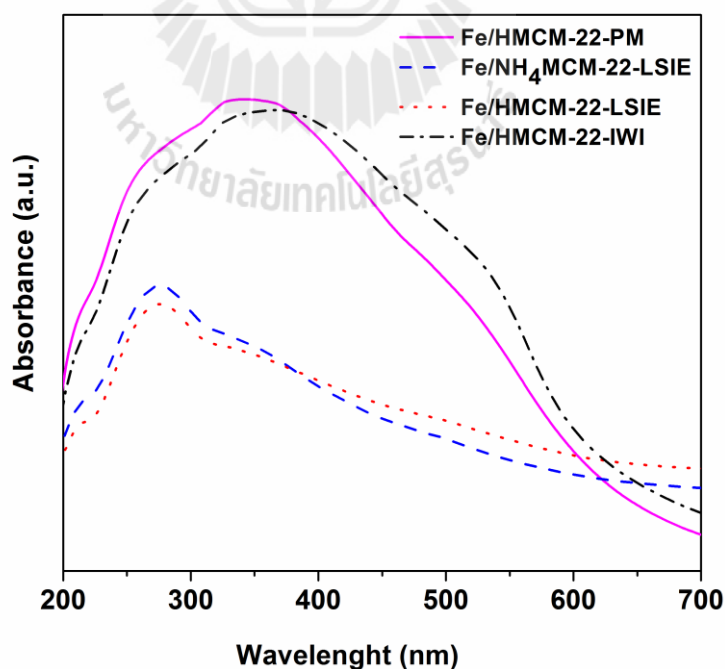


Figure 5.4 DR-UV-Vis spectra of supported Fe catalysts: Fe/MCM-22-IWI, Fe/HMCM-22-LSIE, Fe/NH₄MCM-22-LSIE and Fe/HMCM-22-PM.

XANES spectra of Fe standards and supported catalysts at K-edge are shown in Figure 5.5 A and B, respectively. The spectra of all samples were similar to that of Fe_2O_3 phase suggesting that Fe_2O_3 was the major phase. Such phase was also confirmed by Linear Combination Fitting (LCF) (Table 5.2). Moreover, the pre-edge which is a small peak before the edge region could indicate the environment of Fe because it was from the allowed electronic transition from 1s orbital to 3d orbital of Fe with tetrahedral coordination (Berlier et al., 2005). The $\text{Fe}/\text{NH}_4\text{MCM-22-LSIE}$ gave the strongest pre-edge intensity indicating the dominance of Fe with tetrahedral coordination, in other words, Fe in this catalyst resided mainly at the exchange positions.

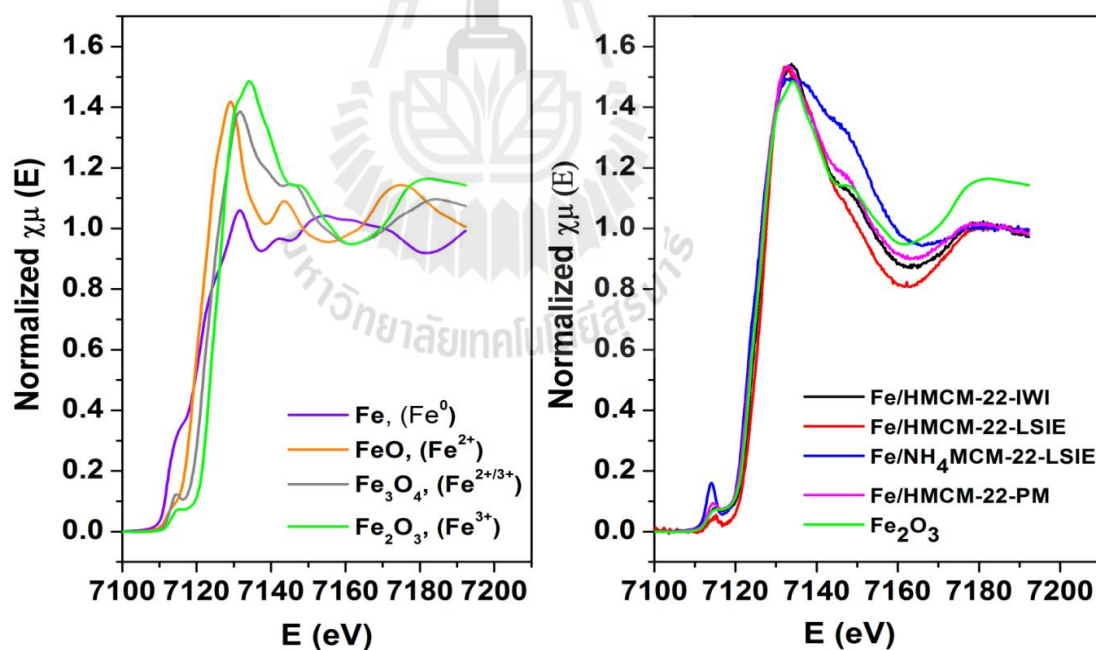


Figure 5.5 A) XANES spectra of Fe standards: Fe, FeO, Fe_3O_4 and Fe_2O_3 , B) XANES spectra of supported Fe catalysts: Fe/MCM-22-IWI, Fe/HMCM-22-LSIE, Fe/ $\text{NH}_4\text{MCM-22-LSIE}$ and Fe/HMCM-22-PM.

Table 5.2 Linear combination fitting results and pre-edge data of supported Fe catalysts.

Properties	Fe/HMCM-22-IWI	Fe/HMCM-22-LSIE	Fe/NH ₄ MCM-22-LSIE	Fe/HMCM-22-PM
Iron components (%)				
Fe ₂ O ₃	-	100.0	99.1	98.3
Fe ₃ O ₄	0.0030	-	0.9	1.7
Reliability factor, R	7115.2	0.0216	0.0259	0.0036
Pre-edge energy, (eV)	0.0788	7115.2	7114.2	7114.9
Pre-edge intensity	0.0788	0.0546	0.1601	0.0928

5.4.2 Catalytic performance in phenol hydroxylation

Phenol conversions from hydroxylation are shown in Figure 5.6. The conversions at 15 min were in the following order: Fe/NH₄MCM-22-LSIE > Fe/HMCM-22-LSIE > Fe/HMCM-22-IWI > Fe/HMCM-22-PM. After that the conversions from all samples increased and reached steady values of around 55%. The catalyst with the shortest induction period was Fe/NH₄MCM-22-LSIE. With lower Fe loading, the catalysts from LSIE gave higher turnover numbers than those from other methods. The high activity may be contributed from the abundance of Fe in tetrahedral coordination. These results are consistent with the proposed pathway that the Fe in tetrahedral coordination was more active for the phenol hydroxylation than that in octahedral coordination (Li et al., 2012).

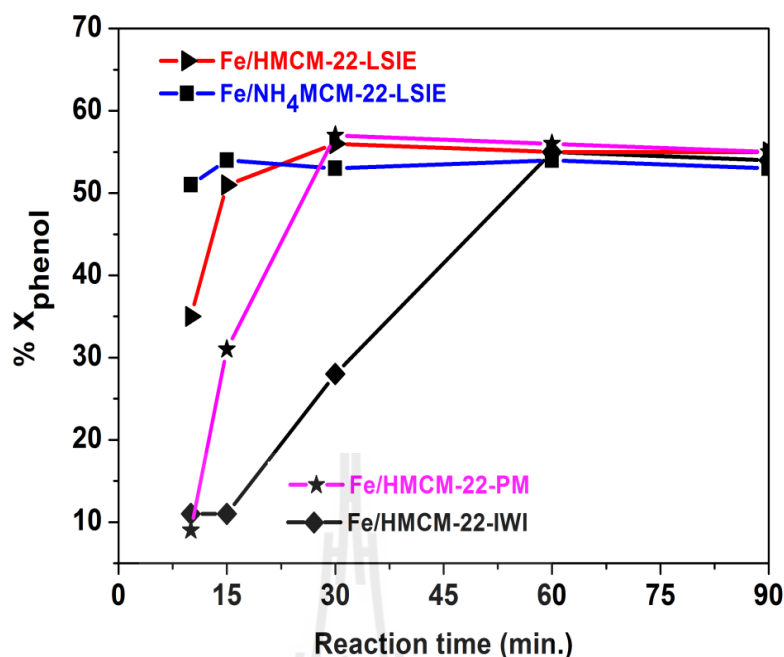


Figure 5.6 Phenol conversions on the supported Fe catalysts at 70 °C, phenol:H₂O₂ mole ratio of 1:1 and stirring condition.

Table 5.3 summarizes the product selectivity of all catalysts with the reaction time. The observed products were CAT, HQ and BQ. Based on similar conversions, percent yields of products collected at 90 min are shown in Figure 5.7. CAT was the major product followed by HQ and other products which were not detected by GC but suggested by the carbon balance. These products may be the coke deposited on the catalysts and were confirmed by TPO (see below). Fe/NH₄MCM-22-LSIE gave the highest CAT and HQ selectivities and the lowest mass loss. Moreover, a small amount of BQ was detected only at an early stage from all catalysts. It was possible that BQ was a kinetic product which transformed to other products. Allian et al. (1994) described that BQ was from the over oxidation of HQ under the excess amount of H₂O₂ (Allian et al., 1994). This phenomenon might also

occur during the reaction testing and GC analysis (Musuda et al., 1990). There were several explanations for the disappearance of BQ. Allian et al. (1994) studied the reaction of BQ with H₂O₂ using silica-alumina catalyst at 60 °C and reported that BQ could oxidize H₂O₂ to give HQ and O₂.

Table 5.3 Phenol conversions and product selectivity at various reaction times of Supported Fe catalysts.

Catalyst	Reaction time (min)	%X _{phenol}	%S _{products}			
			CAT	HQ	BQ	Others
Fe/HMCM-22-IWI	10	11	0	0	1	99
	15	11	0	0	1	99
	30	28	36	12	12	40
	60	55	38	20	1	42
	90	54	41	24	0	34
	120	55	45	26	0	29
	180	55	44	25	0	30
Fe/HMCM-22-LSIE	10	35	36	13	9	42
	15	51	41	21	2	36
	30	56	42	24	0	34
	60	55	44	25	0	31
	90	55	44	26	0	30
	120	55	44	26	0	30
	180	55	45	26	0	29
Fe/NH ₄ MCM-22-LSIE	10	51	44	25	1	31
	15	54	46	27	0	26
	30	53	49	29	0	22
	60	54	47	28	0	25
	90	53	48	29	0	23
	120	54	48	28	0	24
	180	55	47	29	0	24
Fe/HMCM-22-PM	10	9	0	0	6	94
	15	31	37	15	11	37
	30	57	36	21	1	42
	60	56	37	23	0	40
	90	55	42	27	0	31
	120	57	40	25	0	34
	180	56	42	27	0	31

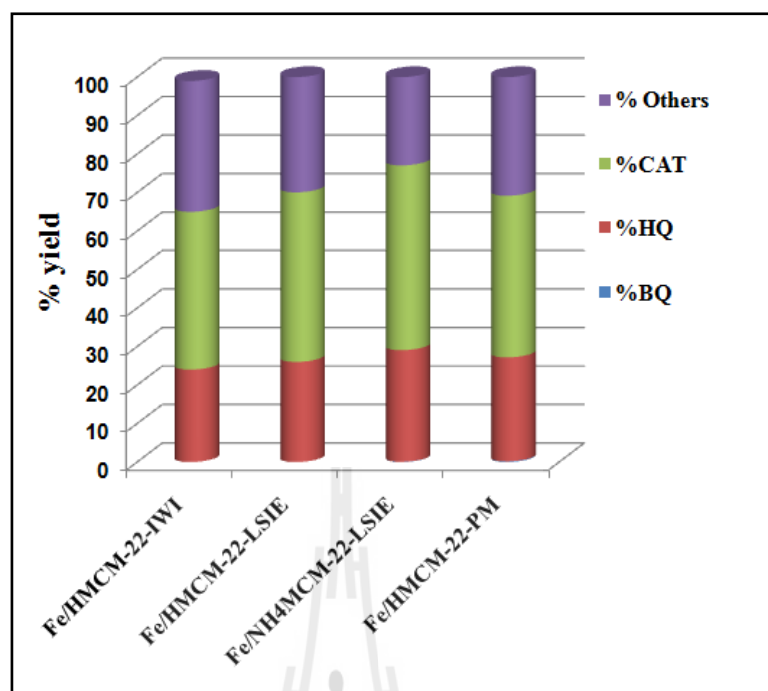


Figure 5.7 Product selectivities during phenol hydroxylation at reaction time of 90 min.

Regarding the formation of coke during the phenol hydroxylation, the physical properties change of reaction solution and catalyst could be investigated and recorded as evidence. An example of reaction solution change during the reaction by using Fe/HMCM-22-IWI as catalyst was taken as shown in Figure 5.8. Initially, the phenol solution mixed with catalysts revealing a pale orange solution. Then, the reaction started by addition H_2O_2 revealing the darkness increased with the reaction time and conversion. This happened with the similar phenomena for others catalysts in this work. The dark color of reaction solution was explained by a presence of dissolved polymer and could be partially removed by filtration (Araña et al., 2001).

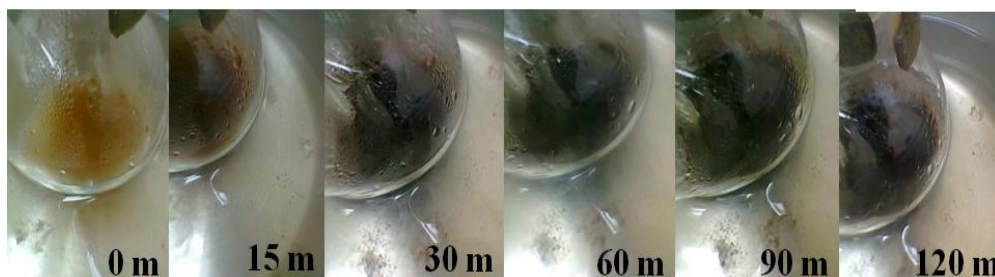


Figure 5.8 Color change of reaction solution during the phenol hydroxylation by a batch reactor.

The comparison between fresh catalyst and spent catalyst was investigated as shown in Figure 5.9. The spent catalysts became darker than the fresh one exhibiting the formation of coke on the catalysts during the reaction. More darkness could be obtained with catalysts with higher Fe content.

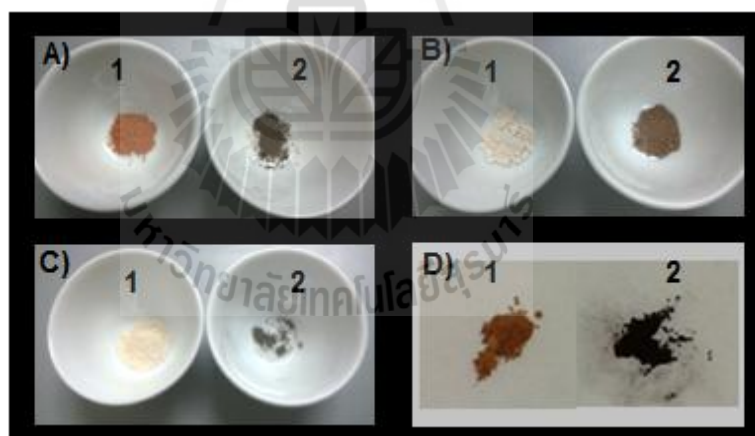


Figure 5.9 Images of fresh (1) and spent (2) catalyst for A) Fe/HMCM-22-IWI, B) Fe/HMCM-22-LSIE C) Fe/NH₄MCM-22-LSIE and D) Fe/HMCM-22-PM.

Figure 5.10 shows TPO profiles of spent catalysts which were signal of CO₂ from combustion of the coke deposited on the spent catalysts. The temperature reflected the length of carbon chain and the peak area was proportional to the amount of coke. The peaks represented between 250 and 350 °C were from light coke

deposited at the catalyst external surface. The peaks between 550 and 600 °C were from heavy coke generated inside the pore of zeolite (Guisnet et al., 2009; Ibáñez et al., 2014). The largest CO₂ signals were obtained from Fe/MCM-22-IWI with the peaks around 350 °C and 550 °C. The second largest signal was from Fe/MCM-22-PM with the peak at around 275 °C. Since the majority of active sites were outside the zeolite cavities, the coke from these samples might be generated from active sites on the external surface.

The TPO signals from Fe/NH₄MCM-22-LSIE and Fe/HMCM-22-LSIE were smaller than those from the previous cases and occurred at higher temperature around 350 °C and 600 °C. The less amount of coke may correspond to the lower Fe loading. As previous results from DR-UV-Vis, Fe was located at the ion exchange position which mostly occupied in the zeolite cavity (Meloni et al., 2001). Therefore, the coke from these samples may be generated from active sites inside the zeolite pore. Regarding to the super cages of MCM-22, the coke could formed and blocked the zeolite pore which was needed to remove at higher temperature compared with catalysts from IWI and PM.

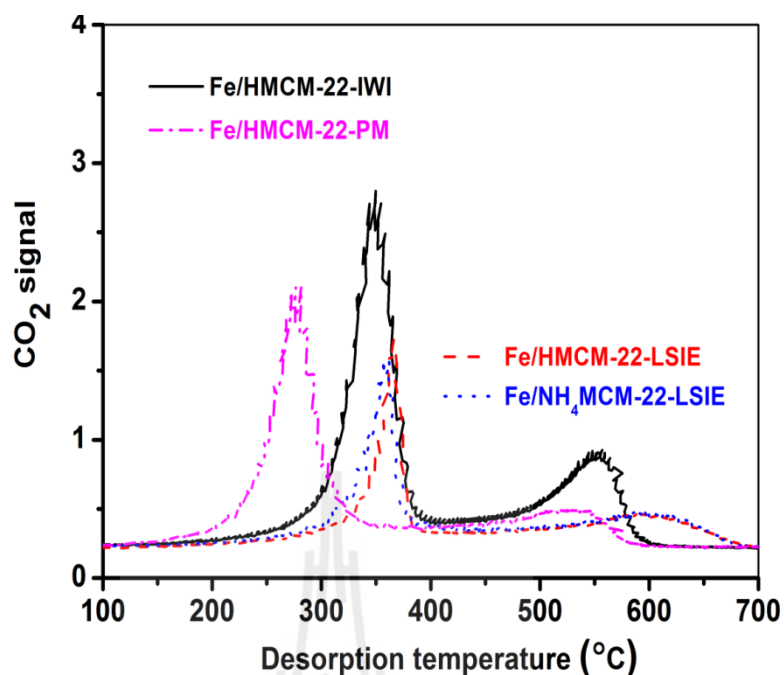


Figure 5.10 Temperature programmed oxidation profiles of spent supported Fe catalysts after one cycle of the phenol hydroxylation. Spent catalysts were calcined with the heating rate of 5 °C/min under the flowing of 3% O₂/Ar with the total flow rate 40 mL/min.

Continuously confirmation of the coke on spent catalyst, the oxidation of the spent catalysts was also carried out and monitored by FTIR measurement as a real time analysis. The peak assignments are concluded into Table 5.4. The FTIR spectra of the spent catalysts before and after oxidation are as Figure 5.11. The characteristic bands of zeolite were observed at 1997, 1866 and 1263 cm⁻¹. The peak of adsorbed water was observed at 1633 cm⁻¹ and then it was disappeared upon the oxidation. Regarding to the presence of coke on the spent catalysts, peaks at 1721, 1598, 1501 and 1474 cm⁻¹ which all assigned to carbonaceous species or coke from the

polymerization of reaction intermediates during the phenol hydroxylation were observed and they were decreased after the oxidation.

Table 5.4 Characteristic of infrareds assignments.

Phase	Bands (cm ⁻¹)	Assignments	Type of vibrations	Reference
HBEA and HMCM-22	1996, 1877	zeolite	Overtone lattice	Rintramee et al., 2012
	1263-1288	zeolite	Si-O-Si	Rintramee et al., 2012
	1634	adsorbed H ₂ O	δ O-H	Pechar and Rykl., 1979
Hydrocarbon deposited on zeolite	1721	carbonyl species	ν(C=O)	Smith et al., 1979
	1598	carbonaceous species	νC=C cyclic	Abbas et al., 2008 Merayo et al., 2013
	1508, 1501	formate	ν(COO ⁻)	Gerei et al., 1973
	1482,	carbonaceous species	νC=C cyclic	Garcia-Cortes. et al, 2003
	1474, 1467			

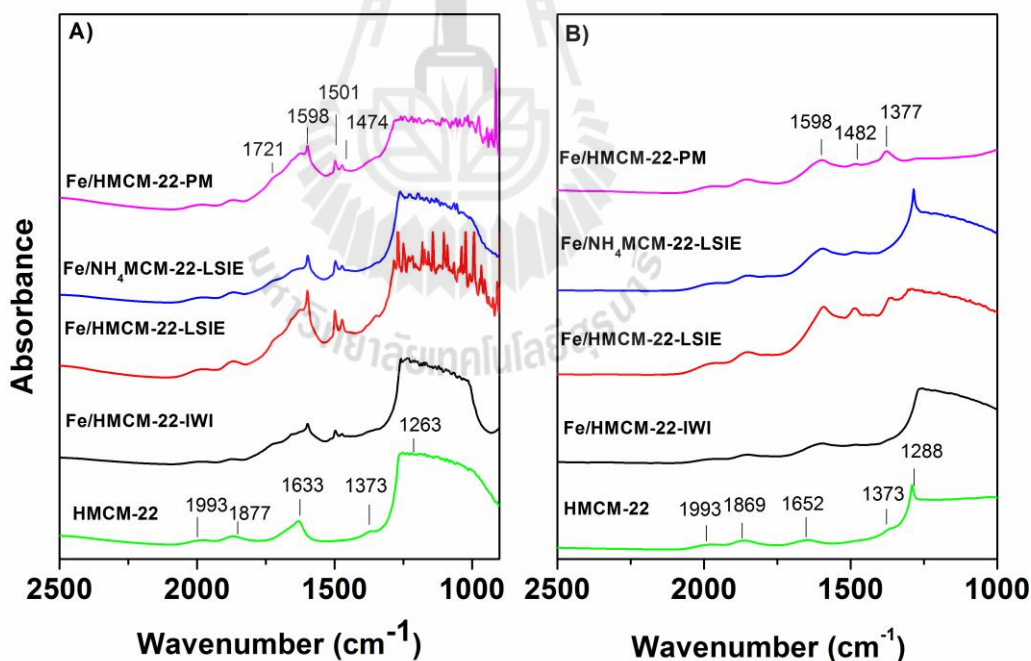


Figure 5.11 FTIR spectra of spent catalyst in a series of zeolite BEA A) before the oxidation at 25 °C and B) after the oxidation at 450 °C.

5.5 Conclusions

The Fe catalysts were loaded onto zeolite MCM-22 by incipient wetness impregnation (IWI), liquid state ion-exchange (LSIE) and physical mixing (PM). The isolated Fe_2O_3 at the ion-exchange position of zeolite prepared from LSIE was the active sites for phenol hydroxylation. The Fe/ $\text{NH}_4\text{MCM-22-LSIE}$ having Fe_2O_3 mainly in tetrahedral coordination was the best catalyst providing the shortest period to reach a steady state and the lowest mass loss from coke formation. For other cases, Fe/HMCM-22-IWI and Fe/HMCM-22-PM had Fe_2O_3 particles deposited on the external surface which were less active for the reaction. Besides, the narrow pore structure of MCM-22 could not improve the yield of HQ. To gain more details about the mass loss, the changes during phenol hydroxylation was further investigated by ATR-FT-IR technique (see Chapter VI).

5.6 References

- Abbas, O., Rebufa, C., Dupuy, N. and Kister, J. (2008). FTIR—Multivariate curve resolution monitoring of photo-Fenton degradation of phenolic aqueous solutions Comparison with HPLC as a reference method. **Talanta**. 77: 200-209.
- Allian, M., Germain, A. and Figueras, F. (1994). The formation of para benzoquinone and the mechanism of hydroxylation of phenol by hydrogen peroxide on the solid acids. **Catalysis Letters**. 28: 409-415
- Araña, J., Tello-Rendón, E., Doña-Rodríguez, J. M., Herrera-Melián, J. A., González-Díaz, O. and Pérez Peña, J. (2001). Highly concentrated phenolic wastewater treatment by the photo-Fenton reaction, mechanism study by FTIR-ATR. **Chemosphere**. 44: 1017-1023.

- Balle, P., Geiger, B. and Kureti, S. (2009). Selective catalytic reduction of NO_x by NH₃ on Fe/HBEA zeolite catalysts in oxygen-rich exhaust. **Applied Catalysis B: Environmental**. 85: 109-119.
- Berlier, G., Pourny, M., Bordiga, S., Spoto, G., Zecchina, A. and Lamberti, C. (2005). Coordination and oxidation changes undergone by iron species in Fe-MCM-22 upon template removal, activation and red-ox treatments: an in situ IR, EXAFS and XANES study. **Journal of Catalysis**. 229: 45-54.
- Capek, L., Kreibich, V., decek, J. De, Grygar, T., Wichterlova, B., Sobal, Z., Martens, J. A., Brosius, R. and Tokarova, V. (2005). Analysis of Fe species in zeolites by UV-VIS-NIR, IR spectra and voltammetry; Effect of preparation, Fe loading and zeolite type. **Microporous and Mesoporous Materials**. 80: 279-289.
- Cheng, J. C., Degnan, T. F., Beck, J. S., Huang, Y. Y., Kalyanaraman, M., Kowalski, J. A., Loehr, C. A. and Mazzone, D. N. (1999). A comparison of zeolites MCM-22, Beta, and USY for liquid phase alkylation of benzene with ethylene. **Science and Technology in Catalysis**. 121: 53-60.
- Chumee, J., Grisdanurak, N., Neramittagapong, S. and Wittayakun, J. (2009). Characterization of AlMCM-41 synthesized with rice husk silica and utilization as supports for platinum iron catalysts. **Brazilian Journal of Chemical Engineering**. 26: 367-373.
- Corma, A., Corell, C. and Pérez-Pariente, J. (1995). Synthesis and characterization of MCM-22 zeolite. **Zeolites**. 15: 2-8.
- Delitala, C., Alba, M. D., Becerro, A. I., Delpiano, D., Meloni, D., Musu, E. and Ferino, I. (2009). Synthesis of MCM-22 zeolites of different Si/Al ratio and

their structural, morphological and textural characterisation. **Microporous and Mesoporous Materials**. 118: 1-10.

Dzwigaj, S., Stievano, L., Wagner, F-E. and Che, M. (2007). Effect of preparation and metal content on the introduction of Fe in BEA zeolite, studied by DR UV-vis, EPR and Mossbauer spectroscopy. **Journal of Physics and Chemistry of Solids**. 68: 1885-1890.

Esther Leena Preethi, M., Revathi, S., Sivakumar, T., Manikandan, D., Divakar, D., Valentine Rupa, A. and Palanichami, M. (2007). Phenol Hydroxylation Using Fe/Al-MCM-41 Catalysts. **Catalysis Letters**. 120: 56-64.

Garcia-Cortes, J. M., Perez-Ramirez, J., Rouzaud, J. N., Vaccaro, A. R., Illan-Gomez, M. J. and Salinas-Martinez De Lecea, C. (2003). On the structure sensitivity of deNO_x HC-SCR over Pt-beta catalysts. **Journal of Catalysis**. 218: 111-122.

Gerei, S. V., Rozhkova, E. V. and Gorokhovatsky, Y. B. (1973). Propylene and oxygen chemisorption on cupric oxide and cuprous oxide catalysts. **Journal of catalysis**. 28: 341-350.

Guisnet, M., Costa, L. and Ribeiro F. R. (2009). Prevention of zeolite deactivation by coking. **Journal of Molecular Catalysis A: Chemical**. 305: 69-83

Hensen, E., Zhu, Q., Janssen, R., Magusin, P., Kooyman, P. and Vansanten, R. (2005). Selective oxidation of benzene to phenol with nitrous oxide over MFI zeolites: 1. On the role of iron and aluminum. **Journal of Catalysis**. 233: 123-135.

Høj, M., Beier, M. J., Grunwaldt, J-D. and Dahl, S. (2009). The role of monomeric iron during the selective catalytic reduction of NO over Fe-BEA zeolite catalysts. **Applied Catalysis B: Environmental**. 93: 166-176.

- Ibáñez, M., Artetxe, M., Lopez, G., Elordi, G., Bilbao, J., Olazar, M. and Castano, P. (2014). Identification of the coke deposited on an HZSM-5 zeolite catalyst during the sequenced pyrolysis–cracking of HDPE. **Applied Catalysis B: Environmental**. 436: 148-149.
- Kumar, M. S., Schwidder, M., Grünert, W. and Brückner, A. (2004) On the nature of different iron sites and their catalytic role in Fe-ZSM-5 DeNO_x catalysts: new insights by a combined EPR and UV/VIS spectroscopic approach. **Journal of Catalysis**. 227: 384-397.
- Lawton, S. L., Leonowicz, M. E., Partridge, R. D., Chu, P. and Rubin, M. K. (1998). Twelve-ring pockets on the external surface of MCM-22 crystals. **Microporous Mesoporous Materials**. 23: 109-117.
- Leonowicz, M. E., Lawton, J. A., Lawton, S. L. and Rubin, M. K. (1994). MCM-22: A molecular sieve with two independent multidimensional channel system. **Science**. 264: 1910-1913.
- Li, L., Shen, Q., Li, J., Hao, Z., Xu, Z. P. and Max Lu, G. Q. (2008). Iron-exchanged FAU zeolites: Preparation, characterization and catalytic properties for N₂O decomposition. **Applied Catalysis A: General**. 344: 131-141.
- Li, B., Xu, J., Liu, J., Zuo, S., Pan, Z. and Wu, Z. (2012). Preparation of mesoporous ferrisilicate with high content of framework iron by pH-modification method and its catalytic performance. **Journal of Colloid and Interface Science**. 366: 114-119.
- Liang, X., Yang, R., Li, G. and Hu, C. (2013). Phenol hydroxylation over Fe-incorporated mesoporous materials prepared by coprecipitation. **Microporous and Mesoporous Materials**. 182: 62-72.

- Machado, V., Rocha, J., Carvalho, A. P. and Martins, A. (2012). Modification of MCM-22 zeolite through sequential post-synthesis treatments. Implications on the acidic and catalytic behavior. **Applied Catalysis A: General**. 329: 445-446.
- Matsuda, M., Ohyachi, K. and Matsuura, T. (1990). Chem Express 5: 533-536.
- Meloni, D., Laforge, S., Martin, D., Guisnet, M., Rombi, E. and Solinas, V. (2001). Acidic and catalytic properties of H-MCM-22 zeolites 1. Characterization of the acidity by pyridine adsorption. **Applied Catalysis A: General**. 215: 55-66.
- Merayo, N., Hermosilla, D., Negro, C. and Blanco, Á. (2013). On-line FTIR as a novel tool to monitor Fenton process behavior. **Chemical Engineering Journal**. 232: 519-526.
- Pechar, F. and Rykl, D. (1981). Infrared spectra of natural zeolites of the stilbite group. **Chemické Zvesti**. 35: 189-202.
- Rintramee, K., Föttinger, K., Rupprechter, G. and Wittayakun, J. (2012). Ethanol adsorption and oxidation on bimetallic catalysts containing platinum and base metal oxide supported on MCM-41. **Applied Catalysis B: Environmental**. 115-116: 225-235.
- Smith, A. L. (1979). Applied infrared spectroscopy: fundamentals, techniques, and analytical problem solving. **Wiley—Interscience**. pp. 336.
- Rubin, M. K. and Chu, P. (1990). Composition of synthetic porous crystalline material, Its synthesis and use. **US Patent No.4**. 954: 325.
- Wu, Y., Ren, X., Lu, Y. and Wang, J. (2008). Crystallization and morphology of zeolite MCM-22 influenced by various conditions in the static hydrothermal synthesis. **Microporous and Mesoporous Materials**. 112: 138-146.

CHAPTER VI

STUDY OF MASS LOSS IN PHENOL

HYDROXYLATION OVER IRON CATALYST

SUPPORTED ON ZEOLITE MCM-22 BY ATTENUATED

TOTAL INTERNAL REFLECTANCE WITH FOURIER

TRANSFORM INFRARED SPECTROSCOPY

6.1 Abstract

The aim of this part was to investigate the changes during the phenol hydroxylation by Attenuated Total Internal Reflectance with Fourier Transform Infrared Spectroscopy (ATR-FT-IR). The catalysts were Fe/HMCM-22-IWI, Fe/HMCM-22-IE, Fe/NH₄MCM-22 and Fe/HMCM-22-PM. ZnSe was used as an internal reflectance element (IRE). Catalysts were coated on the ZnSe and the reaction occurred on the surface. Fe/NH₄MCM-22 was used as the model to optimize the condition for the reaction by ATR-FT-IR. The parameters in this work were phenol/H₂O₂ molar ratio, catalyst amount, condition (static vs. flowing), flow rate and reaction temperature. The best condition was carried out under the flowing condition at 40 °C. From the infrared spectra, a broad band at 1600-1800 cm⁻¹ which was assigned to organic acids from the deep oxidation of HQ, CAT and BQ predominately increased with the reaction time. Besides, the peak at 2460 cm⁻¹ corresponded to CO₂ from a complete oxidation of organic acids. In another way, the formation of organic

acids during the phenol hydroxylation on Fe/HMCM-22-IWI in a batch process lowered the pH of reaction mixture with the reaction time and the pH became constant at 60 min. The organic acids were also confirmed by high pressure liquid chromatography (HPLC). The formation of organic acid may correlate to mass loss during the phenol hydroxylation.

6.2 Introduction

Regarding to the results from Chapter V, Fe/NH₄MCM-22-LSIE was a promising catalyst for phenol hydroxylation in a batch process since the reaction reached a steady state within 10 min. Therefore, it is interesting to use it such a catalyst for industry. Concerning to the mass loss, it was observed selectively around 30%. Many mechanisms for the phenol hydroxylation have been proposed. There are two possible ways initiated by either hydroxyl radical or the phenoxy radical. Choi and co-workers (2006) proposed the formation of hydroxyl radical from the reaction between hydrogen peroxide and iron catalyst. The phenol was oxidized by a hydroxyl radical to CAT and HQ. The CAT and HQ might be degraded to organic acids and finally to CO₂ (Okamoto et al., 1985; Matthews and McEvoy, 1992; Alnaizy and Akgerman, 2000). Meyer and co-workers (1965) proposed another mechanism that the phenoxy radical initiated the phenol hydroxylation instead of hydroxyl radical to yield CAT and HQ. Then they could further polymerize to coke product getting dark solution after the reaction (Meyer et al., 1965; Xiong et al., 2000).

To gain deeply understanding about the causes of mass loss from the reaction, the reaction pathways were studied by Attenuated total internal reflectance with Fourier transform infrared spectroscopy (ATR-FT-IR).

6.3 Experiment

6.3.1 Preparation of zeolite MCM-22 supports and supported Fe catalysts

Zeolite MCM-22 in ammonium and proton forms was synthesized according to an established procedure by Corma et al., 1995. They were used as supports for the Fe catalysts. $\text{Fe}(\text{NO}_3)_3 \cdot 9\text{H}_2\text{O}$ was used as Fe precursor to load onto the zeolite supports by incipient wetness impregnation (IWI), liquid state ion exchange (LSIE) and physical mixing (PM) methods. Details of zeolite supports and supported Fe catalysts preparation were described as topics 5.3.2 and 5.3.3 in the Chapter V.

6.3.2 Batch reactor for phenol hydroxylation

The catalytic testing was performed in a batch process as described in a topic of 3.3.6 in Chapter III. The conversion of phenol to CAT, HQ and BQ were determined by a gas chromatograph (SHIMAZU 14A series) equipped with an ID-BP1 coated capillary column and a flame ionization detector.

Organic acids occurring in the phenol hydroxylation were analyzed by high performance liquid chromatography (HPLC), Agilent Technologies with ZORBAX RRHD SB-C-18 column and UV-Visible detector. The 0.40 mL of reaction mixture was withdrawn by a glass syringe and the catalyst was separated by a nylon membrane cartridge filter with the pore diameter of 0.2 micron. The 10 μL of the sample was injected to the injection port at room temperature. The 0.1N H_2SO_4 aqueous solution was used as the eluent under the isocratic analysis with the flow rate of 0.4 mL/min. The samples were measured at the following wavelength: 254 nm for phenol, HQ, CAT, BQ and 210 nm for oxalic acid, formic acid, acetic acid.

6.3.3 Instrumental setting for ATR – FT-IR

ATR-FT-IR technique was done by a real time analysis. The ZnSe was an internal reflectance element (IRE). The supported Fe catalyst was deposited on surface of ZnSe in the following procedure. ZnSe was fixed on a preparation holder as shown in Figure 6.1A. The catalyst was suspended in ethanol and sonicated for 2 min. The obtained slurry was dispersed onto the surface of ZnSe by a dropper, air-dried at room temperature and at 80 °C for 4h in a hot-air oven. Finally, the catalyst coated - ZnSe was obtained as shown in Figure 6.1B. Figure 6.1C shows the equipment set up for the ATR cell. The ATR cell was assembled by placing the coated - ZnSe among the stainless steels plates by having rubber-rings supported on the top and bottom of the ZnSe. The cell was attached to a sample holder and tightens by screws as shown in Figure 6.1D. The cell was heated to the target temperature by hot water circulated from a water bath. The golden part was connected to the ATR cell as shown in Figure 6.1E. Hot water was circulated through the golden part from the inlet and outlet. The ATR cell was placed inside the IR spectrometer. The measurement was done on a BRUKER FT-IR spectrophotometer, VERTEX series, equipped with a N₂ purge unit. The cell position was adjusted to obtain the maximum intensity. The dash line shows the direction of infrared light from the IR source to detector. IR spectrum of the coated ZnSe was recorded. Then solution was pumped through the coated ZnSe by a peristaltic pump. IR spectra were recorded in an absorption mode with 4 cm⁻¹ resolution. Signal of water was subtracted from all spectra.

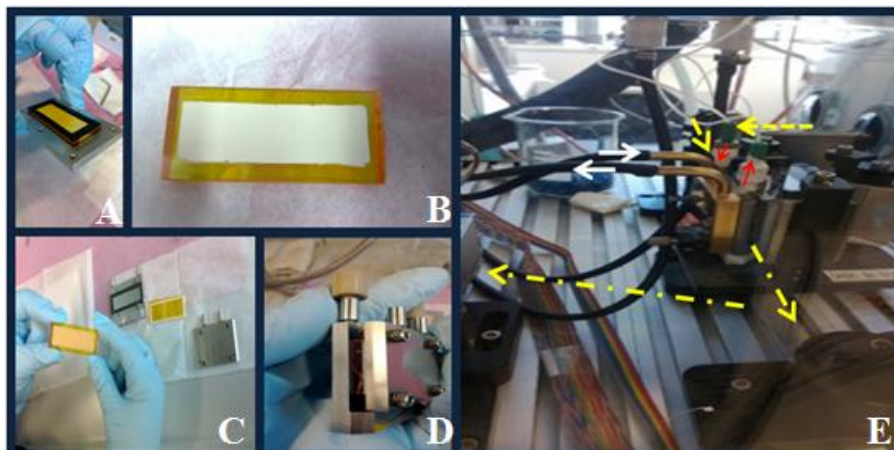


Figure 6.1 ATR-FT-IR setup: A) ZnSe on a preparation holder, B) catalyst coated on ZnSe, C) assembling of the ATR cell, D) ATR cell and E) positioning of ATR cell in the IR spectrometer.

6.3.4 Phenol adsorption by ATR-FT-IR technique

Investigation of phenol adsorption was conducted on only Fe/NH₄MCM-22-LSIE. The 40 mg of sample was deposited onto the surface of ZnSe with the method described above. Water was subtracted as background for the measurement. The 0.3332M of phenol aqueous solution was flowed through the coated ZnSe with the flow rate of 0.05mL/min. The IR spectra were recorded from 900 cm⁻¹ to 4000 cm⁻¹ for every 10 min.

6.3.5 Phenol hydroxylation by ATR-FT-IR technique

The phenol hydroxylation was studied with a real time analysis by ATR-FT-IR technique. An aqueous phenol solution (0.3332 M) was flowed through the coated ZnSe cell. IR spectra was recorded and defined as the reaction at 0 min. Then, a mixture of 0.3332 M phenol aqueous solution and 30% H₂O₂ with the appropriate mole ratio were passed through the coated ZnSe to start the reaction. The IR spectra

were recorded with the reaction time from 900 to 4000 cm^{-1} with a speed of 9 scans /min. IR spectra of aqueous solution of phenol, HQ, CAT, BQ, resorcinol, H_2O_2 and mixed standard were separately recorded as standard spectra for the reaction. However, the organic acids could not be monitored in this experiment owing to the pH limitation of ZnSe crystal (working range of pH 5 - 9) (Andanson and Baiker, 2010). The IR spectra of organic acids including formic, acetic and oxalic acid were reported in literature (Abbas et al., 2008).

6.4 Results and discussion

6.4.1 IR spectra for aromatic hydrocarbons

Figure 6.2A) displays the IR spectra of aromatic hydrocarbons used as standards for the phenol hydroxylation by ATR-FT-IR technique including aqueous solutions of phenol, HQ, CAT, BQ and mixed hydrocarbons (40% phenol + 9% BQ + 15% HQ + 36% CAT). IR spectra of all standards overlap with each other and difficult to distinguish under the presence of phenol reactant. The peak assignments are included into Table 6.1. Besides, the phenol hydroxylation was conducted in a batch process at 70 °C for comparison. The samples were withdrawn at the interval time. IR spectra of the samples from reaction were recorded as shown in Figure 6.2 B). An additional broad band at 1634 cm^{-1} was observed at 20 min and became larger with the reaction time. Moreover, other broad bands with the centre at 1710 and 1792 cm^{-1} were observed at 60 min and 90 min. Abbas and co-workers (2008) studied photo-Fenton degradation of phenolic aqueous solution by using ATR-FT-IR techniques. Organic acids were observed from the deep oxidation of phenolic compounds and analyzed by HPLC (Zazo et al., 2005; Zhou et al., 2011; Alnaizy and

Akgerman, 2000). The presence of organic acids led to the broad bands at 1620, 1708 and 1724 cm^{-1} as shown in figure 6.3 (Abbas et al., 2008; Merayo et al., 2013). These bands corresponded to the vibration of C=O group within organic acid molecules (Jung et al., 2003). In this respect, the organic acids could be produced by the Fe/HMCM-22-IWI in a batch reactor. To gain more information on the phenol hydroxylation, the ATR-FT-IR was further studied under various conditions.

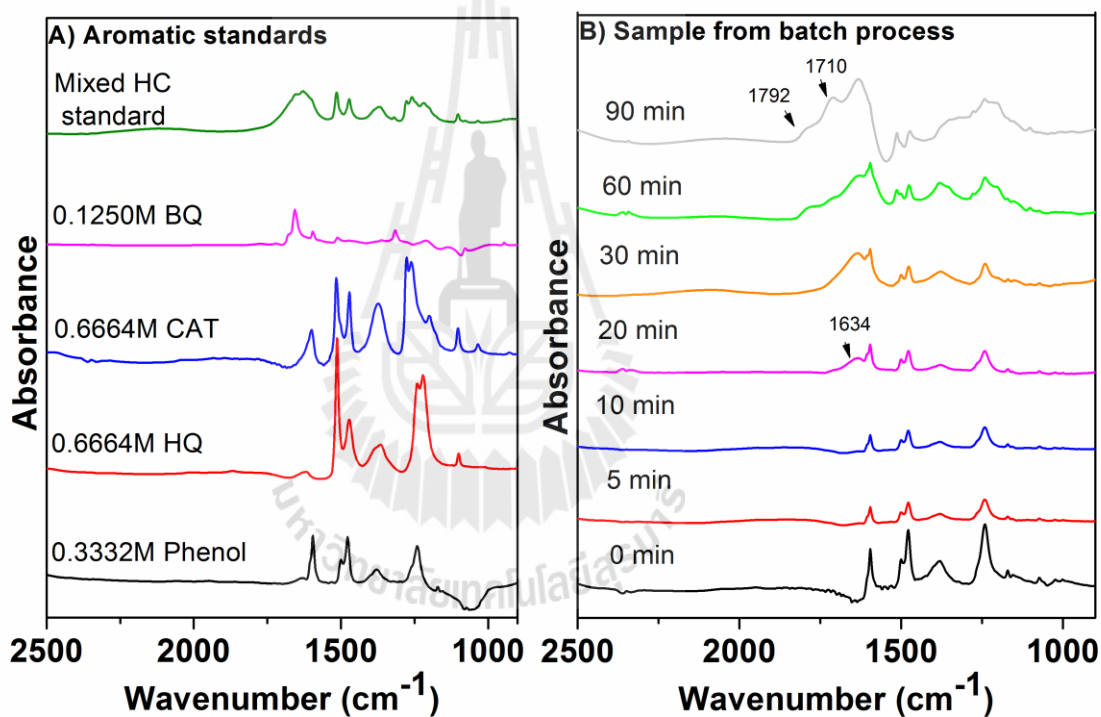


Figure 6.2 A) Aromatic hydrocarbon standards on catalyst coated IRE at 40 °C, B) reaction sample of phenol hydroxylation from batch process on bare ZnSe at 40 °C. The phenol hydroxylation condition: phenol/ H_2O_2 molar ratio of 1/1 under stirring of 700 rpm at 70 °C.

Table 6.1 Characteristic of infrareds assignments of phenolic compounds.

Wavenumber (cm ⁻¹)				Type of vibration	Functional groups	References
Phenol	CAT	HQ	BQ			
-	-	-	1657		quinone	
1597	1600	1514	-	νC=C	-C=C cyclic	Abbas et al., 2008 Merayo et al., 2013
1498	1514	1473	-			
1475	1473	-	-			
1379	1371	1365		O-H def	O-H def and νC-O phenol	
1239	1264	1239	1316			
1170	1200	1220				
-	1277	-	-	νC-O	-O-arryl	
1074	1101	1100	1079	δ=C-H	=C-H aromatic	
	1034					

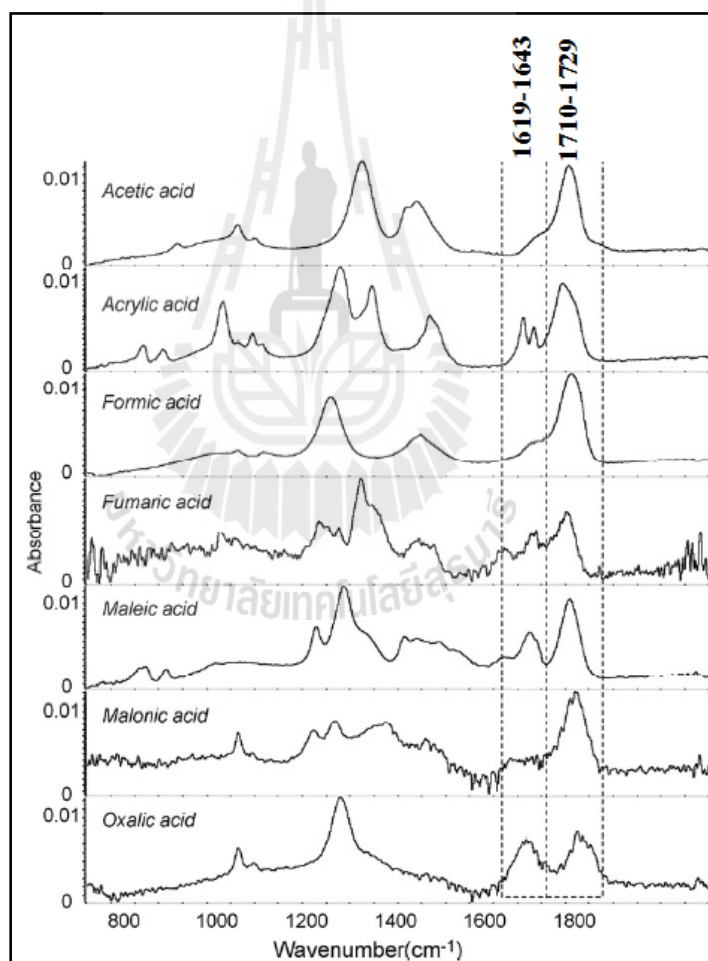


Figure 6.3 IR spectra of organic acid solutions by Abbas et al. (2008).

6.4.2 Phenol adsorption by ATR-FT-IR technique

According to the results from Chapter V, Fe/NH₄MCM-22-LSIE was the

best catalyst for phenol hydroxylation in a batch process giving the highest activity, product selectivity and lowest mass loss. Therefore, ATR-FT-IR measurement was carried out by using Fe/NH₄MCM-22-LSIE as a model catalyst to survey the suitable condition. Figure 6.4 shows the phenol adsorption on Fe/NH₄MCM-22-LSIE at 40 °C. Water was subtracted as a background. IR spectra at 0 min indicated the characteristic peak of phenol compound. The peak assignments for phenol are concluded into Table 6.1. The IR spectra did not change with the adsorption time until 300 min indicating that the reaction did not take place in the absence of H₂O₂.

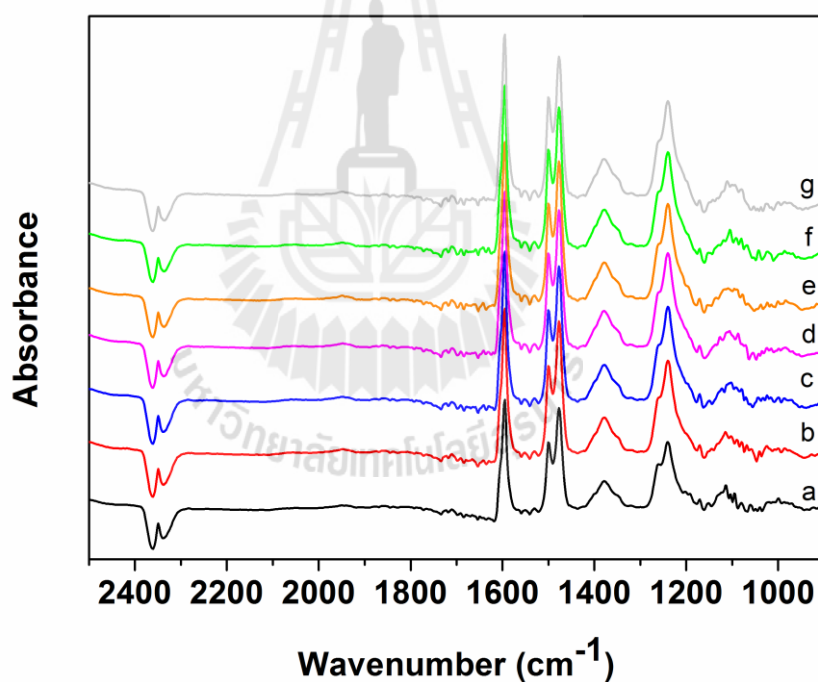


Figure 6.4 Phenol adsorption on Fe/NH₄MCM-22 catalyst at 40 °C at different adsorption time in minute a) 0, b) 30, c) 60, d) 120, e) 180, f) 240 and g) 300 min.

6.4.3 Phenol hydroxylation on bare ZnSe monitored by ATR-FT-IR technique

The control reaction was monitored on the bare IRE at 40 °C. The reactant

mixture, 0.3332 M phenol and 30% H₂O₂ with the phenol/H₂O₂ molar ratio of 1/3, was passed through the bare ZnSe with the flow rate of 0.05 mL/min. Figure 6.5 shows the progress of the control reaction with the reaction time. There was no change on the peak position of phenol. Thus, phenol hydroxylation did not occur in the absence of catalyst by ATR-FT-IR measurement. However, the absorbance increased as plateau with the centre at around 1700 cm⁻¹ and 900 cm⁻¹. This phenomenon was from the presence of H₂O₂.

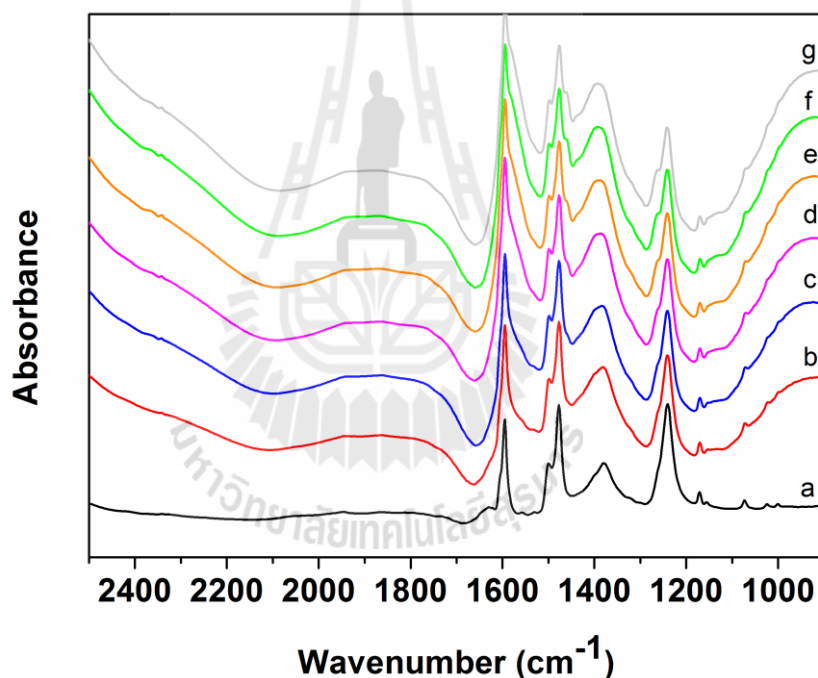


Figure 6.5 Phenol hydroxylation with phenol/H₂O₂ of 1/3 on bare ZnSe at 40 °C the reaction time in minute a) 0, b) 30, c) 60, d) 120, e) 180, f) 240 and g) 300.

6.4.4 Optimization the phenol hydroxylation condition for ATR-FT-IR technique

In this part, the phenol hydroxylation was performed in various conditions. There were factors of study following as effect of catalyst content, effect of reaction type, effect of flow rate of reactant mixture, effect of Phenol/H₂O₂ ratio in reactant mixture and effect of reaction temperature.

6.4.4.1 Effect of catalyst content on the phenol hydroxylation under static condition

According to the principle of ATR-FT-IR, the infrared beam came into contact with the ZnSe crystal and generated the evanescence wave which is penetrate the surface species on the coated-ZnSe crystal (Bürgi, 2006). The infrared intensity depended on the content of sample coated on the ZnSe crystal. However, an optimum amount of sample should be determined to obtain the best infrared signals. In order to investigate amount of sample, the various amount of Fe/NH₄MCM-22-LSIE with 12.5, 25.0 and 40.0 mg were dispersed in ethanol and dropped onto the ZnSe. Afterward they were tested in phenol hydroxylation under static condition at 40 °C. The IR spectra were recorded with the reaction time as shown in Figure 6.6. All IR spectra exhibit the similar features. The catalyst of 40.0 mg was the suitable one still giving well defined and high intense signals. Moreover, the catalyst was the most stable deposited on ZnSe during the reaction. The presence of CO₂ peak was slightly observed at 2341 cm⁻¹. It was produced from the oxidation of organic acids under the excess amount of oxidant (Zazo et al., 2005).

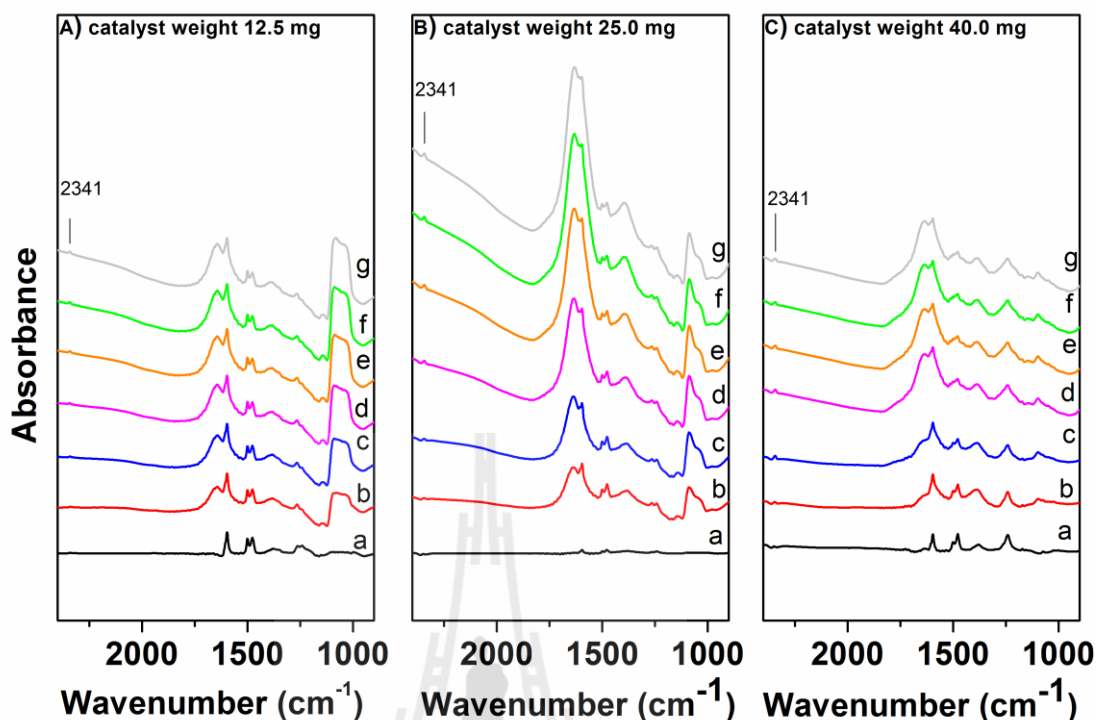


Figure 6.6 Phenol hydroxylation on Fe/NH₄MCM-22-LSIE with phenol/H₂O₂ of 1/3 under static condition at 40 °C with catalyst weight of A) 12.5 mg, B) 25.0 mg and C) 40.0 mg at the reaction time in minute: a) 0, b) 30, c) 60, d) 120, e) 180, f) 240 and g) 300 min.

6.4.4.2 Effect of reaction condition on the phenol hydroxylation

The phenol hydroxylation was compared between static and flow conditions. Under the static condition, the reactant mixture was flowed through the catalyst-coated ZnSe until completely filled the reaction space then it was stopped and monitored with the times. In the flow condition, the reactant mixture was continuously flowed through the catalyst-coated ZnSe with the flow rate of 0.5 mL/min. Figure 6.7 shows IR spectra of phenol hydroxylation in both conditions. They also show similar peak patterns. CO₂ peak stayed longer under static condition.

However, the phenol hydroxylation in static condition was not suitable for the ATR-FT-IR measurement because O_2 gas produced from the H_2O_2 decomposition could generate high pressure during the experiment and damage the ATR cell. Such problem could be avoided by using the flow condition.

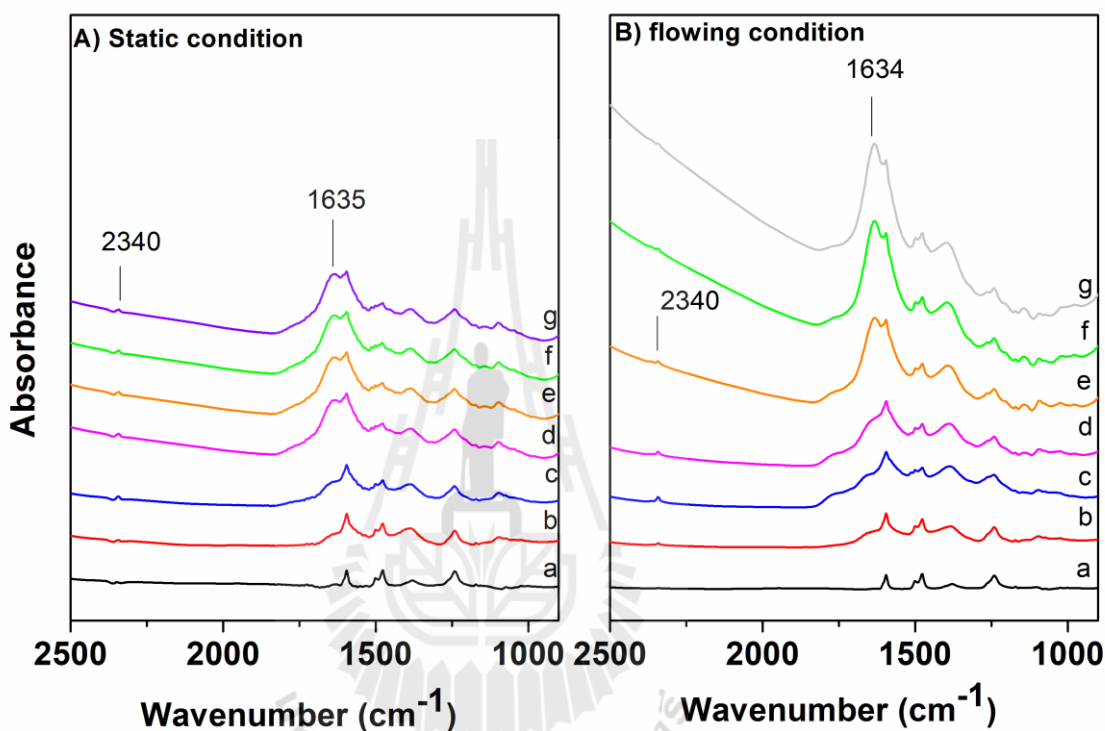


Figure 6.7 Phenol hydroxylation on Fe/ NH_4 MCM-22-LSIE with phenol/ H_2O_2 of 1/3 at 40 °C under A) static, B) flow condition at the reaction time in minute: a) 0, b) 30, c) 60, d) 120, e) 180, f) 240 and g) 300 min

6.4.4.3 Effect of flow rate of reactant mixture on the phenol hydroxylation

The flow rate of the reactant mixture was varied at 0.5, 0.1 and 0.05 mL/min. with a peristaltic pump. As shown in figure 6.8 C), the IR spectra observed from 0.05 mL/min provided well defined spectra. CO_2 peak was clearly

observed at 2341 cm^{-1} when compared to other conditions. The reactant mixture had high contact time to retain and react with the surface catalyst giving more detail spectra. Therefore, the optimum flow rate of reactant mixture was 0.05 mL/min .

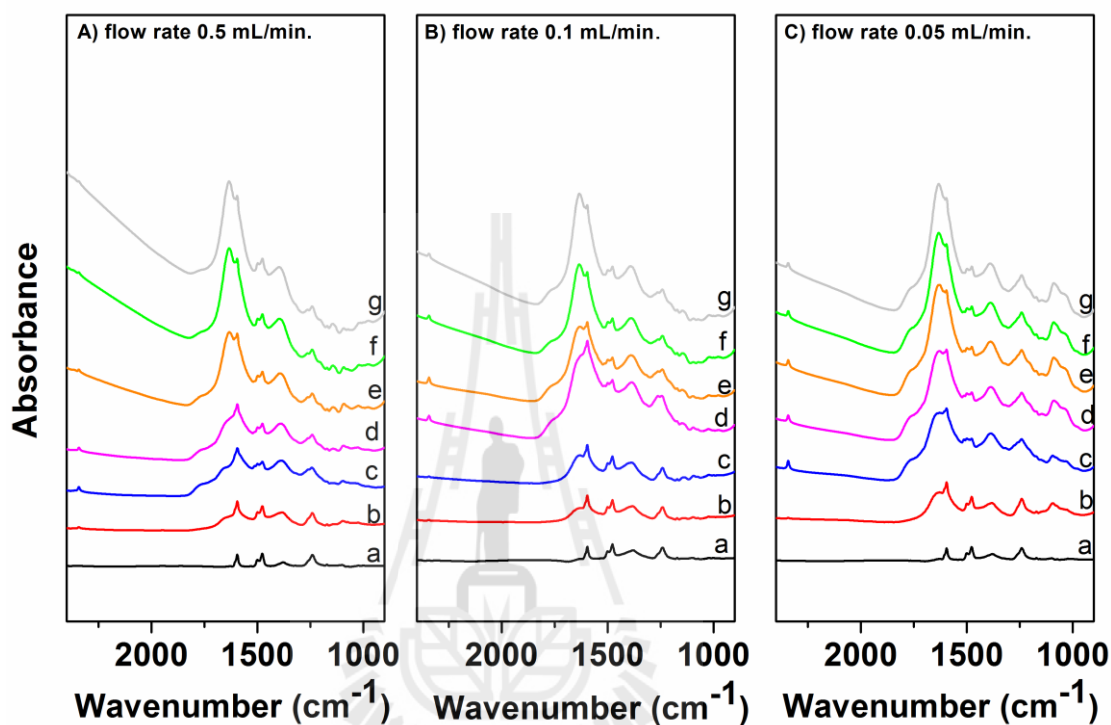


Figure 6.8 Phenol hydroxylation with phenol/H₂O₂ of 1/3 on Fe/NH₄MCM-22-LSIE catalyst at 40 °C under flow condition with the flow rate of A) 0.5 mL/min, B) 0.1 mL/min and C) 0.05 mL/min at the reaction time in minute: a) 0, b) 30, c) 60, d) 120, e) 180, f) 240 and g) 300 min.

6.4.4.4 Effect of phenol/H₂O₂ of reactant mixture on the phenol hydroxylation

The phenol/H₂O₂ ratio was an important factor for the reaction. With high amount of H₂O₂, the deep oxidation could be monitored to yield high amount of CO₂. The phenol/H₂O₂ = 1/1 and 1/3 were compared. The results are

showed as Figure 6.9. The features of spectra are similar for both conditions. For the phenol/H₂O₂ molar ratio of 1/3, CO₂ peaks were observed from 60 min. High amount of H₂O₂ led to the deep oxidation giving CO₂. Moreover, the intensity of CO₂ peak was proportional to the amount of H₂O₂ (Peres et al., 2010).

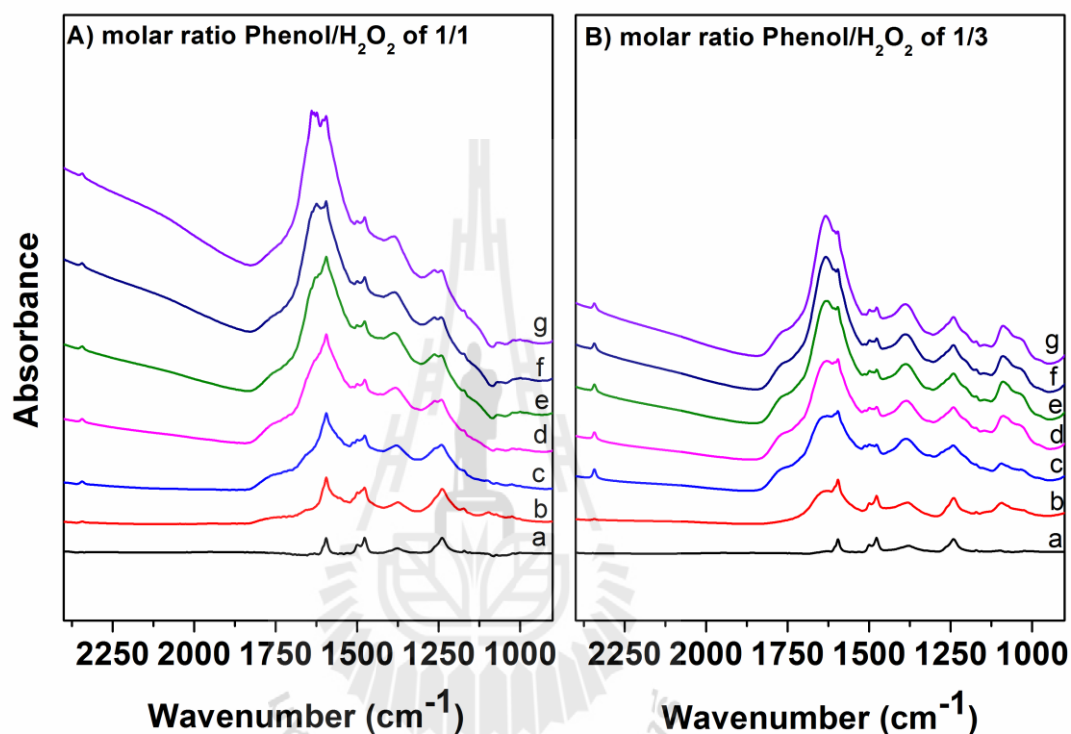


Figure 6.9 Phenol hydroxylation on Fe/NH₄MCM-22-LSIE at 40 °C under flowing condition with the phenol/H₂O₂ ratio of reactant mixture A) 1:1 and B) 1:3 at the reaction time in minute: a) 0, b) 30, c) 60, d) 120, e) 180, f) 240 and g) 300 min.

6.4.4.5 Effect of reaction temperature on the phenol hydroxylation

In order to investigate the reaction pathways by ATR-FT-IR technique, the phenol hydroxylation was monitored at low temperature (40 °C) to retard the reaction rate. The reactant mixture with phenol/H₂O₂ of 1/1 was used for comparison with results from the batch reaction. The progress of the reaction is

showed in Figure 6.10 A) resulting in the formation of broad band with the center at 1640 cm^{-1} . It increased with the reaction time however the CO_2 peak at 2340 cm^{-1} could not be observed. When the reaction temperature was increased to $70\text{ }^\circ\text{C}$, the broad band at $1610 - 1640\text{ cm}^{-1}$ was observed and increased with the time. CO_2 peak was observed with less intensity at 2340 cm^{-1} . There was not much CO_2 peak from deep oxidation within the reaction of 120 min. Not only the reaction temperature but also amount of H_2O_2 affected to the deep oxidation during the phenol hydroxylation giving CO_2 .

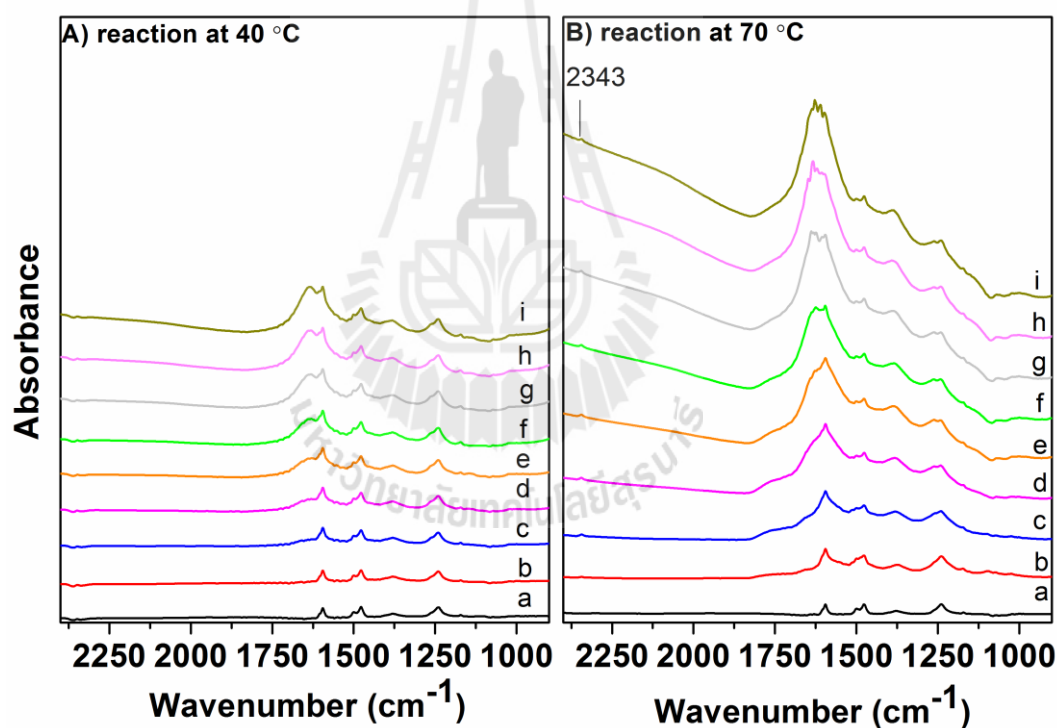


Figure 6.10 Phenol hydroxylation on $\text{Fe}/\text{NH}_4\text{MCM-22-LSIE}$ with the phenol/ H_2O_2 molar ratio of 1/1 under flowing condition at the reaction temperature of A) $40\text{ }^\circ\text{C}$ B) $70\text{ }^\circ\text{C}$ at the reaction time a) 0, b) 15, c) 30, d) 45, e) 60, f) 75 and g) 90 h) 105 and i) 120 min.

In conclusion, the suitable reaction condition for phenol hydroxylation by ATR-FT-IR technique was determined depended on the resolution of IR spectra. Fe/NH₄MCM-22-LSIE was used as a model catalyst for finding the reaction condition. The optimum condition was carried out on flowing reactor. Catalyst was coated on ZnSe crystal with 40.0 mg. The reactant mixture with the phenol/H₂O₂ molar ratio of 1/1 was flowed onto the catalyst coated-ZnSe with the flow rate of 0.05 mL/min. The IR spectra were recorded with the reaction time.

6.4.5 The phenol hydroxylation by ATR-FT-IR technique over Fe supported catalyst on zeolite MCM-22

Supported Fe catalysts prepared from 3 methods were tested for phenol hydroxylation with the reaction condition getting from the previous results. The IR spectra of supported Fe catalysts are show as Figure 6.11. They had the similar features for all catalysts. The broad band with the centre at 1640 cm⁻¹ increased with the reaction time. The CO₂ peak at 2341 cm⁻¹ was not clearly observed owing to low amount of H₂O₂.

Abbas and co-workers (2008) measured the ATR-FT-IR spectra of various organic acids. The broad band's presented at 1610-1643 cm⁻¹ and 1710-1729 cm⁻¹ were assigned to O-C=O and C=O of organic acid, respectively etc. Thus the presence of broad band observed at 1640 cm⁻¹ in this work could indicate the formation of organic acids. The presence of CO₂ could confirm the deep oxidation of phenol. The pathway of phenol hydroxylation has been proposed from the work in other groups. Zazo and co-workers (2005) studied the phenol hydroxylation by Fenton's reagent in a batch reactor at 25 °C. To elucidate the reaction pathway, a series of runs were carried out using phenol, CAT, HQ, BQ and organic acids as starting compounds for

the oxidation by H_2O_2 . The proposed pathway is shown as Scheme 6.1. CO_2 was observed as a final product obtained from the deep oxidation of reactants under the excess amount of H_2O_2 , fourteen times over concentration of phenol. This proposed scheme was similar to the works from Karakhanov et al. (2010) and Zhou et al. (2011).



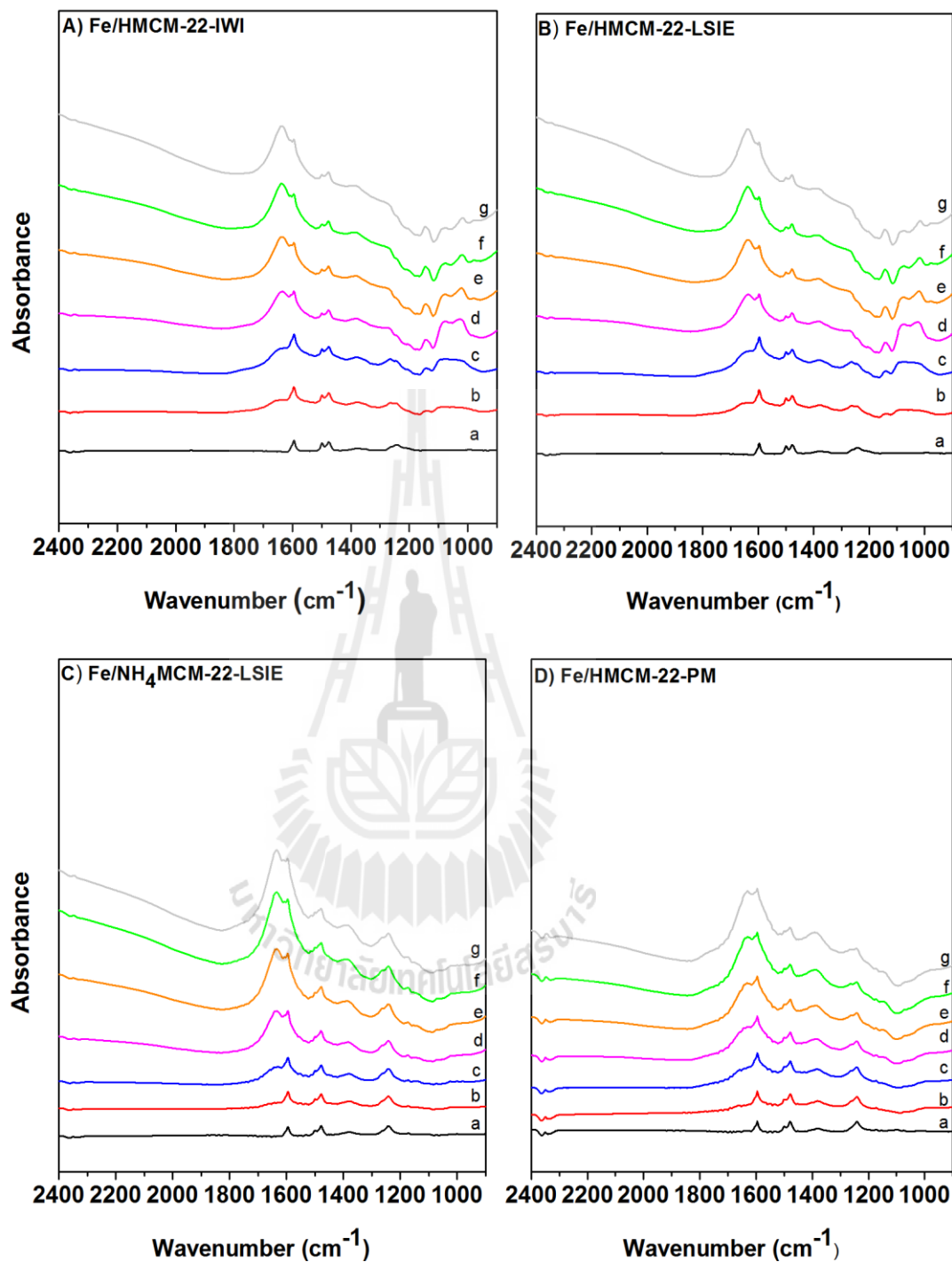
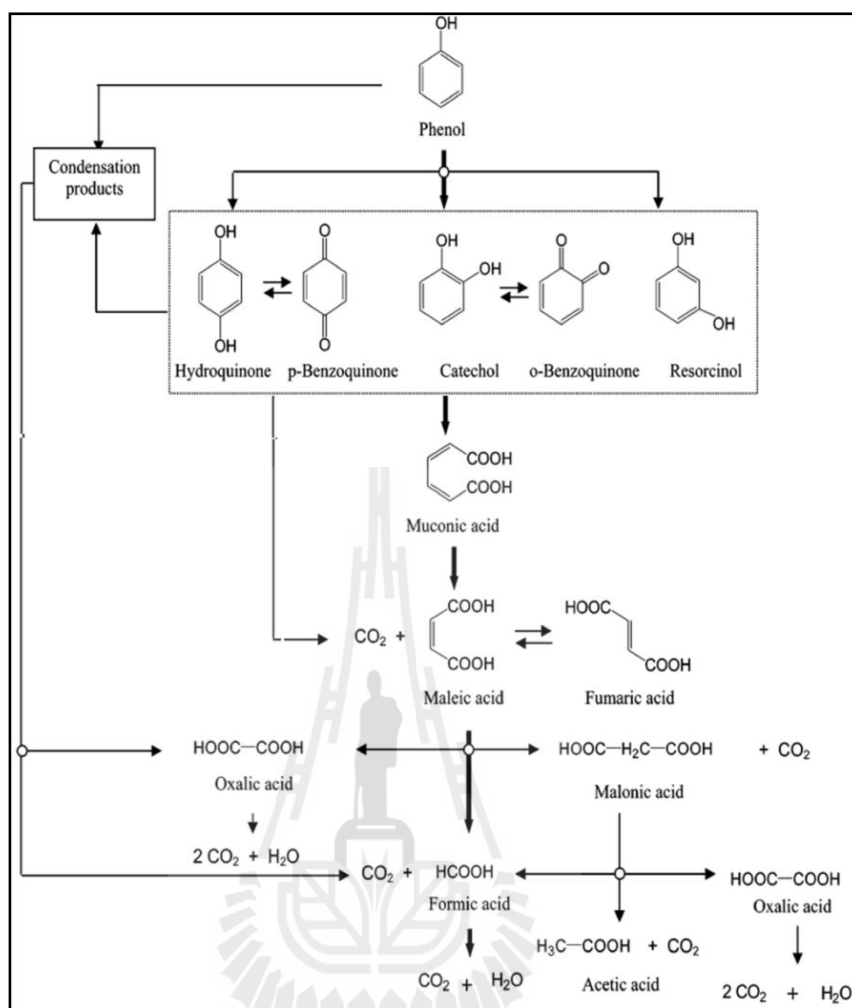


Figure 6.11 Phenol hydroxylation under flowing condition at the reaction temperature of 40 °C on Fe supported catalyst at the reaction time in minute: a) 0, b) 30, c) 60, d) 120, e) 180, f) 240 and g) 300 min.



Scheme 6.1 Proposed phenol hydroxylation by Fenton's reagent by Zazo et al. (2005).

All results from ATR-FT-IR measurement exhibited that organic acids could be produced from the deep oxidation of phenol during the phenol hydroxylation. It was a competition reaction leading to mass loss. To confirm the formation of organic acids, the phenol hydroxylation in batch process needed to perform and further analyze by HPLC.

6.4.6 The oxidation of HQ, CAT and BQ by ATR-FT-IR technique over supported Fe catalyst on zeolite MCM-22

According to Scheme 6.1, the oxidation of reaction intermediates (HQ, CAT and BQ) from phenol hydroxylation produced the organic acids. However, the complete oxidation produced CO₂ and H₂O as the final products. In this work, it was interesting to study the oxidation of HQ, CAT and BQ by using the H₂O₂ as oxidant. The progress of reaction was monitored by ATR-FT-IR. Figure 6.12 reveals the oxidation of HQ, CAT and BQ by H₂O₂, respectively. As the results, the peaks of CO₂ and organic acids were observed at around 2344 and 1751 cm⁻¹, respectively and increased with the reaction time. According to CO₂ peak, CAT and BQ were oxidized faster than HQ.

Zhou and co-workers (2011) proposed the pathway of phenol hydroxylation over CuNiAlCO₃ with H₂O₂ at 30 °C. The H₂O₂/phenol = 15 was carried out in the reaction. HQ was the primary product observed in the solution then it was oxidized to BQ. The BQ was continuously oxidized to maleic acid through a ring opening route and converted to formic and oxalic acid. Both acids could be further degraded to CO₂ (Zhou et al., 2011; Quintanilla-Catvajal et al., 2010). Therefore, there were many steps required for oxidation of HQ compared to CAT and BQ. In case of CAT, it could be oxidized directly to organic acid with the sequence shown in Scheme 6.1. For conclusion, CAT, HQ and BQ could be oxidized further to organic acids and CO₂ even the reaction was conducted under a mild reaction condition.

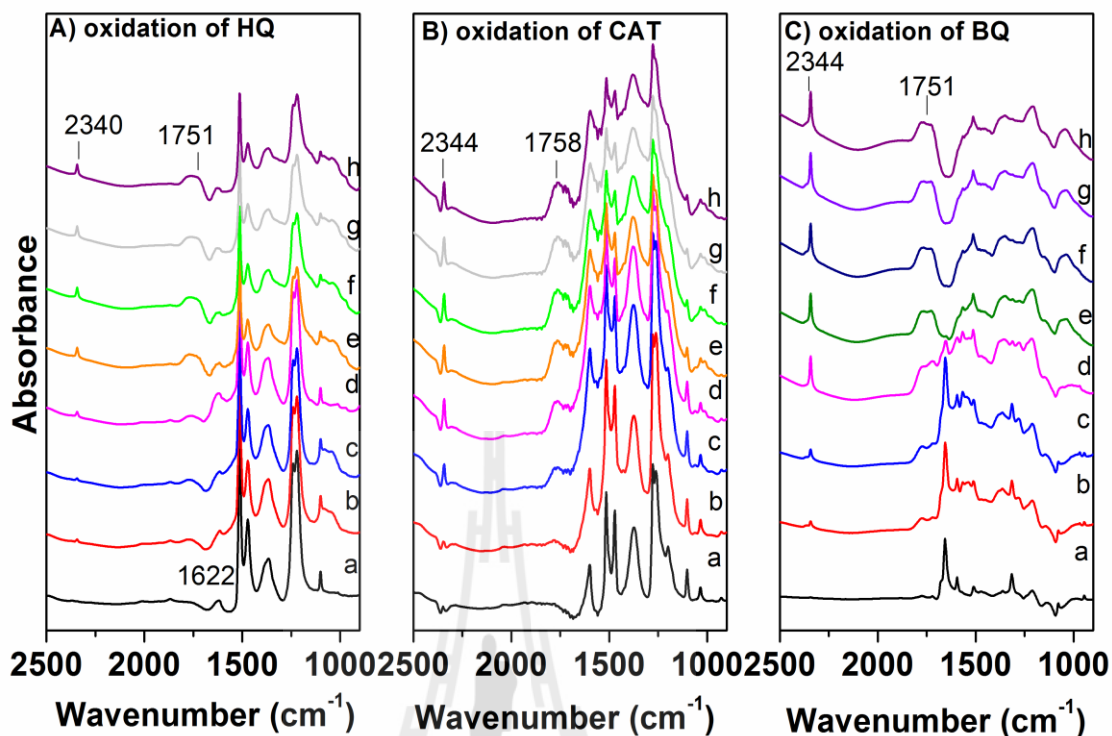


Figure 6.12 IR spectra for the oxidation of the reaction intermediates by H_2O_2 with the phenol/ H_2O_2 molar ratio of 1 at $40\text{ }^\circ\text{C}$ under flowing condition 0.1 mL/min using $\text{Fe}/\text{NH}_4\text{MCM-22}$ as catalyst A) HQ B) CAT and C) BQ at the reaction time in minute: a) 0, b) 30, c) 60, d) 120, e) 180, f) 240 and g) 300 min.

6.4.7 Change of solution pH after phenol hydroxylation in a batch reactor

To verify the formation of organic acids, the pH of solution during the phenol hydroxylation was measured. The reaction was performed in a batch reactor under the following condition; the phenol/ H_2O_2 molar ratio of 1/1 at $70\text{ }^\circ\text{C}$. $\text{Fe}/\text{HMCM-22-IWI}$ was used as a catalyst. Results obtained from the reaction are summarized in Table 6.2. The pH of solution decreased after the catalyst was added to the phenol aqueous solution. Then it became constant after stirred at $70\text{ }^\circ\text{C}$ for 30 min. afterward, the H_2O_2 was added to the solution. It was found that the pH of solution

decreased with the phenol conversion and became constant. The decrease of pH may be from either organic acid during the reaction or protons from the decomposition of H_2O_2 (Chen et al., 2005).

Table 6.2 Results of phenol hydroxylation and pH values of the reaction mixture.

Condition	Reaction time (min.)	% X_{phenol}	pH during the phenol hydroxylation in batch process
0.3332 M phenol (Room temperature)	0	-	6.77
0.3332 M phenol + catalyst (Room temperature)	0	-	6.29
0.3332 M phenol + catalyst (70 °C, stirred for 30 min.)	0	-	5.60
0.3332 M phenol + catalyst+ H_2O_2 (70 °C, stirred for 30 min.)	0	-	4.60
Phenol hydroxylation	10	11	4.07
	15	11	3.92
	30	28	3.44
	60	55	1.47
	90	54	1.44
	120	55	1.45
	180	55	1.44

6.4.8 Phenol hydroxylation analyzed by HPLC over Fe/HMCM-22-IWI on zeolite MCM-22

According to ATR-FT-IT results, all catalysts revealed the similar feature of the IR spectra. Thus, the catalyst with the lowest reaction rate was considerably monitored by HPLC. The reaction was performed in a batch reactor by using Fe/HMCM-22-IWI as a catalyst. The reaction mixture was analyzed by HPLC technique. Figure 6.12 shows the chromatogram of standards used for the analysis. The peak position is concluded in Table 6.1. For organic acids standard, it was a

mixture aqueous solution of oxalic acid, acetic acid and formic acid. For aromatic hydrocarbon standard, it was a mixture aqueous solution of CAT, HQ, BQ, resorcinol and phenol.

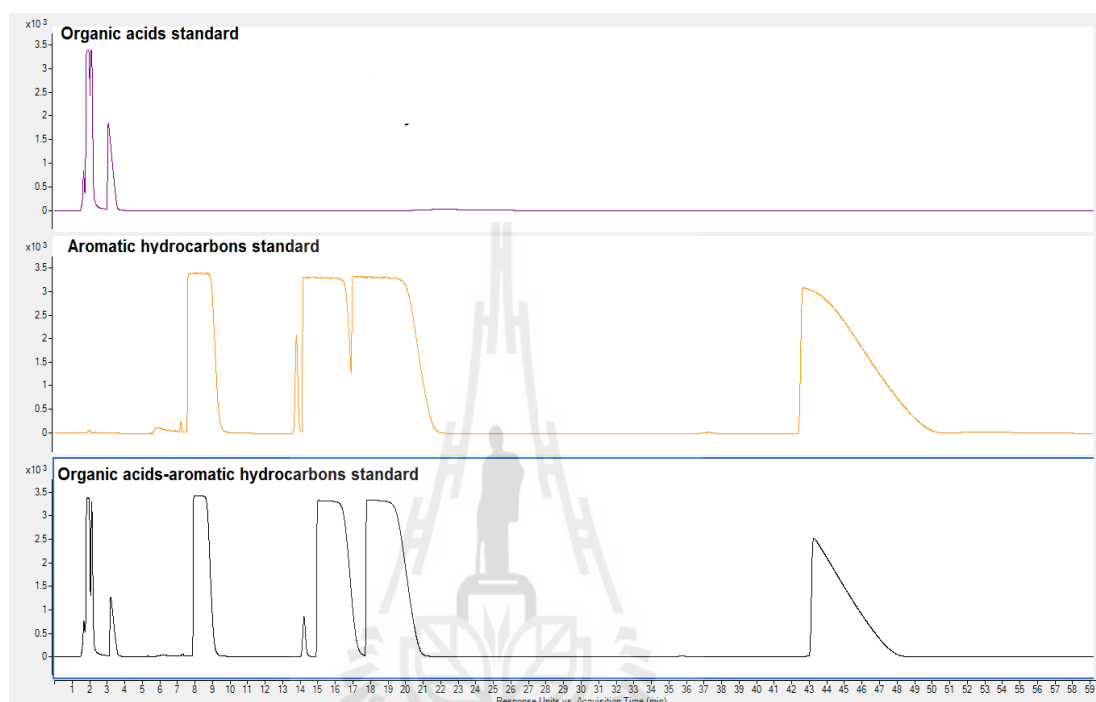


Figure 6.13 Chromatograms of standards for phenol hydroxylation.

Table 6.3 Retention time of standards for phenol hydroxylation from chromatograms.

Compounds	Retention time (min)
Organic acids standard (oxalic acid, acetic acid and formic acid)	1.5 - 4.0
Aromatic hydrocarbons standard (Phenol, CAT, HQ, BQ and resorcinol)	8, 13.8, 15, 19 and 43

Figure 6.14 shows the chromatogram of reaction mixture withdrawn at different reaction times. At 20 min the reaction occurred resulting in the formation of HQ, CAT and small amount of BQ. The phenol peak was still observed as a broad

peak. A series of aromatic hydrocarbon peaks were presented with the blue line. Moreover, the peaks stand for organic acids could be observed and presented with the red line. Thus, the deep oxidation of phenol to organic acids was occurred as a side reaction during the phenol hydroxylation. However, the organic acids decreased with the reaction time and no longer observed at 60 min. During the decrease of organic acids, new peaks were observed at the retention time of 4 - 8 min probably from the decomposition of organic acid which could not be identified.

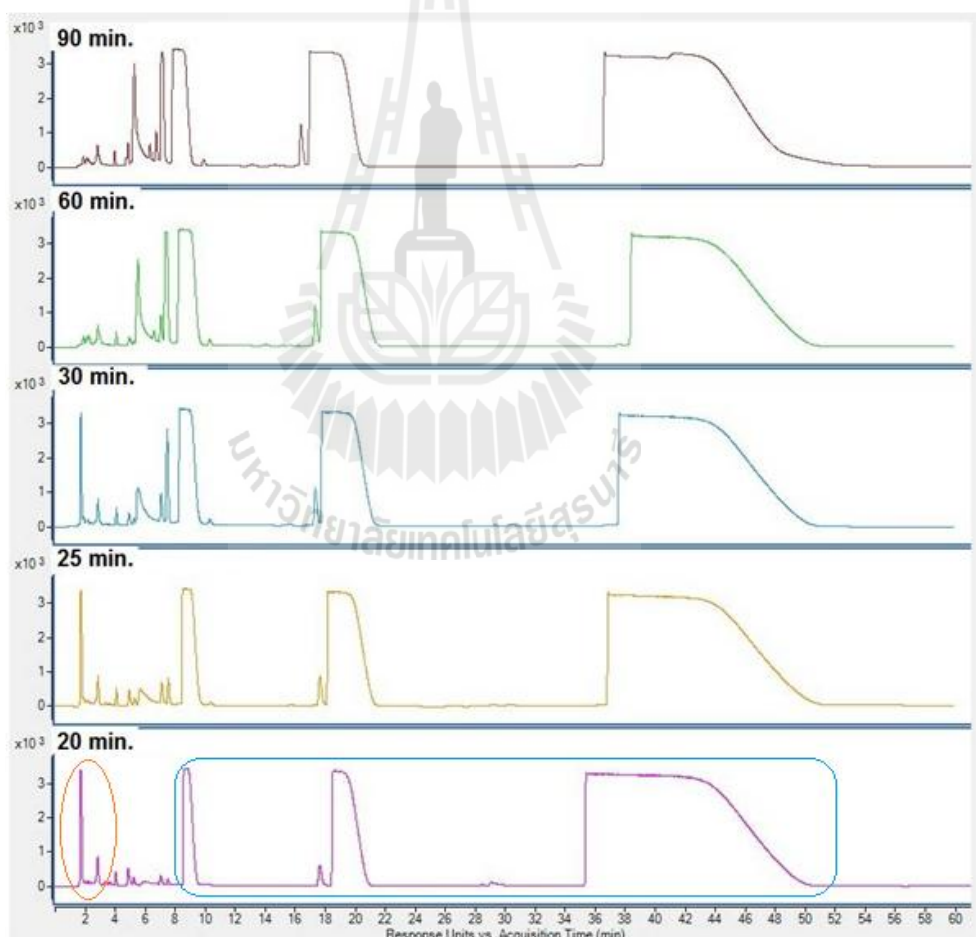


Figure 6.14 chromatogram of reaction mixture from phenol hydroxylation in a batch reactor at different reaction times.

6.5 Conclusions

Phenol hydroxylation was carried on supported Fe catalysts prepared by 3 methods. According to results from GC, CAT and HQ were observed as major products. BQ was observed as a kinetic product. However mass loss during the reaction was observed and defined as “others”. Regarding to the ATR-FT-IR measurement, CAT, HQ and BQ could be oxidized further to yield organic acids and CO₂. The formation of organic acids was verified by HPLC. In conclusion, the deep oxidation was a side reaction. It was one of the reasons that caused the mass loss in phenol hydroxylation.

6.6 References

- Abbas, O., Rebufa, C., Dupuy, N. and Kister, J. (2008). FTIR-Multivariate curve resolution monitoring of photo-Fenton degradation of phenolic aqueous solutions Comparison with HPLC as a reference method. **Talanta**. 77: 200-209.
- Alnaizy, R. and Akgerman, A. (2000). Advanced oxidation of phenolic compounds. **Advances in Environmental Research**. 4: 233-244.
- Andanson, J-M. and Baiker, A. (2010). Exploring catalytic solid/liquid interfaces by in situ attenuated total reflection infrared spectroscopy. **Chemical Society Reviews**. 39: 4571-4584.
- Burgi, T. (2006). Attenuated Total Reflection Infrared Spectroscopy of Solid Catalysts Functioning in the Presence of Liquid-Phase Reactants. **Advances in Catalysis**. 50: 227-283.

- Chen, C., Xu, C., Feng, L., Suo, J. and Qiu, F. (2005). Kinetics and reaction mechanism of phenol hydroxylation catalyzed by La-Cu₄FeAlCO₃. **Science in China Series B: Chemistry**. 48: 530–537.
- Choi, J.-S., Yoon, S.-S., Jang, S.-H. and Ahn, W.-S. (2006). Phenol hydroxylation using Fe-MCM-41 catalysts. **Catalysis Today**. 111: 280-287.
- Corma, A., Corell, C. and Pérez-Pariente. (1995). Synthesis and characterization of MCM-22 zeolite. **Zeolites**. 15: 2-8.
- Jung, Y. M. (2003). Characterization of Ph-dependent IR spectra of oxalic acid: comparison of self-modeling curve resolution analysis with calculation of IR frequencies. **Bulletin of Korean Chemical Society**. 24: 1410-1412.
- Karakhanov, E. A., Maximov, A. L., Kardasheva, Y. S., Skorkin, V. A., Kardashev, S. V., Ivanova, E. A., Lurie-Luke, E., Seeley, J. A. and Cron, S. L. (2010). Hydroxylation of phenol by hydrogen peroxide catalyzed by copper(II) and iron(III) complexes: the structure of the ligand and the selectivity of ortho-hydroxylation. **Industrial & Engineering Chemistry Research**. 49: 4607-4613.
- Quintanilla-Carvajal, M. X., Camacho-Diaz, B. H., Meraz-Torres, L. S., Chanona-Perez, J. J. and Jung, Y. M. (2003). Characterization of pH-dependent IR spectra of oxalic acid: comparison of self-modeling curve resolution analysis with calculations of IR frequencies. **Bulletin of the Korean Chemical Society**. 24: 1410-1412.
- Matthews, R. W. and McEvoy, S. R. (1992). Destruction of phenol in water with sun, sand and photocatalysis. **Solar Energy**. 49: 507-513.

- Merayo, N., Hermosilla, D., Negro, C. and Blanco, Á. (2013). On-line FTIR as a novel tool to monitor Fenton process behavior. **Chemical Engineering Journal**. 232: 519-526.
- Meyer, C., Clement, G. and Balaceanu, J. C. (1965). Initiation of a free radical chain reaction by heterogeneous catalysis in: **Proceedings of Third International Congress on Catalysis**, 1: 184.
- Okamoto, K., Yamamoto, Y., Tanaka, H., Tanaka, M. and Itaya, A. M. (1985) Kinetics of heterogeneous photocatalytic decomposition of phenol over anatase TiO₂ powder. **Bulletin of the Chemical Society of Japan**. 58: 2023-2028.
- Peres, J. A., Domínguez, J. R. and Beltran-Heredia, J. (2010). Reaction of phenolic acids with Fenton-generated hydroxyl radicals: Hammett correlation. **Desalination**. 252: 167-171.
- Xiong, C., Chen, Q., Lu, W., Gao, H., Lu, W. and Gao Z. (2000). Novel Fe-based complex oxide catalysts for hydroxylation of phenol. **Catalysis Letters**. 69: 231-236.
- Zazo, J. A., Casas, J. A., Mohedano, A. F., Gilarranz, M. A. and Rodríguez, J. J. (2005). Chemical pathway and kinetics of phenol hydroxylation by Fenton's reagent. **Environmental Science & Technology**. 39: 9295-9302.
- Zhou, S., Qian, Z., Sun, T., Xu, J. and Xia, C. (2011). Catalytic wet oxidation of phenol over Cu-Ni-Al hydrotalcite. **Applied Clay Science**. 53: 627-633.

CHAPTER VII

GOLD/PALLADIUM BIMETALLIC ALLOY

NANOCLUSTERS STABILIZED BY CHITOSAN AS

HIGHLY EFFICIENT AND SELECTIVE CATALYST

FOR HOMOCOUPLING OF ARYLBORONIC ACID

7.1 Abstract

Aerobic oxidative homocoupling of arylboronic acid under acidic aqueous conditions (pH 4.0) using bimetallic Au/Pd alloy nanoclusters stabilized by chitosan have been investigated. It was found that Au_{0.81}Pd_{0.19} catalyst (3.1 ± 0.8 nm) exhibited superior catalytic activities as compare to monometallic Au (2.3 ± 0.3 nm) and other series of bimetallic nanoclusters, giving the corresponding biaryls nearly in quantitative yield.

7.2 Introduction

Bimetallic Au/Pd alloy nanoclusters have been of particular importance in the field of catalysis since they often exhibit better catalytic properties than the corresponding monometallic counterparts (Ferrando et al., 2008; Toshima et al., 1998; Hutchings, 2008; Chen et al., 2005; Yudha et al., 2011; Kesavan et al., 2011 and Zhang et al., 2012). The catalytic activity of bimetallic nanoclusters markedly depended on the compositions of surface atoms and hence, the activity could be tuned

by changing the ratios of constituent metal atoms, accordingly (Zhang et al., 2011; Villa et al., 2007 and Venezia et al., 2003). The use of hydrophilic polymer matrix as stabilizer not only made the homogeneity in aqueous solution but also offered unique possibilities for enhancing the access of reactants to the catalytic sites (Tsukuda et al., 2011). Previously we reported that gold nanoclusters stabilized by poly (1-vinylpyrrolidin-2-one) (PVP) were highly active catalysts for homocoupling of arylboronic acid under basic aqueous conditions (Tsunoyama et al., 2004), the first example of the gold nanocluster-catalyzed carbon–carbon bond formation (Carrettin et al., 2005; Carrettin et al., 2005; Willis and Guzman, 2008; Chaicharoenwimolkul et al., 2008 and González et al., 2006). However, oxygenation reaction to phenol derivatives was unavoidable due to the formation of hydrogen peroxide equivalent during the homocoupling reactions under the basic conditions with PVP-stabilized gold nanoclusters (Au:PVP) as a catalyst (Tsunoyama et al., 2004 and Kuivila, 1954). To avoid the basic conditions for suppressing the oxygenation, the homocoupling of a potassium aryltrifluoroborate (ArBF_3K) salt catalyzed by Au:PVP under neutral conditions was achieved (Sakurai et al., 2007), however, direct use of arylboronic acid was highly desirable. Recently, we reported that gold clusters stabilized by polyhydroxy biopolymer including chitosan (β -1, 4-linked poly *D*-glucosamine) (Au:chit) and starch (Au:starch) showed superior catalytic activity towards the oxidative homocoupling with high selectivity in aqueous acidic media (Dhital et al., 2012). The high activity of Au:chit was driven from the unique matrix effect where chitosan played the dual function, i.e. stabilization of cluster as well as activation of substrate and high selectivity was due to the acidic media of reaction.

We intended to develop a highly sustainable and selective catalyst for oxidative homocoupling of arylboronic acid and thus, we started to investigate the effect of series of bimetallic Au/Pd alloy catalyst stabilized by chitosan matrix. Herein, we reported the substantial effect of bimetallic Au/Pd alloy clusters in the acceleration of oxidative homocoupling as well as the suppression of the oxygenation side-pathway.

7.3 Experiment

7.3.1 Chemicals

Hydrogen tetrachloroaurate tetrahydrate (Tanaka Kikinzoku), palladium chloride (Wako) sodium tetraborohydride (Wako), acetic acid (Wako), chitosan with a medium molecular weight of 75 - 85% de-acetylated (Sigma Aldrich), phenylboronic acid, 4-methoxyphenylboronic acid, 4-methylphenylboronic acid, 4-fluorophenylboronic acid, 4-chlorophenylboronic acid, 4-cyanophenylboronic acid (Sigma Aldrich) were commercially purchased and further purified according to the standard methods, if necessary. In particular, all arylboronic acids were purified by recrystallization from H₂O before use. Milli-Q grade water was used in all experiments. Au:chit was prepared according to our previous report (Dhital et al., 2012).

7.3.2 Preparation of Au/Pd:chit

The series of bimetallic Au/Pd nanoclusters were prepared using an organic synthesizer (EYELA, PPS-2510). Chitosan (150 mg) was placed in a hard glass test tube ($\varnothing = 45$ mm) and dispersed into 46.5 mL of 0.18% of aqueous acetic acid solution in MilliQ water. To the solution, quantitative amount of stock 25 mM HAuCl₄ and 12.5 mM PdCl₂, were added and final solution was made 0.5 mM of total

metals concentration. The resulting solution was stirred for 30 minutes (1600 rpm) at room temperature and maintained 6 °C before reduction and then, an aqueous solution of NaBH₄ (2.5 mL of 9.7 mg, 0.1 M) was rapidly added under 1600 rpm. The color of the solution immediately turned from pale yellow to dark brown, indicating the formation of small Au/Pd nanoclusters. The hydrosol of Au/Pd nanoclusters (0.5 mM) was stored in refrigerator at 5 °C and used for catalytic reactions.

7.3.3 Characterization of Au/Pd:chit

UV-Vis spectra were measured by JASCO V-670 spectrophotometer at 24 °C. The ratios of Au and Pd in bimetallic catalyst were analyzed by ICP-AES (LEEMANLABS INC, Profile plus). High-resolution TEM images were recorded with a JEM-2100F at an accelerating voltage of 200 kV. GC 2010 (Shimadzu) with Rtx-5MS column (length 30 m, inner diameter 0.25 mm and film thickness 0.25 µm) was used for monitoring the kinetics of reactions. ¹H NMR spectra were measured on a JEOL JMN LAMBDA 400 spectrometer at 23 °C at 400 MHz. CDCl₃ was used as a solvent and the residual solvent peak was used as an internal standard (7.26 ppm). TLC analysis was performed using Merck Silica gel 60 F₂₅₄ and preparative TLC was conducted using Wako Wakogel B-5F. Horiba pH/DO meter, D-55 was used to measure the pH of the solutions.

7.3.4 Procedure for the homocoupling of arylboronic acid (1) by Au/Pd:chit

All the reaction was carried out using an organic synthesizer EYELA PPS-2510. A test tube (Ø = 30 mm) was placed with 0.25 mmol of **1** and 5 mL of pH = 4 acetate buffer at 30 °C. To the mixture was added 10 mL of 0.5 mM Au/Pd:chit solution (2 atom%) and the mixture was stirred vigorously (1300 rpm) for the required time listed in Table 6.2. The reaction was quenched with ethyl acetate and the

products were extracted with ethyl acetate (4 x 15 mL). The combined organic layer was washed with brine, dried over Na_2SO_4 and evaporated in vacuum. The crude product was purified by PTLC to afford pure **2**. The yield of **3** was determined by ^1H -NMR using dioxane as internal standard.

7.4 Results and discussion

7.4.1 Characterization of Au/Pd:chit

A series of Au/Pd:chit with different metal ratios were prepared according to our previous method by co-reduction method using sodium borohydride as a reducing agent and chitosan as a stabilizing agent (Murugadoss and Sakurai, 2011). HAuCl_4 and H_2PdCl_4 solution were used as each metal source. The initial metal content in mM can be found in Appendix D. The ratio of these two metals were calculated from the initial mole ratio of the mixing solutions and finally determined by ICP-AES analysis. As shown in Table 7.1, the calculated initial ratios were in accordance with that determined by ICP-AES. The Au-enriched alloys consisting of more than 70% Au were successfully prepared and they were stable enough to be stored as a hydrosol in refrigerator for months without aggregation.

Table 7.1 Calculated and actual Au and Pd fraction, mean cluster size, rate constant (k) and rate constant by surface area (k').

Catalyst	Fraction of calculated concentration		Fraction of actual metal analyzed by ICP-AES		Mean cluster size from TEM (nm)	k (h^{-1})	k' (au)
	Au	Pd	Au	Pd			
Au:chit	1.00	-	1.00 ± 0.07	-	2.3 ± 0.2	$(2.1 \pm 0.1) \times 10^{-1}$	1.0 ± 0.1
Au _{0.91} Pd _{0.09} :chit	0.90	0.10	0.91 ± 0.04	0.09 ± 0.04	2.6 ± 0.3	$(4.2 \pm 0.2) \times 10^{-1}$	2.3 ± 0.2
Au _{0.86} Pd _{0.14} :chit	0.85	0.15	0.86 ± 0.03	0.14 ± 0.06	2.8 ± 0.3	$(6.3 \pm 0.1) \times 10^{-1}$	3.7 ± 0.2
Au _{0.81} Pd _{0.19} :chit	0.80	0.20	0.81 ± 0.02	0.19 ± 0.06	3.1 ± 0.8	$(11.0 \pm 0.4) \times 10^{-1}$	7.1 ± 0.3
Au _{0.77} Pd _{0.23} :chit	0.75	0.25	0.77 ± 0.05	0.23 ± 0.02	3.3 ± 0.7	$(6.1 \pm 0.2) \times 10^{-1}$	4.2 ± 0.2
Au _{0.72} Pd _{0.28} :chit	0.70	0.39	0.72 ± 0.03	0.28 ± 0.01	4.5 ± 1.4	$(4.1 \pm 0.1) \times 10^{-1}$	3.9 ± 0.3



UV-Vis spectra of series of Au/Pd:chit are shown in Figure 7.1A) and B). An exponentially increasing absorbance was observed towards higher energy due to inter band transition of newly formed bimetallic alloyed structure. The gradual disappearance of surface plasmon band (SPR) of Au:chit on bimetalization with Pd also indicated the formation of alloy rather than segregation of Pd (Scott et al., 2004; Toshima et al., 1992; Creighton and Eadon, 1991).

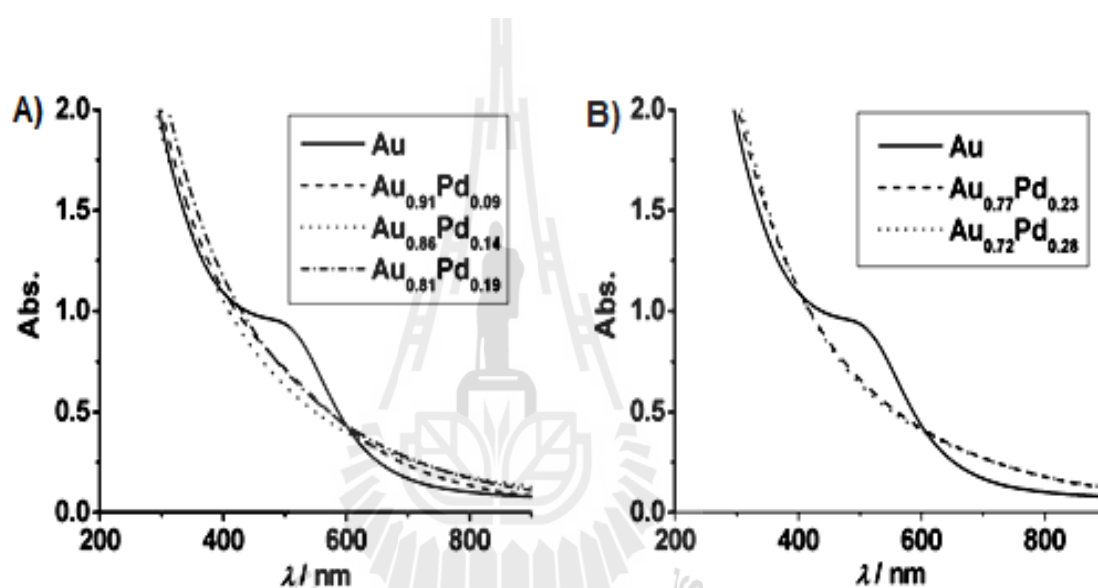


Figure 7.1 UV-Vis absorption spectra of A) $\text{Au}_{0.91}\text{Pd}_{0.09}$:chit, $\text{Au}_{0.86}\text{Pd}_{0.14}$:chit, $\text{Au}_{0.81}\text{Pd}_{0.19}$:chit in reference with Au:chit, B) $\text{Au}_{0.77}\text{Pd}_{0.23}$:chit and $\text{Au}_{0.72}\text{Pd}_{0.28}$:chit in reference with Au:chit.

Representative transmission electron microscopy (TEM) images of series of bimetallic nanoparticles (Figure 7.2) with different metallic ratios showed that particle sizes were increased with increasing the Pd content in bimetallic clusters. For example, the average size of Au:chit was estimated to be 2.3 ± 0.2 nm and on bi-

metallization with Pd, mean size was gradually increased up to 4.5 ± 1.4 nm. The results are also summarized in Table 7.1.

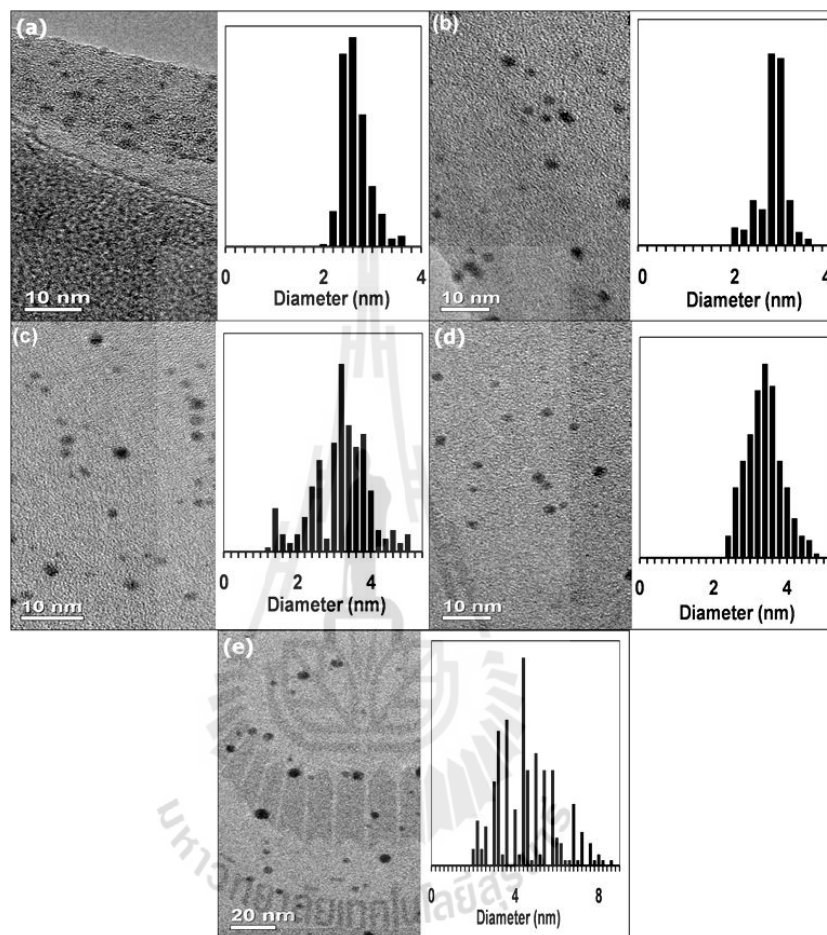


Figure 7.2 Transmission electron microscopy images of (a) $\text{Au}_{0.91}\text{Pd}_{0.09}:\text{chit}$ (b) $\text{Au}_{0.86}\text{Pd}_{0.14}:\text{chit}$ (c) $\text{Au}_{0.81}\text{Pd}_{0.19}:\text{chit}$ (d) $\text{Au}_{0.77}\text{Pd}_{0.23}:\text{chit}$ (e) $\text{Au}_{0.72}\text{Pd}_{0.28}:\text{chit}$.

In contrast, to Au-enriched clusters, the alloys having less than 60% of Au such as $\text{Au}_{0.6}\text{Pd}_{0.4}:\text{chit}$ or $\text{Au}_{0.5}\text{Pd}_{0.5}:\text{chit}$ became unstable and suffered from the aerobic oxidation to form charged Pd species. Figure 7.3 shows the UV-Vis spectra of $\text{Au}_{0.6}\text{Pd}_{0.4}:\text{chit}$ and $\text{Au}_{0.5}\text{Pd}_{0.5}:\text{chit}$ as freshly prepared and after one day, indicating the

rapid formation of charged Pd species. Therefore, the alloy clusters with more than 70% Au were used in the following catalyst investigation.

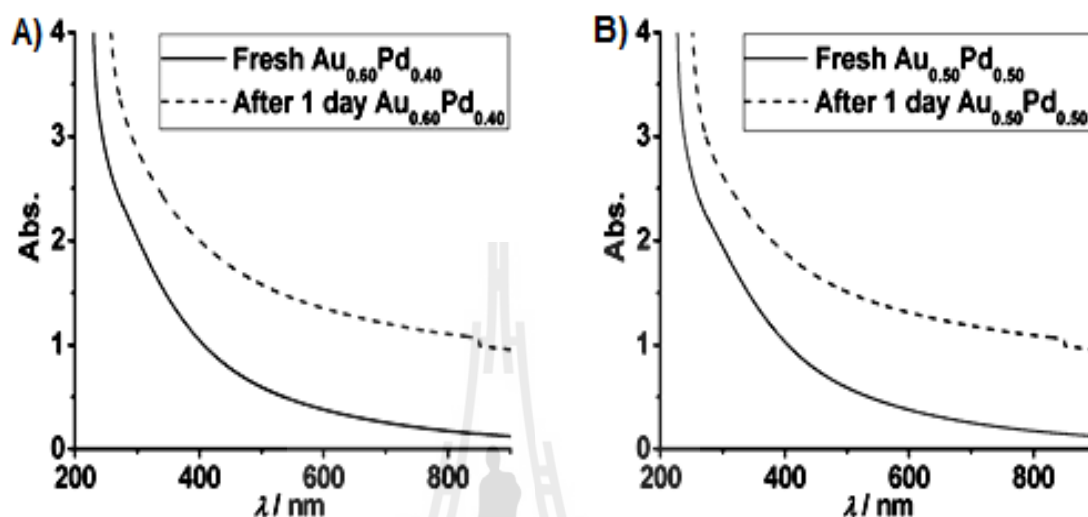


Figure 7.3 UV-Vis absorption spectra of (a) Au_{0.60}Pd_{0.40}:chit, freshly prepared and after one day, (b) Au_{0.50}Pd_{0.50}:chit, freshly prepared and after one day.

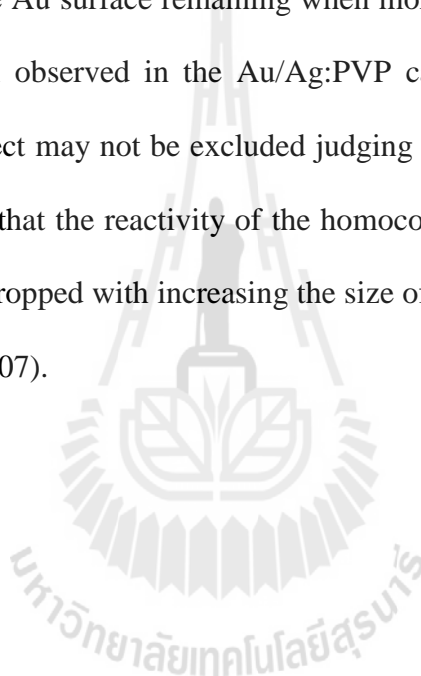
7.4.2 Catalytic performance of Au/Pd:chit in homocoupling of phenylboronic acid

First, the catalytic activity of the thus-prepared bimetallic Au/Pd catalysts were screened by homocoupling of phenylboronic acid (**1a**) in the presence of 2 atom% catalysts in acetate buffer solution (pH = 4) under air at 30 °C. Among these catalysts, in particular, Au_{0.81}Pd_{0.19}:chit exhibited superior activity to accomplish the reaction within 4 h, giving **2a** almost quantitatively with a trace amount of phenol (**3a**), detected by GC. Since all the reaction followed pseudo-first order against the decay of the concentration of **1a**, the rate constants (*k*) of each catalyst were obtained from the least-square fit. Details of kinetic plot are demonstrated in Appendix E. In

order to evaluate the rate constant quantitatively against the total exposed surface areas for each catalyst under the conditions in which total number of Au and Pd atoms was conserved, the rate constant per unit surface area relative to that of Au:chit, k'_n , was obtained by assuming a spherical shape given by the following equation [$k'_n = (d_n/2.3) \times (k_n/k_{100})$](d_n : the core diameters). Both k and k' are listed in Table 7.1. To clarify the bimetallic effect, the relationships between relative rate constants (k'_n) and the Pd contents in the alloy (Figure 7.4A) and the mean size of the clusters (Figure 7.4 B) are shown, respectively. It was found that there was an optimum alloy ratio for the best catalyst, i.e. the rate of conversion of **1a** increased with the Pd content when it was from 5% to 19% but decreased with Pd content more than 19%.

The following discussion was constituted on the assumption that the homocoupling reaction was promoted on Au (not on Pd) because in general, Au clusters promoted the homocoupling more efficiently than Pd clusters. For example, Au:PVP had higher activity towards homocoupling of arylboronic acid as compare to Pd:PVP (Dhital and Sakurai, 2012), although direct comparison using chitosan matrix could not be operated due to the unavailability of the pure Pd:chit. Effect of electronic structures of Au:PVP on aerobic oxidation catalysis had been studied. It was concluded that the catalytic activity was enhanced with increasing electron density on the Au core because the electron transfer from the anionic Au core to the LUMO of O₂ led to the formation of superoxo or peroxy-like species, an active site in the aerobic oxidation reactions (Tsunoyama et al., 2009). We also reported that chitosan matrix worked as an electron donor to the Au core, therefore similar effect of electronic structure in chitosan to that in PVP matrix was expected (Tsunoyama et al., 2011). In addition, electron donation effect from the Ag of its optimum of 10%

containing bimetallic Au/Ag alloy cluster enhanced oxidation reaction had already been reported (Chaki et al., 2007). Since Pauling's electronegativity of gold (2.54) is larger than that of Pd (2.24), the interaction between two metals will allow Au to accept electrons from Pd, leading to the increase of catalytic activity with increasing the Pd contents up to 19%. Two reasons might be considered why Au/Pd alloy nanoclusters having more than 20% of Pd are less active. One may be attributed to the decrease of the active Au surface remaining when more Pd was doped in the clusters, which had also been observed in the Au/Ag:PVP catalyst (Chaki et al., 2007). In addition, the size effect may not be excluded judging from the result in Figure 7.4B). We already reported that the reactivity of the homocoupling of ArBF_3K catalyzed by Au:PVP drastically dropped with increasing the size of Au clusters from 1.3 nm to 9.5 nm (Sakurai et al., 2007).



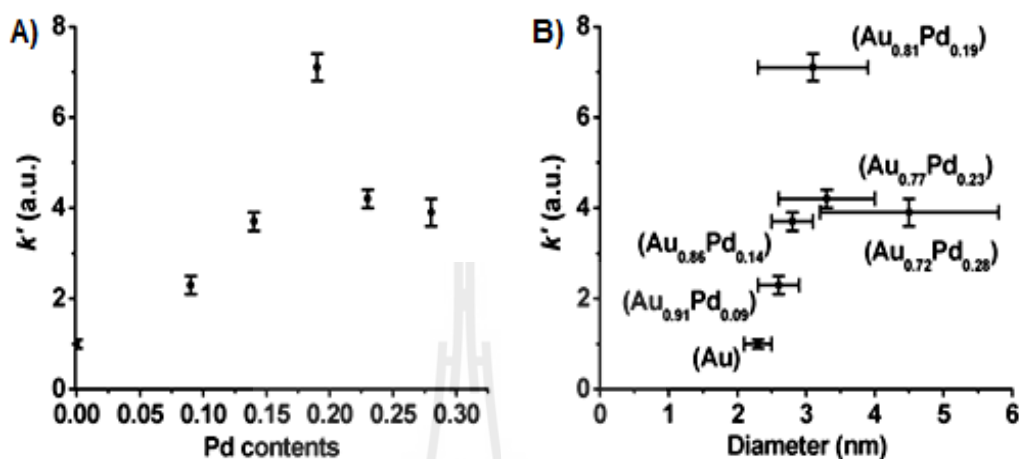


Figure 7.4 The relationship between reaction rates of oxidative homocoupling of phenylboronic acid (**1a**) by a series of bimetallic Au/Pd nanoparticles.

Next, the relative rates of oxidative coupling of *para*-substituted arylboronic acids using Au_{0.81}Pd_{0.19}:chit as a catalyst were examined and the results are listed in Table 7.2. All the reaction was performed using 0.25 mmol of arylboronic acid in the presence of 2 atom% of Au_{0.81}Pd_{0.19}:chit in acidic aqueous solution (pH 4, acetate buffer) under air at 30 °C. In the case of R = OMe (**1b**), a strongly electron-donating group, the reaction was completed within 2.5 hours and gave 98% of 4,4'-dimethoxybiphenyl (**2b**) with less than 1% of 4-methoxyphenol (**3b**) (entry 2). The reaction of 4-tolylboronic acid (**1c**) was much faster than that of **1a** or **1c** and was completed within 1.5 hours, giving 4,4'-dimethylbiphenyl (**2c**) almost quantitatively with a trace amount of 4-cresol (**3c**) (entry 3). The halogen substituents such as 4-fluorophenylboronic acid (**1d**) and 4-chlorophenylboronic acid (**1e**) also afforded the

corresponding biaryls (**2d**, **2e**) in 97% and 96% yields, respectively (entries 4 and 5). It should be noted that **1d** and **1e** showed significant differences in the reaction rate. The reaction of **1d** took 10 hours to complete, whereas 34 hours was required for **1e** and as a result, significant amount of oxygenated by-product (**3e**) was detected in 3% yield. In the case of 4-cyano derivative (**1f**), a strongly electron withdrawing group, the reaction was somewhat faster than that of **1e** to afford **2f** and **3f** in 96% and 2% yields, respectively after 12 hours.

Table 7.2 Oxidative homocoupling of various *para*-substituted arylboronic acids catalyzed by Au_{0.81}Pd_{0.19}:chit.

Entry	R	σ	σ^-	lnk (h ⁻¹)	Time (h)	Yield (%)	
						2 ^[a]	3 ^[b]
1	H (1a)	0.00	0.00	0.13	3	98 (2a)	<1 (3a)
2	OMe (1b)	-0.27	-0.26	0.53	2.5	99 (2b)	<1 (3b)
3	Me (1c)	-0.17	-0.17	0.09	2	99 (2c)	<1 (3c)
4	F (1d)	0.06	-0.03	-0.84	10	97 (2d)	<1 (3d)
5	Cl (1e)	0.23	0.19	-2.81	34	96 (2e)	3 (3e)
6	CN (1f)	0.66	1.00	-1.99	12	96 (2f)	2 (3f)

Isolated yield^[a]. Estimated from NMR^[b]. The σ and σ^- were obtained from the publication of Hansch, C., Leo, A., Taft, R. W. (1991).

In our previous study of Au:chit catalyst, nucleophilicity of substrate had significant effect in the coupling reaction and reasonably linear relationship between the lnk/(h⁻¹) values and the Hammett σ^- substituent constants was obtained ($\rho = -1.62$);

this relationship suggested that the reaction proceeded via an anionic species $[\text{ArB}(\text{OH})_3^-]$ even though it was performed under acidic conditions (Dhital et al., 2012). We explained that the interfacial hydroxy groups between the hydrophobic part of the matrix and the water solvent played an important role in dragging the boronic acid into the interior part of the catalyst near the gold surface by through reversible binding with hydroxy group of chitosan. As a result, the reaction conditions inside the matrix resemble those in solution at pH 9 even under acidic conditions, thereby permitting the generation of boronate species. In this case, the reactivity was proportional to the nucleophilicity.

In contrast, neither Hammett plots using σ^- nor σ constants (Murugadoss et al., 2012) against the $\ln k/(h^{-1})$ values showed linear relationship in the $\text{Au}_{0.81}\text{Pd}_{0.19}$:chit-catalyzed reaction although the general trend was similar, i.e. the more nucleophilic substituents possess higher reactivity (Figure 7.5). In addition, the Hammett plot with σ substituent constants seems to fit slightly better than that with σ^- constants, indicating that the reaction likely proceeded via neutral species as a transition state. Such poor linear relationship suggested multiple reaction mechanisms or multiple catalytic sites involved in this catalytic reaction.

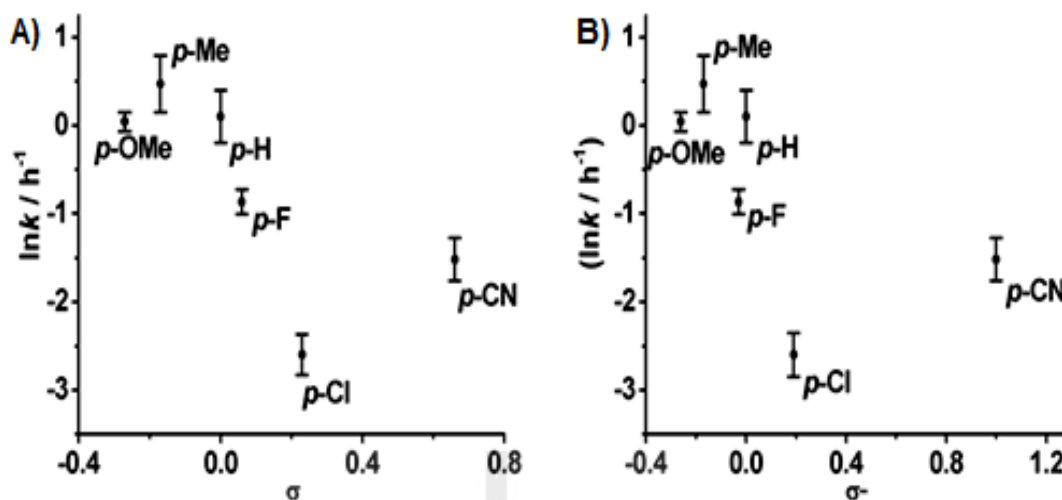


Figure 7.5 Hammett plot for homocoupling of substituted arylboronic acids; *p*-methyl phenylboronic acid, *p*-methoxyphenylboronic acid, phenylboronic acid, *p*-cyanophenylboronic acid, *p*-chlorophenylboronic acid and *p*-fluorophenylboronic acid.

7.5 Conclusion

As described above, we synthesized bimetallic Au/Pd alloy nanoclusters stabilized by chitosan with various Au/Pd ratios, which showed highly efficient and selective catalytic activity towards the oxidative homocoupling of arylboronic acid under ambient conditions in pH=4 acetate buffer solution. Among these catalysts, Au_{0.81}Pd_{0.19}: chit was the most active, particularly in comparison with monometallic Au:chit. The observed Hammett correlation indicated that the reaction is likely to occur by multiple mechanisms or multiple catalytic sites probably involved in bimetallic catalysis. Further investigation to elucidate the precise mechanism is in progress.

7.6 References

- Carrettin, S., Corma, A., Iglesias, M. and Sanchez, F. (2005). Stabilization of Au(III) on heterogeneous catalysts and their catalytic similarities with homogeneous Au(III) metal organic complexes. **Applied Catalysis A: General**. 291: 247-252.
- Carrettin, S., Guzman, J. and Corma, A. (2005). Supported Gold Catalyzes the homocoupling of phenylboronic acid with high conversion ands. **Angewandte Chemie International Edition**. 44: 2242-2245.
- Chaicharoenwimolkul, L., Munmai, A., Chairam, S., Tewasekson, U., Sapudom, S., Lakliang, Y. and Somsook, E. (2008). Effect of stabilizing ligands bearing ferrocene moieties on the gold nanoparticle-catalyzed reactions of arylboronic acids. **Tetrahedron Letters**. 49: 7299-7302.
- Chaki, N. K., Tsunoyama, H., Negishi, Y., Sakurai, H. and Tsukuda, T. (2007). Effect of Ag-doping on the catalytic activity of polymer-stabilized Au clusters in aerobic oxidation of alcohol. **Journal of Physical Chemistry C**. 111: 4885-4888.
- Chen, M., Kumar, D., Yi, C.-W. and Goodman, D. W. (2005). The Promotional Effect of Gold in Catalysis by Palladium-Gold. **Science**. 310: 291-293.
- Creighton, J. A. and Eadon, D. G. (1991) Ultraviolet–visible absorption spectra of the colloidal metallic elements Journal of the Chemical Society. **Faraday Transactions**. 87: 3881-3891.
- Dhital, R. N. and Sakurai, H. (2012) Anomalous efficacy of bimetallic Au/Pd nanoclusters in C-Cl bond activation and formal metathesis-type C-B bond activation at room temperature. **Chemistry Letters**. 41: 630-632.

- Dhital, R. N., Murugadoss, A. and Sakurai, H. (2012). Dual roles of polyhydroxy matrices in the homocoupling of arylboronic acids catalyzed by gold nanoclusters under acidic conditions. **Chemistry – An Asian Journal**. 7: 55-59.
- Ferrando, R., Jellinek, J. and Johnston, R. L. (2008). Nanoalloys: from theory to applications of alloy clusters and nanoparticles. **Chemical Reviews**. 108: 845-910.
- González-Arellano, C., Corma, A., Iglesias, M. and Sánchez, F. (2006). Gold (I) and (III) catalyze Suzuki cross-coupling and homocoupling, respectively. **Journal of Catalysis**. 238: 497-501.
- Hansch, C., Leo, A. and Taft, R. W. (1991). A survey of Hammett substituent constants and resonance and field parameters. **Chemical Reviews**. 91: 165-95.
- Hutchings, G. J. (2011). Solvent-free oxidation of primary carbon-hydrogen bonds in toluene using Au-Pd alloy nanoparticles. **Science**. 331: 195-199.
- Hutchings, G. J. (2008). Nanocrystalline gold and gold palladium alloy catalysts for chemical synthesis. **Chemical Communications**. 10: 1148-1664.
- Kesavan, L., Tiruvalam, R., Rahim, M. H. A., Saiman, M. I. B., Enashe, D. I., Jenkins, R. L., Dimitratos, N., Lopez-Sanchez, J. A., Taylor, S. H., Knight, D. W., Kiely, C. J. and Kuivila, H. G. (1954) Electrophilic displacement reactions. III. kinetics of the reaction between hydrogen peroxide and benzenboronic acid. **Journal of the american chemical society**. 76: 870-874.
- Murugadoss, A. and Sakurai, H. (2011). Chitosan-stabilized gold, gold–palladium, and gold–platinum nanoclusters as efficient catalysts for aerobic oxidation of alcohols. **Journal of Molecular Catalysis A: Chemical**. 341: 1-6.

- Murugadoss, A., Kai, N. and Sakurai, H. (2012). Synthesis of bimetallic gold–silver alloy nanoclusters by simple mortar grinding. **Nanoscale**. 4: 1280-1282.
- Sakurai, H., Tsunoyama, H. and Tsukuda, T. (2007). Oxidative homo-coupling of potassium aryltrifluoroborates catalyzed by gold nanocluster under aerobic conditions. **Journal of Organometallic Chemistry**. 692: 368-374.
- Scott, R. W. J., Wilson, O. M., Oh, S.-K., Kenik, E. A. and Crooks, R. M. (2004). Bimetallic palladium–gold dendrimer-encapsulated catalysts. **Journal of American Chemical Society**. 126: 15583-15591.
- Toshima, N., Harada, M., Yamazaki, Y. and Asakura, K. (1992). Catalytic activity and structural analysis of polymer-protected gold-palladium bimetallic clusters prepared by the simultaneous reduction of hydrogen tetrachloroaurate and palladium dichloride. **The Journal of Physical Chemistry**. 96: 9927-9933.
- Toshima, N. and Yonezawa, T. (1998). Bimetallic nanoparticles—novel materials for chemical and physical applications. **New Journal of Chemistry**. 22: 1179-1201.
- Tsukuda, T., Tsunoyama, H. and Sakurai, H. (2011). Aerobic oxidations catalyzed by colloidal nanogold. **Chemistry – An Asian Journal**. 6: 736-748.
- Tsunoyama, H., Ichikuni, N., Sakurai, H. and Tsukuda, T. (2009). Effect of electronic structures of Au clusters stabilized by poly(N-vinyl-2-pyrrolidone) on aerobic oxidation catalysis. **Journal of American Chemical Society**. 131: 7086-7093.
- Tsunoyama, H., Sakurai, H., Ichikuni, N., Negishi, Y. and Tsukuda, T. (2004). Colloidal gold nanoparticles as catalyst for carbon–carbon bond formation: application to aerobic homocoupling of phenylboronic acid in water. **Langmuir**. 20: 11293-11296.

- Venezia, A. M., Parola, V. L., Deganello, G., Pawelec, B. and Fierro, J. L. G. (2003). Synergetic effect of gold in Au/Pd catalysts during hydrodesulfurization reactions of model compounds. **Journal of Catalysis**. 215: 317-325.
- Villa, A., Campione, C. and Prati, L. (2007). Bimetallic gold/palladium catalysts for the selective liquid phase oxidation of glycerol. **Catalysis Letters**. 115: 133-136.
- Willis, N. and Guzman, J. (2008). Influence of the support during homocoupling of phenylboronic acid catalyzed by supported gold. **Applied Catalysis A: General**. 339: 68-75.
- Yudha, S., Dhital, R. N. and Sakurai, H. (2011). Gold- and gold-palladium/poly (1-vinylpyrrolidin-2-one) nanoclusters as quasi-homogeneous catalyst for aerobic oxidation of glycerol. **Tetrahedron Letters**. 52: 2633-2637.
- Zhang, H., Watanabe, T., Okumura, M., Haruta, M. and Toshima, N. (2012). Catalytically highly active top gold atom on palladium nanocluster. **Nature Materials**. 11: 49-52.
- Zhang, H., Xie, Y., Sun, Z., Tao, R., Huang, C., Zhao, Y. and Liu, Z. (2011). In-Situ loading ultrafine AuPd particles on ceria: highly active catalyst for solvent-free selective oxidation of benzyl alcohol. **Langmuir**. 27: 1152-1157.

CHAPTER VIII

CONCLUSIONS

Supported Fe catalysts were prepared, characterized and tested for phenol hydroxylation. Zeolite BEA and MCM-22 in ammonium form (NH_4BEA and $\text{NH}_4\text{MCM-22}$) and proton form (HBEA and HMCM-22) were used as supports. The Fe was loaded on the supports by three methods: incipient wetness impregnation (IWI), liquid state ion-exchange (LSIE) and physical mixing (PM). The Fe supported catalysts were characterized by several techniques. By powder X-ray diffraction (XRD), the structure of zeolite supports was remained after Fe loading. By N_2 adsorption-desorption analysis, their surface area and porosity were slightly lower than the bare support indicating a good dispersion of Fe. By ICP-OES, the Fe loading through IWI and SSIE were about 6 - 8 wt% and that through LSIE was about 1 - 3 wt%. By XANES, the main phase of Fe in all catalysts was Fe_2O_3 . By DR-UV-Vis, LSIE catalysts had isolated Fe_2O_3 located mainly at the ion-exchange position of zeolite whereas IWI and PM catalysts had the Fe_2O_3 particles were observed on the external surface of the zeolites. The catalysts were tested for phenol hydroxylation in a batch reactor at 70 °C with phenol: H_2O_2 molar ratio of 1:1. The observed products were benzoquinone (BQ), catechol (CAT) and hydroquinone (HQ). However, the results from carbon mass balance during the reaction indicated catalyst deactivation. The catalyst prepared from LSIE method was the most active giving the fastest reaction rate and the lowest mass loss for the reaction. The superior behavior of the

catalyst made from LSIE came from the presence of isolated Fe_2O_3 at the ion-exchange position of zeolite. Since the zeolite acidity from the presence of Al might induce the formation of tar for the phenol hydroxylation. The zeolite HBEA was dealuminated by HNO_3 at different times and Fe was inserted to the T-vacant site by LSIE method. By XRD, the contraction of zeolite lattice was observed for dealuminated BEA (D-BEA). After the Fe insertion, the zeolite lattice expanded, particularly the d_{302} spacing. The isolated Fe_2O_3 at the ion-exchange position was predominantly observed for the Fe supported on D-BEA. The prepared catalysts were tested regarding their quality for phenol hydroxylation. The reaction rate was decreased and correlated with the increase of dealumination time. Then, the rate was increased by the sample dealuminated for 240 min attributing to an opening of the zeolite pore. Compared to Fe supported on BEA, the dealumination of BEA raised the CAT and HQ yields and reduced the mass loss. Comparison of product yields from the best catalyst from all supports (HBEA, D-BEA and HMCM-22) at 15 min is shown in Figure 8.1. Fe/D-BEA-30 was the most effective catalyst in this work. HQ selectivity was not improved by the narrow pore of MCM-22 and the pore may obstruct the diffusion of substrates leading to coking.

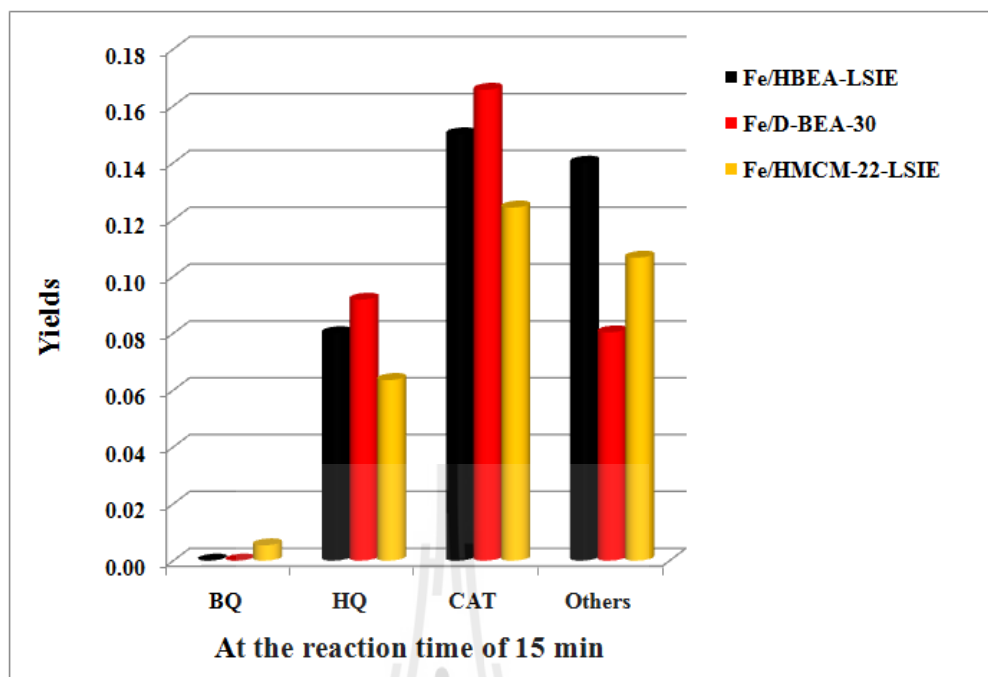


Figure 8.1 Product yields during the phenol hydroxylation of Fe/HBEA-LSIE, Fe/D-BEA and Fe/HMCM-22-LSIE.

To understand the mass loss, the spent catalysts were studied by TPO. The carbon mass loss was in good agreement with results from TPO. Amount of coke was proportional to Fe loading. Besides, the phenol hydroxylation was monitored by ATR-FT-IR. Deep oxidation of CAT, HQ and BQ by H_2O_2 was observed and yielded organic acids which were further confirmed by HPLC. Therefore, the causes of mass loss in phenol hydroxylation were from formation of coke and organic acids. In summary, there were several factors that affected the phenol hydroxylation including preparation method which resulted in different form of Fe, type of zeolite and Al contents in the zeolite BEA.

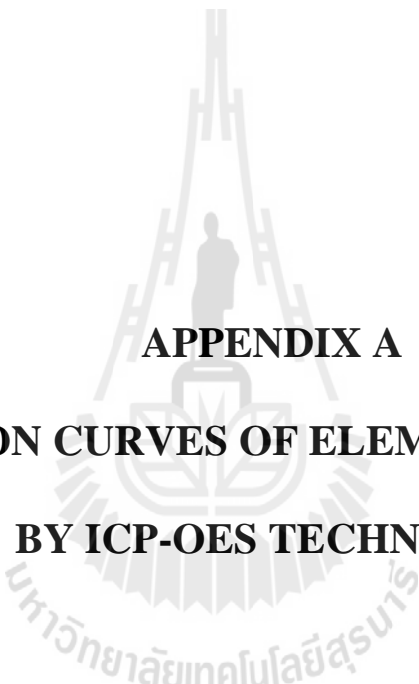
For the homocoupling of arylboronic acid, it was investigated over bimetallic Au/Pd alloy nanoclusters stabilized by chitosan. Influence of bimetallic ratio to the

catalytic and selectivity was understood. The catalyst $\text{Au}_{0.81}\text{Pd}_{0.19}:\text{chit}$ was the most active, particularly in comparison with monometallic $\text{Au}:\text{chit}$. The observed Hammett correlation indicated that the reaction likely occurred by multiple mechanisms or multiple catalytic sites probably involving in the bimetallic catalysis.





APPENDICES



APPENDIX A
CALIBRATION CURVES OF ELEMENTAL ANALYSIS
BY ICP-OES TECHNIQUE

Calibration for ICP-OES analysis

The calibration curves for Si, Al and Fe were constructed by the following procedure. The stock solution of Si with the concentration (C) of 1000 ppm was diluted with the 2% HNO₃ aqueous solution to 7 concentrations following these orders: 0.01C, 0.02C, 0.03C, 0.04C, 0.05C, 0.06C, 0.07C and 0.08C.

The stock solution of Al with the concentration (C) of 500 ppm was diluted with the 2% HNO₃ aqueous solution to 7 concentrations following these orders: 0.002C, 0.006C, 0.012C, 0.018C, 0.024C, 0.030C and 0.036C.

The stock solution of Fe with the concentration (C) of 500 ppm was diluted with the 2% HNO₃ aqueous solution to 7 concentrations following the order similar to Al.

A series of standard solutions was mixed together and diluted in the volumetric flasks number 1-7, respectively. Finally, they were analyzed by ICP-OES. The respond signal was plotted with the concentration of each standard.

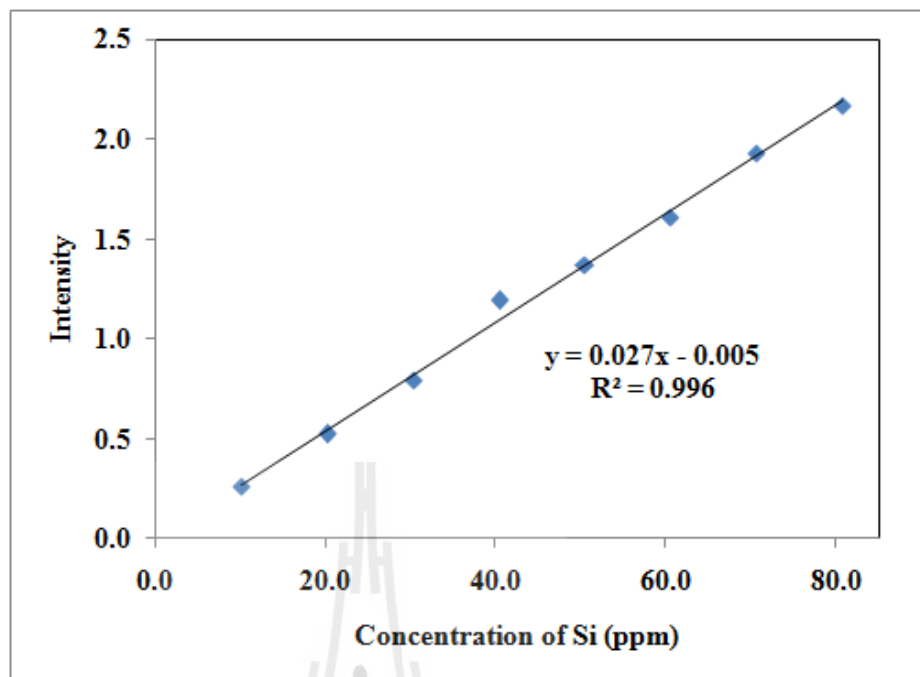


Figure A-1 Calibration curve of Si for ICP-OES.

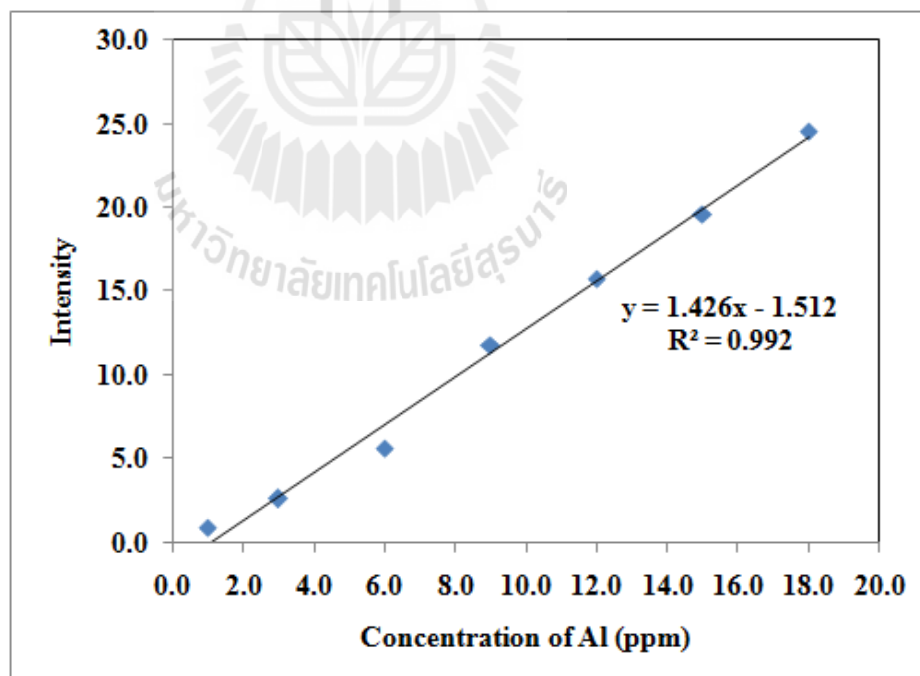


Figure A-2 Calibration curve of Al for ICP-OES.

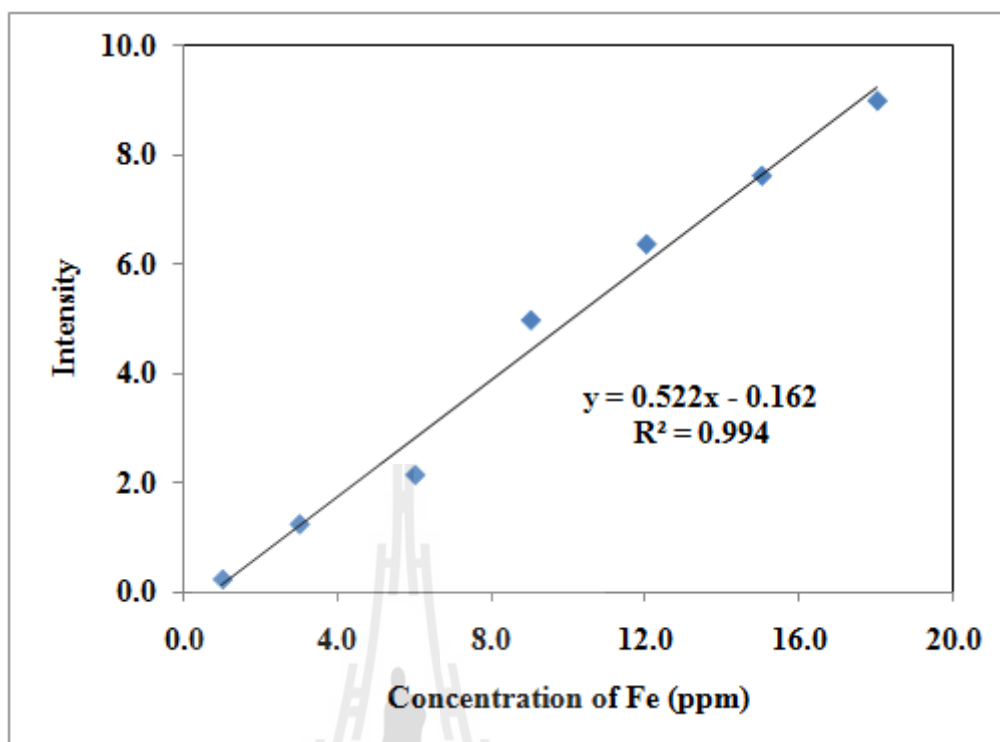


Figure A-3 Calibration curve of Fe for ICP-OES.



The elemental analysis results from ICP-OES technique were concluded into Table A-1 and A-2 as follows;

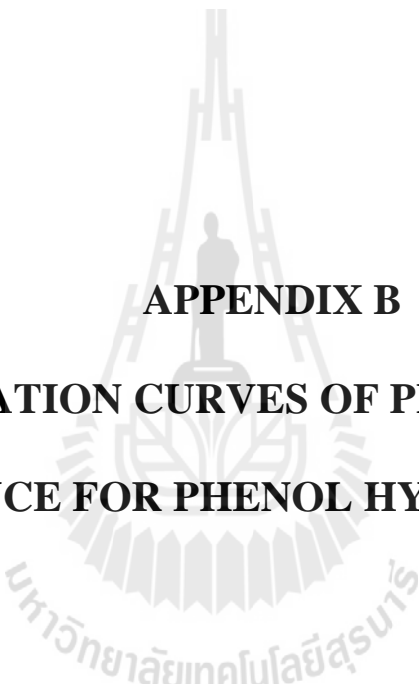
Table A-1 Elemental analysis of zeolite BEA and supported Fe catalysts.

Catalyst	% Fe (wt/wt)	Mole of Fe (g ⁻¹)	Mole of Si (g ⁻¹)	Mole of Al (g ⁻¹)	Si/Al mole ratio
HBEA	-	-	0.01089	0.00117	9.31
NH ₄ BEA	-	-	0.01143	0.00117	9.77
Fe/HBEA-IWI	6.21	0.0011	0.01129	0.00107	10.58
Fe/HBEA-LSIE	1.45	0.0003	0.01296	0.00103	12.63
Fe/NH ₄ BEA-22-LSIE	3.12	0.0006	0.01213	0.00093	13.05
Fe/HBEA-PM	7.70	0.0013	0.01183	0.00108	10.92

Table A-2 Elemental analysis of zeolite MCM-22 and supported Fe catalysts.

Catalyst	% Fe (wt/wt)	Mole of Fe (g ⁻¹)	Mole of Si (g ⁻¹)	Mole of Al (g ⁻¹)	Si/Al mole ratio
HMCM-22	-	-	0.01512	0.00092	16.43
NH ₄ MCM-22	-	-	0.01583	0.00096	16.49
Fe/HMCM-22-IWI	6.05	0.0011	0.01415	0.00088	16.08
Fe/HMCM-22-LSIE	0.85	0.0002	0.01507	0.00090	16.74
Fe/NH ₄ MCM-22-LSIE	0.92	0.0002	0.01470	0.00090	16.33
Fe/HMCM-22-PM	6.50	0.0012	0.01356	0.00099	13.69





APPENDIX B

**CALIBRATION CURVES OF PRODUCTS AND
REACTANCE FOR PHENOL HYDROXYLATION**

Calibration curve of phenol hydroxylation

The calibration curve was constructed from the mixed standard solution by the following procedure. The stock solution of phenol with the concentration (C) of 5×10^{-2} M was prepared by dissolving 0.2365g of phenol in ethanol 50 mL. Then it was diluted with the ethanol to 7 concentrations following these orders: 0.02C, 0.04C, 0.12C, 0.2C, 0.28C, 0.38C and 0.43C.

The stock solution of catechol with the concentration (C) of 5×10^{-2} M was prepared by dissolving 0.2809 g of catechol in ethanol 50 mL. Then it was diluted with the ethanol to 7 concentrations following these orders: 0.02C, 0.06C, 0.12C, 0.18C, 0.24C, 0.30C and 0.4C

The stock solution of hydroquinone with the concentration (C) of 5×10^{-2} M was prepared by dissolving 0.2758 g of hydroquinone in ethanol 50 mL. Then it was diluted with the ethanol to 7 concentration followings these order: 0.02C, 0.04C, 0.08C, 0.12C, 0.16C, 0.2C and 0.28C.

The stock solution of benzoquinone with the concentration (C) of 1×10^{-2} M was prepared by dissolving 0.1092 g of hydroquinone in ethanol 100 mL. Then it was diluted with the ethanol to 7 concentration followings these order: 0.008C, 0.025C, 0.05C, 0.1C, 0.15C, 0.2C and 0.30C.

A series of standard solutions was mixed together and diluted in the volumetric flasks number 1-7, respectively. Toluene was used as internal standard. Finally, they were analyzed by GC. The respond peak area ratio of standards/toluene was plotted with the mole of each standard.

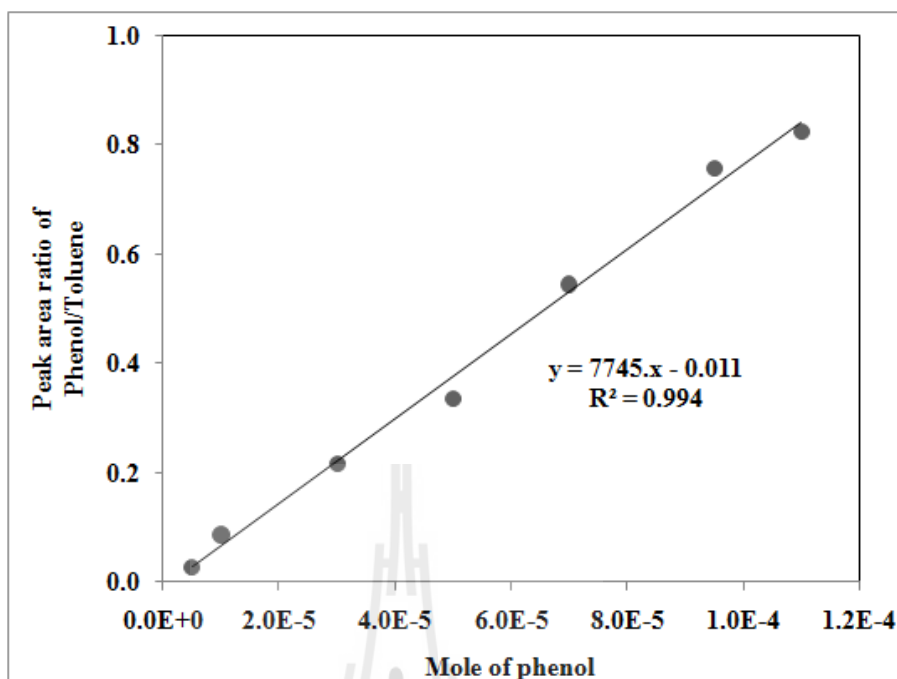


Figure B-1 Calibration curve of phenol for phenol hydroxylation.

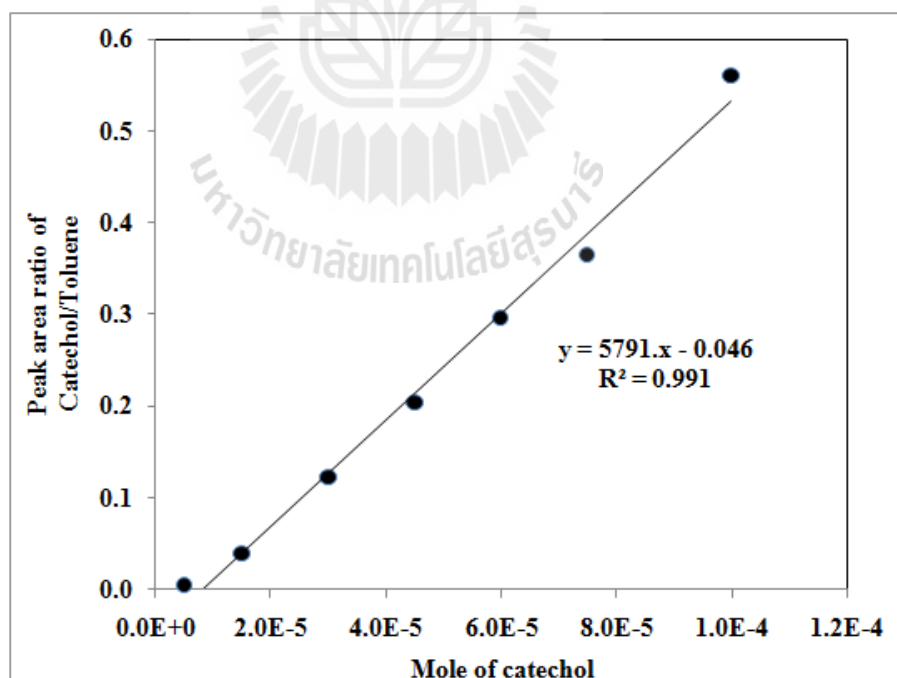


Figure B-2 Calibration curve of catechol for phenol hydroxylation.

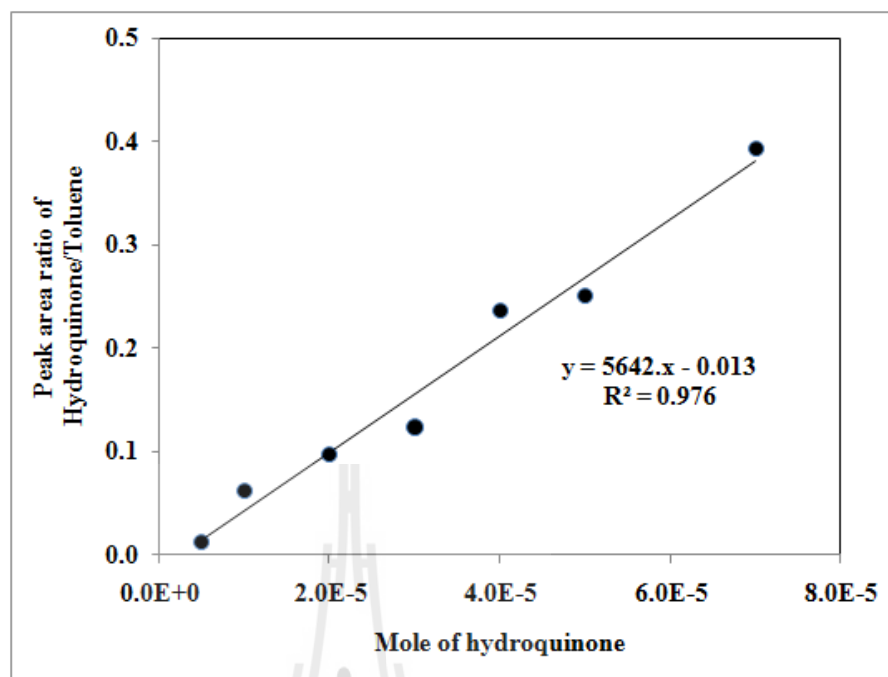


Figure B-3 Calibration curve of hydroquinone for phenol hydroxylation.

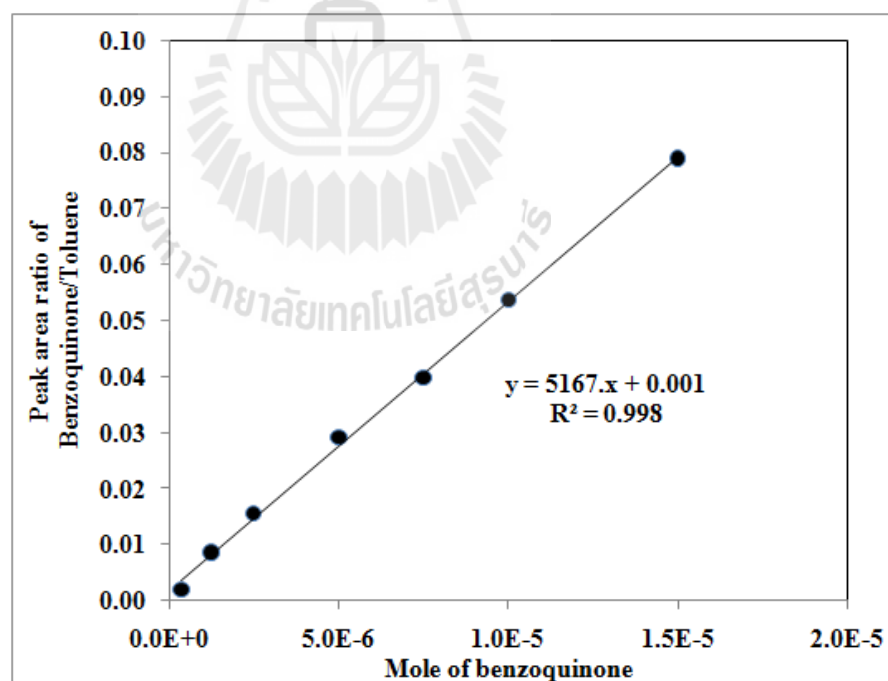


Figure B-4 Calibration curve of benzoquinone for phenol hydroxylation.

Calculation for phenol conversion

The conversion of phenol was calculated from this equation;

$$\% X_{phenol} = \left(\frac{\text{Initial mole of phenol} - \text{Final mole of phenol}}{\text{Initial mole of phenol}} \right) \times 100$$

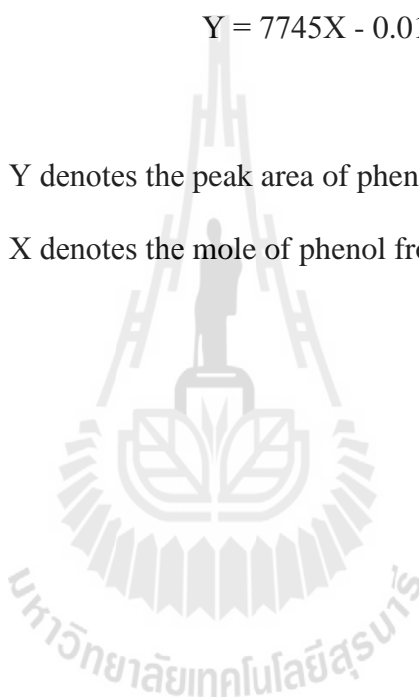
Concentration of phenol was calculated as follows;

$$Y = 7745X - 0.011$$

where

Y denotes the peak area of phenol from an analyte.

X denotes the mole of phenol from an analyte.



Calculation for carbon loss (mole)

The mole of carbon loss was calculated based on carbon balance from this equation;

$$\% \text{ Carbon loss (mole)} = \left(\frac{\text{spent phenol (mole)} - \Sigma \text{CAT+ HQ + BQ (mole)}}{\text{spent phenol (mole)}} \right) \times 100$$

$$\text{Spent phenol (mole)} = \text{Initial phenol (mole)} - \text{Final phenol (mole)}$$

Concentration of CAT, HQ and BQ was calculated as follows;

$$\text{Mole of CAT;} \quad Y = 5791X - 0.046$$

$$\text{Mole of HQ;} \quad Y = 5642X - 0.013$$

$$\text{Mole of BQ;} \quad Y = 5167X - 0.001$$

where

Y denotes the peak area of CAT, HQ and BQ from an analyte,

X denotes the mole of CAT, HQ and BQ from an analyte.



Calculation for product selectivity

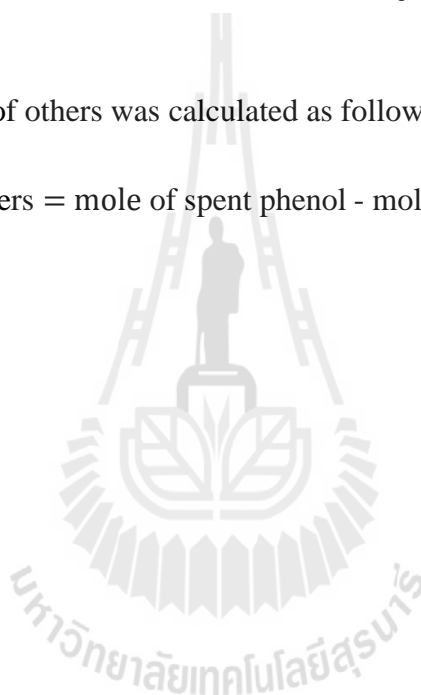
The product selectivity was calculated as follows;

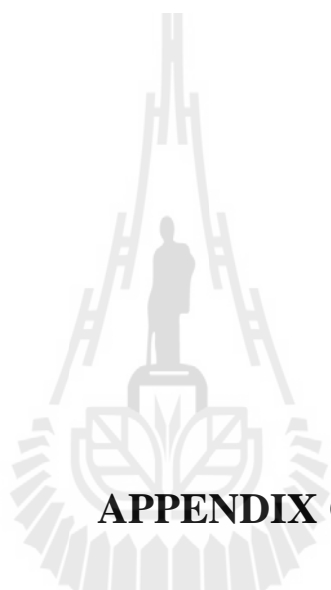
$$\% \text{Product selectivity} = \left(\frac{\text{mole of target product}}{\text{mole of CAT} + \text{HQ} + \text{BQ} + \text{others}} \right) \times 100$$

where

Mole of others was calculated as follows;

Mole of others = mole of spent phenol - mole of CAT, HQ and BQ





APPENDIX C

DATA FROM N₂ ADSORPTION-DESORPTION

Table C-1 N₂ adsorption-desorption of HBEA.

P/P0	Volume adsorbed	P/P0	Volume adsorbed	P/P0	Volume adsorbed
0.0000388	10.16570	0.0959000	179.73260	0.1510100	183.21710
0.0000332	20.35120	0.1008300	180.10850	0.1009400	180.28550
0.0000342	30.49220	0.1467600	182.83540	0.0892300	179.37700
0.0000330	40.65370	0.2034600	185.21290	0.0800400	178.61020
0.0000306	50.83110	0.2548200	186.79360	0.0705100	177.66040
0.0000296	61.01000	0.3044900	188.04680	0.0602700	176.52510
0.0000290	71.18890	0.3528600	189.07430	0.0503900	175.23930
0.0000299	81.36680	0.4004600	189.94800	0.0402800	173.65120
0.0000350	91.54270	0.4504700	190.76740	0.0303100	171.63950
0.0000467	101.71450	0.5006300	191.51200	0.0206100	168.96970
0.0000743	111.87240	0.5506000	192.19160		
0.0001380	121.97310	0.6006600	192.84750		
0.0002987	132.10700	0.6508300	193.48880		
0.0007910	142.12990	0.7008200	194.14180		
0.0024000	151.71520	0.7509600	194.83400		
0.0028900	153.21370	0.8008400	195.63230		
0.0049800	157.44190	0.8509300	196.62950		
0.0068100	160.53460	0.9007300	198.09830		
0.0092500	162.81600	0.9496900	200.95230		
0.0102200	163.56490	0.9849200	208.59950		
0.0154300	166.46710	0.9441700	201.53270		
0.0197700	168.22540	0.8875600	198.29290		
0.0248600	169.85060	0.8345700	196.82500		
0.0301600	171.22450	0.7835900	195.85530		
0.0350900	172.31050	0.7519100	195.31590		
0.0403300	173.31650	0.7012300	194.61440		
0.0452400	174.15350	0.6514100	193.97190		
0.0504000	174.93920	0.6012100	193.34580		
0.0557800	175.68270	0.5511800	192.72430		
0.0605400	176.28330	0.5011200	192.08690		
0.0655800	176.92480	0.4515700	191.10870		
0.0706000	177.45180	0.4004500	190.06980		
0.0758500	177.98220	0.3508000	189.10870		
0.0808800	178.46400	0.3010800	188.03190		
0.0858900	178.91250	0.2509300	186.75930		
0.0909500	179.33880	0.2008200	185.22970		

Table C-2 N₂ adsorption-desorption of NH₄BEA.

P/P0	Volume adsorbed	P/P0	Volume adsorbed	P/P0	Volume adsorbed
0.0000289	20.32380	0.1009800	182.78110	0.3505200	189.10200
0.0000265	30.49090	0.1471000	185.02090	0.3006900	188.48930
0.0000237	40.65690	0.2038200	186.83540	0.2505900	187.68450
0.0000199	50.82240	0.2554700	187.92350	0.2005200	186.62020
0.0000177	60.98730	0.3047300	188.70330	0.1508500	185.06070
0.0000158	71.15200	0.1009800	182.78110	0.1010300	182.68110
0.0000159	81.31570	0.1471000	185.02090	0.0898400	181.93580
0.0000177	91.47930	0.2038200	186.83540	0.0800900	181.20890
0.0000227	101.64190	0.2554700	187.92350	0.0704200	180.38600
0.0000354	111.80260	0.3047300	188.70330	0.0603900	179.39070
0.0000653	121.95830	0.3508000	189.23660	0.0503900	178.20900
0.0001415	132.10030	0.4002200	189.69510	0.0404200	176.75170
0.0003698	142.19670	0.4503700	190.05630	0.0304800	174.86380
0.0012000	152.09770	0.5003300	190.32970	0.0206600	172.28870
0.0029200	158.73940	0.5503100	190.54600	0.0099300	167.39840
0.0049800	162.52080	0.6003300	190.72300		
0.0068600	164.72960	0.6502700	190.87950		
0.0091700	166.78220	0.7002100	191.05830		
0.0104300	167.69400	0.7503100	191.26240		
0.0152900	170.29020	0.8002700	191.56110		
0.0199900	172.08950	0.8501900	192.05710		
0.0247600	173.52230	0.9000600	192.96010		
0.0300300	174.81120	0.9486700	195.14360		
0.0351300	175.86170	0.9840400	201.57910		
0.0401900	176.77260	0.9432600	195.54770		
0.0453100	177.57380	0.8861500	193.06930		
0.0502400	178.27840	0.8328000	192.18880		
0.0558100	178.97620	0.7820000	191.73210		
0.0604800	179.50640	0.7314700	191.45290		
0.0657200	180.04790	0.6814100	191.24520		
0.0708600	180.53200	0.6506500	191.12300		
0.0760500	180.97370	0.6005100	190.97130		
0.0811300	181.38740	0.5506700	190.79950		
0.0860700	181.76300	0.5004700	190.60770		
0.0910700	182.12400	0.4510800	190.10030		
0.0960100	182.46260	0.3999400	189.59640		

Table C-3 N₂ adsorption-desorption of Fe/HBEA-IWI.

P/P0	Volume adsorbed	P/P0	Volume adsorbed	P/P0	Volume adsorbed
0.0000115	10.12140	0.0952200	175.24580	0.0600400	171.88570
0.0000146	20.24650	0.1001800	175.61040	0.0502400	170.72080
0.0000155	30.37280	0.1450600	178.22050	0.0403100	169.30610
0.0000159	40.49970	0.3024900	182.65640	0.0303500	167.47390
0.0000166	50.62640	0.3501200	183.36160	0.0201700	164.92190
0.0000180	60.75330	0.3973700	183.91880	0.0099600	160.53230
0.0000208	70.87990	0.4471200	184.39170		
0.0000261	81.00610	0.4967800	184.76020		
0.0000351	91.13160	0.5464100	185.07350		
0.0000511	101.25370	0.5961400	185.33700		
0.0000822	111.37300	0.7947100	186.46510		
0.0001443	121.48500	0.8441200	187.09980		
0.0002879	131.57460	0.8941100	188.01080		
0.0007160	141.57730	0.9454400	190.47560		
0.0024000	151.19530	0.9828100	198.13280		
0.0029400	152.58220	0.9292500	189.60530		
0.0049500	156.00200	0.8801300	187.74410		
0.0071900	158.39230	0.8286000	186.81810		
0.0091200	159.94570	0.7781200	186.29530		
0.0098100	160.41230	0.7280700	185.91620		
0.0147400	162.93310	0.6966800	185.70340		
0.0198800	164.82730	0.6471900	185.43750		
0.0247300	166.19890	0.5974600	185.18320		
0.0297900	167.36590	0.5476900	184.91590		
0.0348800	168.39230	0.4980800	184.60420		
0.0399800	169.28780	0.4485400	184.13120		
0.0450000	170.05970	0.3989200	183.56630		
0.0499400	170.74480	0.3494300	182.97990		
0.0548900	171.38360	0.2991800	182.24290		
0.0604700	172.05200	0.2493300	181.29650		
0.0650600	172.55380	0.1996900	180.07280		
0.0702000	173.08230	0.1504500	178.24750		
0.0752200	173.56640	0.1006600	175.48350		
0.0802600	174.04260	0.0890800	174.62670		
0.0853400	174.48080	0.0797300	173.84030		
0.0904300	174.88650	0.0699100	172.91880		

Table C-4 N₂ adsorption-desorption of Fe/HBEA-LSIE.

P/P0	Volume adsorbed	P/P0	Volume adsorbed	P/P0	Volume adsorbed
0.000000	0.00000	0.1009600	176.94130	0.0900800	175.80040
0.0000414	20.30130	0.1462000	179.79440	0.0801400	174.87470
0.0000426	30.44000	0.2040200	182.28140	0.0703600	173.84700
0.0000410	40.57420	0.2558500	183.86210	0.0603900	172.65030
0.0000383	50.70510	0.3534200	186.01570	0.0503100	171.23010
0.0000360	60.83370	0.4006500	186.80650	0.0403900	169.53450
0.0000326	71.00220	0.4508200	187.53010	0.0304400	167.36170
0.0000330	81.13210	0.5007500	188.16910	0.0205900	164.37590
0.0000379	91.26010	0.5509600	188.74740	0.0102400	159.04460
0.0000498	101.42330	0.6009900	189.28470		
0.0000824	111.57990	0.6511700	189.77500		
0.0001637	121.72170	0.7001200	190.28500		
0.0003933	131.81590	0.7503500	190.83500		
0.0011300	141.73860	0.8001900	191.45540		
0.0029000	149.62470	0.8500600	192.24270		
0.0049100	153.78730	0.8998800	193.41690		
0.0069400	156.46530	0.9488200	195.71900		
0.0091100	158.56640	0.9845700	201.83440		
0.0096700	159.01510	0.9420900	195.87020		
0.0149900	162.31470	0.8854500	193.44160		
0.0200600	164.49920	0.8330200	192.31620		
0.0246600	166.04980	0.7822000	191.55370		
0.0299500	167.51670	0.7507300	191.14430		
0.0351800	168.73540	0.7002100	190.60210		
0.0401300	169.74030	0.6505100	190.10660		
0.0452000	170.65220	0.6004000	189.61630		
0.0502500	171.46610	0.5503200	189.12550		
0.0555700	172.26410	0.5003300	188.60420		
0.0604200	172.91190	0.4509800	187.69420		
0.0655800	173.55330	0.3997400	186.67590		
0.0707300	174.14420	0.3500100	185.77670		
0.0758000	174.67030	0.3007800	184.76080		
0.0809800	175.18660	0.2505000	183.50560		
0.0860800	175.66780	0.2004900	181.96110		
0.0910400	176.10790	0.1509100	179.82400		
0.0960600	176.53130	0.1008400	176.69730		

Table C-5 N₂ adsorption-desorption of Fe/NH₄BEA-LSIE.

P/P0	Volume adsorbed	P/P0	Volume adsorbed	P/P0	Volume adsorbed
0.0000180	20.33950	0.1459500	181.74930	0.0895200	177.39420
0.0000141	30.51410	0.2038300	184.57400	0.0801000	176.43870
0.0000113	40.68840	0.2557500	186.37900	0.0703300	175.33530
0.0000096	50.86210	0.3055500	187.76670	0.0603100	174.04930
0.0000091	61.03510	0.3534300	188.86900	0.0503700	172.56620
0.0000100	71.20750	0.4004400	189.78290	0.0402800	170.75600
0.0000132	81.37930	0.4503700	190.62800	0.0304300	168.51480
0.0000204	91.54920	0.5004500	191.38650	0.0203400	165.36450
0.0000357	101.71570	0.5505400	192.07200	0.0105000	160.19820
0.0000695	111.87500	0.6004900	192.71330		
0.0001502	122.01720	0.6505900	193.32480		
0.0003719	132.10970	0.7005300	193.94620		
0.0010700	142.02950	0.7506800	194.62270		
0.0028700	150.24010	0.8005100	195.40400		
0.0050100	154.69700	0.8504500	196.39660		
0.0070600	157.40530	0.9002900	197.85910		
0.0093000	159.56450	0.9492100	200.70280		
0.0102700	160.34250	0.9843100	208.12010		
0.0153500	163.43120	0.9439400	200.80570		
0.0199800	165.46320	0.8863500	197.73380		
0.0247700	167.12910	0.8333800	196.31140		
0.0300800	168.64650	0.7825800	195.34690		
0.0351200	169.87030	0.7508000	194.82300		
0.0401800	170.93890	0.7003100	194.12450		
0.0451800	171.88730	0.6503800	193.48580		
0.0502400	172.74800	0.6003800	192.87320		
0.0554900	173.56220	0.5503600	192.25520		
0.0604600	174.27490	0.5003400	191.61310		
0.0655300	174.94300	0.4506800	190.78270		
0.0706400	175.57230	0.4003600	189.72030		
0.0757900	176.16880	0.3499300	188.66760		
0.0808600	176.71630	0.3006500	187.50170		
0.0860600	177.24530	0.2505500	186.07540		
0.0910400	177.72590	0.2005700	184.31090		
0.0959800	178.18160	0.1509400	181.90010		
0.1009300	178.61500	0.1009400	178.43600		

Table C-6 N₂ adsorption-desorption of Fe/HBEA-PM.

P/P0	Volume adsorbed	P/P0	Volume adsorbed	P/P0	Volume adsorbed
0.0000271	20.35410	0.2540700	145.98280	0.2003700	144.45610
0.0000207	30.53750	0.3039100	147.02400	0.1506900	142.77060
0.0000161	40.71960	0.3505700	147.85460	0.1006900	140.42450
0.0000136	50.90090	0.4006800	148.61690	0.0901400	139.78470
0.0000133	61.08150	0.4508000	149.28460	0.0802300	139.11270
0.0000164	71.26150	0.2540700	145.98280	0.0703900	138.37270
0.0000269	81.43970	0.3039100	147.02400	0.0603900	137.51210
0.0000581	91.61150	0.3505700	147.85460	0.0503600	136.50880
0.0001590	101.76140	0.4006800	148.61690	0.0403200	135.29650
0.0005763	111.80660	0.4508000	149.28460	0.0303400	133.76530
0.0027500	121.28280	0.5007900	149.89350	0.0204600	131.66650
0.0029200	121.60630	0.5508600	150.46890	0.0102300	128.00410
0.0049000	124.39590	0.6008700	151.03610		
0.0070700	126.31310	0.6510300	151.59210		
0.0096300	127.95990	0.7009300	152.20940		
0.0107700	128.54480	0.7510800	152.94300		
0.0151100	130.30090	0.8011600	153.81330		
0.0202300	131.81570	0.8509800	155.00220		
0.0249800	132.91440	0.9008500	156.80340		
0.0301700	133.90830	0.9493900	160.38150		
0.0352100	134.73120	0.9836000	169.01210		
0.0402800	135.45250	0.9448500	160.98130		
0.0452700	136.08690	0.8882500	156.75840		
0.0502900	136.66370	0.8340100	154.90130		
0.0556200	137.21840	0.7827600	153.74630		
0.0604300	137.67940	0.7510800	153.15970		
0.0655500	138.13220	0.7003800	152.39910		
0.0706100	138.55150	0.6505000	151.74700		
0.0756900	138.94520	0.6004600	151.13650		
0.0807800	139.31680	0.5504000	150.57770		
0.0859000	139.66520	0.5004100	150.01070		
0.0909000	139.98540	0.4506900	149.24760		
0.0958600	140.29240	0.4001100	148.43820		
0.1008300	140.58560	0.3503100	147.64540		
0.1474700	142.77660	0.3005500	146.76060		
0.2029600	144.69130	0.2504900	145.71020		

Table C-7 N₂ adsorption-desorption of HMCM-22.

P/P0	Volume adsorbed	P/P0	Volume adsorbed	P/P0	Volume adsorbed
-0.000408	3.69770	0.1770000	137.99000	0.9942000	406.38000
-0.000815	8.02290	0.2029000	139.14000	0.9926000	377.65000
-0.000408	12.35100	0.2285000	140.19000	0.9905000	350.31000
-0.000816	16.67800	0.2541000	141.17000	0.9884000	324.25000
-0.0001631	21.00800	0.2795000	142.10000	0.9856000	299.24000
-0.0001631	25.34800	0.3047000	142.97000	0.9758000	275.84000
-0.0002039	29.70100	0.3499000	144.47000	0.9748000	249.43000
-0.0002447	34.05600	0.3993000	146.04000	0.9596000	225.24000
-0.0002039	38.41000	0.4491000	147.60000	0.9411000	210.72000
-0.0002447	42.77100	0.4986000	149.20000	0.8874000	189.43000
-0.0002448	47.12700	0.5477000	150.91000		
-0.0002448	51.48500	0.5967000	152.77000		
-0.0002448	55.84200	0.6554000	155.32000		
-0.0002447	60.19800	0.7050000	157.91000		
-0.0002448	64.55100	0.7523000	160.87000		
-0.0002448	68.90700	0.7992000	164.49000		
-0.0002448	73.25900	0.8496000	169.91000		
-0.0002040	77.60500	0.8913000	176.86000		
-0.0002448	81.95900	0.8988000	178.40000		
-0.0002448	86.30500	0.9317000	188.88000		
-0.0001632	90.63800	0.9577000	204.26000		
-0.0001632	94.96500	0.9785000	231.02000		
-0.0000816	99.27500	0.9884000	260.21000		
0.0001060	103.57000	0.9925000	280.59000		
0.0004815	108.25000	0.9939000	301.54000		
0.0014700	112.77000	0.9954000	322.33000		
0.0036700	116.92000	0.9961000	343.04000		
0.0081600	120.69000	0.9971000	363.62000		
0.0195900	124.77000	0.9978000	384.07000		
0.0285700	126.60000	0.9981000	404.54000		
0.0395800	128.27000	0.9986000	424.90000		
0.0513700	129.69000	0.9989000	445.31000		
0.0722500	131.67000	0.9988000	465.60000		
0.0975900	133.58000	0.9993000	485.93000		
0.1241000	135.26000	0.9972000	458.07000		
0.1508000	136.72000	0.9959000	431.73000		

Table C-8 N₂ adsorption-desorption of NH₄MCM-22.

P/P ₀	Volume adsorbed	P/P ₀	Volume adsorbed	P/P ₀	Volume adsorbed
0.000000	3.53530	0.3506000	139.39000	0.5525000	151.61000
-0.0000409	7.66350	0.3999000	140.86000	0.5030000	149.86000
-0.0000409	11.78000	0.4501000	142.33000	0.4532000	146.11000
-0.0000818	15.91200	0.4993000	143.85000	0.3935000	143.70000
-0.0000818	20.03100	0.5484000	145.49000	0.3492000	142.37000
-0.0000818	24.16300	0.5968000	147.30000	0.3005000	140.87000
-0.0000818	28.30500	0.6556000	149.80000	0.2713000	139.90000
-0.0000819	32.44700	0.7058000	152.33000	0.2456000	139.01000
-0.0000819	36.59300	0.7527000	155.19000	0.2207000	138.10000
-0.0000819	40.72100	0.7996000	158.77000	0.1960000	137.12000
-0.0000819	44.86100	0.8499000	164.12000	0.1718000	136.06000
-0.0001228	49.00200	0.8918000	171.06000	0.1473000	134.92000
-0.0000819	53.14200	0.8989000	172.57000	0.1233000	133.65000
-0.0001637	57.27900	0.9311000	183.16000	0.0994200	132.22000
-0.0001228	61.42700	0.9587000	198.70000	0.0769600	130.64000
-0.0000819	65.55700	0.9795000	225.81000	0.0491200	128.15000
-0.0001228	69.70700	0.9869000	245.74000	0.0405400	127.16000
-0.0001229	73.84900	0.9914000	266.49000	0.0340600	126.31000
-0.0000819	77.98600	0.9937000	287.79000	0.0224200	124.32000
-0.0000819	82.13300	0.9952000	308.93000	0.0141600	122.25000
-0.0000819	86.26600	0.9961000	329.98000	0.0124600	121.67000
-0.0000410	90.39300	0.9973000	350.95000	0.0097800	120.60000
0.0000000	94.52200	0.9981000	371.85000	0.0076700	119.57000
0.0000657	98.62700	0.9980000	392.72000	0.0058400	118.36000
0.0003583	103.14000	0.9992000	413.54000		
0.0011000	107.53000	0.9960000	383.98000		
0.0028200	111.68000	0.9938000	356.65000		
0.0064300	115.27000	0.9915000	335.99000		
0.0173800	119.72000	0.9885000	307.45000		
0.0268500	121.77000	0.9842000	280.90000		
0.0386200	123.58000	0.9785000	255.84000		
0.0510100	125.05000	0.9660000	229.11000		
0.0723100	127.01000	0.9462000	206.23000		
0.0978800	128.89000	0.8930000	183.69000		
0.1245000	130.52000	0.8605000	176.68000		
0.1512000	131.93000	0.8517000	175.19000		
0.1773000	133.18000	0.8074000	168.36000		
0.2031000	134.31000	0.7982000	167.29000		
0.2289000	135.32000	0.7476000	162.28000		
0.2545000	136.25000	0.7005000	158.75000		
0.2798000	137.14000	0.6475000	155.72000		
0.3052000	137.98000	0.5944000	153.28000		

Table C-9 N₂ adsorption-desorption of Fe/HMCM-22-IWI.

P/P ₀	Volume adsorbed	P/P ₀	Volume adsorbed	P/P ₀	Volume adsorbed
0.00000	3.6690000	0.49940	133.6900000	0.54350	141.5100000
0.00000	7.9208000	0.54840	135.1200000	0.50090	138.1200000
0.00000	12.1790000	0.59740	136.6000000	0.45230	135.9000000
0.00000	16.4390000	0.65610	138.1700000	0.39380	134.6400000
0.00000	20.7120000	0.69660	139.8800000	0.34980	133.2000000
0.00000	24.9840000	0.75180	142.2400000	0.30090	132.2900000
-0.00004	29.2490000	0.79960	144.6400000	0.27150	131.4300000
-0.00004	33.5110000	0.85130	147.4800000	0.24590	130.5600000
-0.00004	37.7860000	0.88720	150.9500000	0.22110	129.6400000
-0.00004	42.0590000	0.89650	156.2100000	0.19650	128.6300000
-0.00004	46.3460000	0.93170	163.0400000	0.17190	127.5400000
-0.00004	50.6340000	0.95910	164.6300000	0.14740	126.3300000
-0.00004	54.9180000	0.97940	174.8900000	0.12330	124.9700000
-0.00004	59.1950000	0.98690	183.0400000	0.09924	123.4500000
0.00000	63.4750000	0.99150	209.5500000	0.07617	121.0400000
-0.00004	67.7550000	0.99510	238.1000000	0.04831	120.0800000
-0.00004	72.0360000	0.99610	258.2300000	0.03957	119.2400000
0.00003	76.3020000	0.99730	278.9900000	0.03304	117.8900000
0.00003	80.5630000	0.99810	299.6900000	0.02441	115.6200000
0.00019	84.8240000	0.99840	320.1400000	0.01446	115.0300000
0.00048	89.0700000	0.99850	340.4100000	0.01253	113.9500000
0.00135	93.7420000	0.99860	360.5800000	0.00969	113.1200000
0.00327	98.3690000	0.99960	380.7500000	0.00771	111.8900000
0.00744	102.8300000	0.99640	372.0400000		
0.01898	106.9400000	0.99420	345.1200000		
0.02838	110.6000000	0.99260	324.6700000		
0.03979	114.3900000	0.99050	296.1500000		
0.05179	116.0500000	0.98580	269.5400000		
0.07302	117.5600000	0.98170	244.4800000		
0.09847	118.8300000	0.97270	220.5900000		
0.12500	120.6300000	0.95630	196.9800000		
0.15140	122.3800000	0.94480	173.9100000		
0.17740	123.9000000	0.89180	167.1800000		
0.20300	125.2200000	0.86600	165.7800000		
0.22870	126.3700000	0.84970	159.2800000		
0.25400	127.4200000	0.81410	158.3200000		
0.27940	128.3700000	0.80130	153.4700000		
0.30470	129.2600000	0.74790	150.0800000		
0.35020	130.1000000	0.69960	147.1500000		
0.39960	130.9000000	0.64660	144.7900000		
0.44950	132.2500000	0.60420	143.2100000		

Table C-10 N₂ adsorption-desorption of Fe/HMCM-22-LSIE.

P/P ₀	Volume adsorbed	P/P ₀	Volume adsorbed	P/P ₀	Volume adsorbed
0.000000	3.79970	0.4495000	145.19000	0.6996000	161.42000
0.000000	8.81600	0.4994000	146.83000	0.6466000	158.42000
0.000000	13.82600	0.5484000	148.57000	0.6042000	156.44000
0.000000	18.84400	0.5974000	150.47000	0.5435000	154.01000
0.000000	23.86400	0.6561000	153.04000	0.5009000	152.46000
0.000000	28.88000	0.6966000	155.06000	0.4523000	148.77000
-0.000408	33.90800	0.7518000	158.45000	0.3938000	146.23000
-0.000408	38.93400	0.7996000	162.26000	0.3498000	144.80000
-0.000408	43.95700	0.8513000	167.85000	0.3009000	143.17000
-0.000409	48.99000	0.8872000	173.79000	0.2715000	142.13000
-0.000409	54.01500	0.8965000	175.75000	0.2459000	141.19000
-0.000409	59.04200	0.9317000	186.75000	0.2211000	140.22000
-0.000409	64.08200	0.9591000	202.56000	0.1965000	139.19000
-0.000408	69.10400	0.9794000	229.62000	0.1719000	138.09000
0.000000	74.13100	0.9869000	249.82000	0.1474000	136.89000
-0.000409	79.16000	0.9915000	270.90000	0.1233000	135.57000
-0.000409	84.18400	0.9951000	292.38000	0.0992400	134.09000
0.0000285	89.18800	0.9961000	313.59000	0.0761700	132.42000
0.0000285	94.20500	0.9973000	334.78000	0.0483100	129.83000
0.0001900	99.19300	0.9981000	355.79000	0.0395700	128.77000
0.0004823	104.10000	0.9984000	376.68000	0.0330400	127.85000
0.0013500	108.85000	0.9985000	397.61000	0.0244100	126.33000
0.0032700	113.26000	0.9986000	418.54000	0.0144600	123.84000
0.0074400	117.27000	0.9996000	439.45000	0.0125300	123.16000
0.0189800	121.81000	0.9974000	418.76000	0.0096900	121.91000
0.0283800	123.81000	0.9964000	389.02000	0.0077100	120.85000
0.0397900	125.56000	0.9942000	361.20000	0.0057600	119.39000
0.0517900	127.00000	0.9926000	339.78000		
0.0730200	129.00000	0.9905000	319.02000		
0.0984700	130.91000	0.9858000	291.29000		
0.1250000	132.57000	0.9817000	265.50000		
0.1514000	134.02000	0.9727000	241.41000		
0.1774000	135.31000	0.9563000	216.63000		
0.2030000	136.48000	0.9448000	209.24000		
0.2287000	137.56000	0.8918000	186.67000		
0.2540000	138.56000	0.8660000	180.75000		
0.2794000	139.51000	0.8497000	177.69000		
0.3047000	140.42000	0.8141000	171.90000		
0.3502000	141.97000	0.8013000	170.37000		
0.3996000	143.58000	0.7479000	164.99000		

Table C-11 N₂ adsorption-desorption of Fe/NH₄MCM-22-LSIE.

P/P ₀	Volume adsorbed	P/P ₀	Volume adsorbed	P/P ₀	Volume adsorbed
0.0000000	3.57160	0.4492000	135.96000	0.5937000	146.76000
0.0000000	8.25060	0.4988000	137.60000	0.5520000	145.10000
-0.0000817	12.93200	0.5479000	139.33000	0.5031000	143.31000
-0.0000409	17.60800	0.5967000	141.23000	0.4532000	139.51000
-0.0000817	22.28000	0.6558000	143.80000	0.3939000	136.99000
-0.0001226	26.96100	0.7059000	146.33000	0.3498000	135.58000
-0.0001635	31.64700	0.7531000	149.24000	0.3011000	133.96000
-0.0001635	36.33100	0.7998000	152.86000	0.2717000	132.93000
-0.0001635	41.01700	0.8508000	158.28000	0.2459000	131.97000
-0.0001635	45.70800	0.8929000	165.16000	0.2211000	131.01000
-0.0002044	50.41500	0.8997000	166.64000	0.1965000	129.98000
-0.0002045	55.11600	0.9329000	177.10000	0.1720000	128.88000
-0.0001636	59.81000	0.9599000	192.51000	0.1475000	127.68000
-0.0002453	64.52800	0.9755000	210.63000	0.1233000	126.38000
-0.0002045	69.22200	0.9882000	240.13000	0.0992700	124.93000
-0.0002045	73.92700	0.9924000	260.52000	0.0761900	123.31000
-0.0002045	78.63000	0.9946000	281.41000	0.0483400	120.78000
-0.0001636	83.33000	0.9953000	302.22000	0.0396600	119.76000
-0.0000818	88.00800	0.9968000	322.96000	0.0332600	118.87000
0.0000285	92.67500	0.9974000	343.45000	0.0247100	117.42000
0.0004827	97.25700	0.9973000	364.00000	0.0147600	115.02000
0.0015900	101.67000	0.9983000	384.42000	0.0120500	114.08000
0.0039700	105.70000	0.9982000	404.88000	0.0094200	112.99000
0.0087600	109.31000	0.9995000	425.25000	0.0078100	112.14000
0.0203400	113.20000	0.9966000	395.65000	0.0058000	110.77000
0.0292200	114.95000	0.9951000	367.99000		
0.0401100	116.58000	0.9931000	341.50000		
0.0518600	117.95000	0.9909000	310.64000		
0.0728800	119.89000	0.9872000	282.90000		
0.0982300	121.76000	0.9823000	257.20000		
0.1247000	123.40000	0.9751000	232.90000		
0.1510000	124.84000	0.9591000	207.89000		
0.1770000	126.13000	0.9385000	193.52000		
0.2028000	127.29000	0.8987000	178.00000		
0.2284000	128.38000	0.8639000	170.16000		
0.2539000	129.39000	0.8471000	167.39000		
0.2793000	130.34000	0.8040000	161.11000		
0.3046000	131.25000	0.7487000	155.66000		
0.3500000	132.77000	0.6999000	152.13000		
0.3993000	134.36000	0.6470000	149.16000		

Table C-12 N₂ adsorption-desorption of Fe/HMCM-22-PM.

P/P ₀	Volume adsorbed	P/P ₀	Volume adsorbed	P/P ₀	Volume adsorbed
0.000000	3.49640	0.3976000	129.90000	0.3027000	128.51000
-0.0000409	7.57550	0.4471000	131.69000	0.2724000	127.38000
-0.0000409	11.67800	0.4960000	133.57000	0.2466000	126.39000
-0.0001228	15.77900	0.5563000	136.07000	0.2213000	125.38000
-0.0002047	19.90300	0.5962000	137.91000	0.1967000	124.33000
-0.0001637	24.00900	0.6538000	140.89000	0.1721000	123.22000
-0.0002047	28.13200	0.7029000	143.93000	0.1478000	122.02000
-0.0002457	32.26200	0.7496000	147.45000	0.1237000	120.70000
-0.0002867	36.39400	0.8021000	152.67000	0.0998600	119.21000
-0.0002457	40.51500	0.8468000	158.99000	0.0775200	117.59000
-0.0002867	44.64000	0.8794000	165.57000	0.0498200	115.01000
-0.0002867	48.78100	0.8993000	170.61000	0.0412600	113.98000
-0.0002866	52.89900	0.9283000	181.31000	0.0348300	113.08000
-0.0002457	57.02800	0.9571000	196.66000	0.0230500	111.00000
-0.0002867	61.16000	0.9749000	214.06000	0.0147000	108.79000
-0.0002868	65.29800	0.9889000	243.03000	0.0122300	107.88000
-0.0002868	69.41800	0.9933000	262.95000	0.0098600	106.79000
-0.0002457	73.54500	0.9959000	283.47000	0.0075200	105.89000
-0.0001639	77.66300	0.9979000	303.76000	0.0058600	105.14000
-0.0001639	81.77600	1.0022000	323.62000		
-0.0000410	85.87600	0.9950000	306.79000		
0.0001905	89.94000	0.9913000	290.06000		
0.0008553	94.32000	0.9858000	263.39000		
0.0023300	98.49400	0.9795000	238.94000		
0.0055300	102.23000	0.9628000	212.54000		
0.0162700	107.08000	0.9402000	197.62000		
0.0257700	109.27000	0.8998000	181.53000		
0.0375600	111.21000	0.8738000	174.67000		
0.0502000	112.78000	0.8498000	169.56000		
0.0714500	114.85000	0.8090000	162.17000		
0.0971700	116.82000	0.8000000	160.89000		
0.1240000	118.53000	0.7513000	154.80000		
0.1506000	120.01000	0.6962000	149.73000		
0.1770000	121.30000	0.6491000	146.31000		
0.2029000	122.47000	0.5970000	143.19000		
0.2284000	123.55000	0.5449000	140.50000		
0.2537000	124.58000	0.4942000	137.97000		
0.2791000	125.55000	0.4505000	134.51000		
0.3043000	126.50000	0.3943000	131.82000		
0.3486000	128.13000	0.3514000	130.26000		



APPENDIX D

**GOLD/PALLADIUM BIMETALLIC ALLOY
NANOCLUSTERS STABILIZED BY CHITOSAN AS
HIGHLY EFFICIENT AND SELECTIVE CATALYST
FOR HOMOCOUPLING OF ARYLBORONIC ACID**

1. Metal contents for Au/Pd catalyst

A series of chitosan stabilized bimetallic Au/Pd catalyst was determined the exact Au and Pd concentration (mM) by ICP-AES. The results are shown in Table D-1.

Table D-1 Analysis of metal contents of chitosan stabilized bimetallic Au/Pd catalyst by ICP-AES techniques.

Catalyst	Initial loading (mM)		Metal contents analyzed by ICP-AES (mM)	
	Au	Pd	Au	Pd
Au:chit	0.50	-	0.50 ± 0.07	-
Au _{0.46} Pd _{0.04} :chit	0.45	0.05	0.46 ± 0.04	0.04 ± 0.04
Au _{0.43} Pd _{0.07} :chit	0.42	0.08	0.43 ± 0.03	0.07 ± 0.06
Au _{0.41} Pd _{0.09} :chit	0.40	0.10	0.41 ± 0.02	0.09 ± 0.06
Au _{0.39} Pd _{0.11} :chit	0.37	0.13	0.39 ± 0.05	0.11 ± 0.02
Au _{0.36} Pd _{0.14} :chit	0.35	0.15	0.36 ± 0.03	0.14 ± 0.01

2. Kinetics of the reaction with phenylboronic acid using a series of chitosan stabilized bimetallic Au/Pd hydrosol

Figure D-1 shows the time dependent catalytic reactions of phenylboronic acid using catalyst with different Au/Pd ratios. The products in each time intervals were analyzed by GC. Hexadecane was used as internal standard for the calculation of yields.

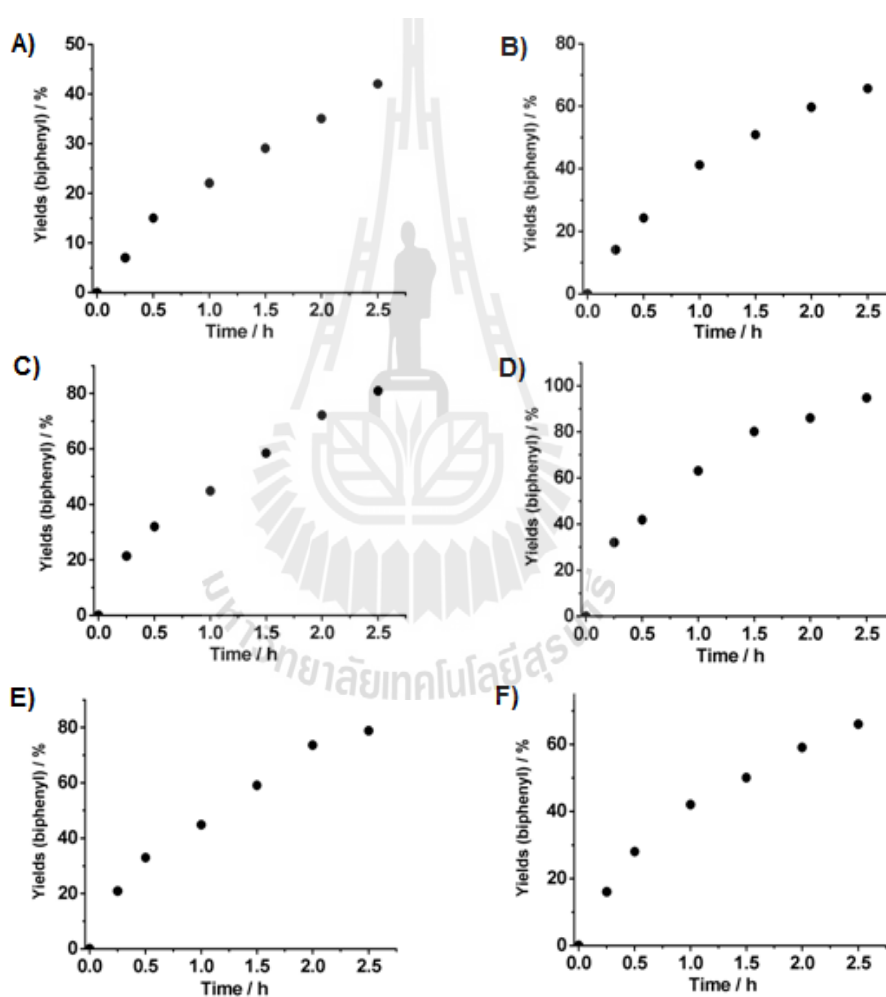


Figure D-1 Plot of biphenyl yields versus reaction time intervals using catalyst with different Au/Pd ratios. (A) Au/chit, (B) Au_{0.91}Pd_{0.09}/chit, (C) Au_{0.86}Pd_{0.14}/chit, (D) Au_{0.81}Pd_{0.19}/chit, (E) Au_{0.77}Pd_{0.23}/chit and (F) Au_{0.72}Pd_{0.28}/chit.

Figure D-2 shows the time course of conversion of phenylboronic acids by using catalyst with different Au/Pd ratios. The rateconstant was estimated from the slope of $-\ln(1-C)$, where C is conversion of phenylboronic acids.

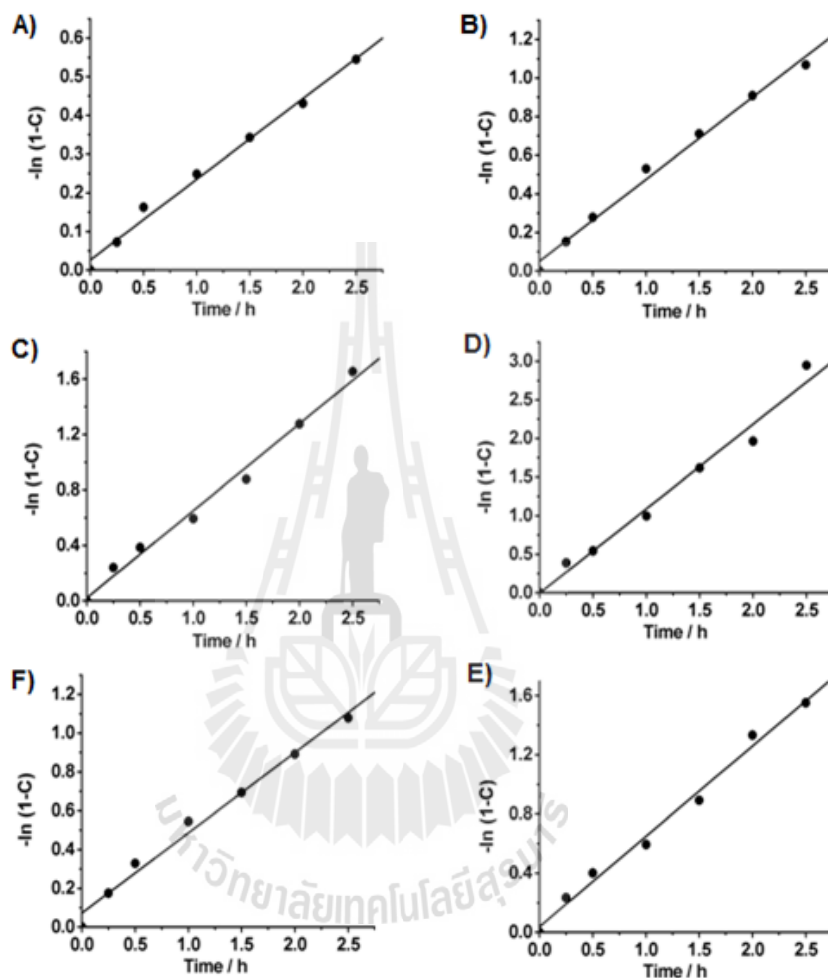


Figure D-2 Plot of $-\ln(1-C)$ against the time conversion of phenylboronic acid using catalyst with different Au/Pd ratios. (A) Au/chit, (B) Au_{0.91}Pd_{0.09}/chit, (C) Au_{0.86}Pd_{0.14}/chit, (D) Au_{0.81}Pd_{0.19}/chit, (E) Au_{0.77}Pd_{0.23}/chit and (F) Au_{0.72}Pd_{0.28}/chit.

3. Kinetics and Hammett plot analysis of the reaction with *p*-substituted arylboronic acid using Au_{0.81}Pd_{0.19}/chit as a catalyst

Figure D-3 shows the time dependent catalytic reactions of *p*-substituted arylboronic acid using Au_{0.81}Pd_{0.19}/chit as a catalyst. Yields of biphenyl products were analyzed by GC. Hexadecane was used as internal standard to calculate the yields.

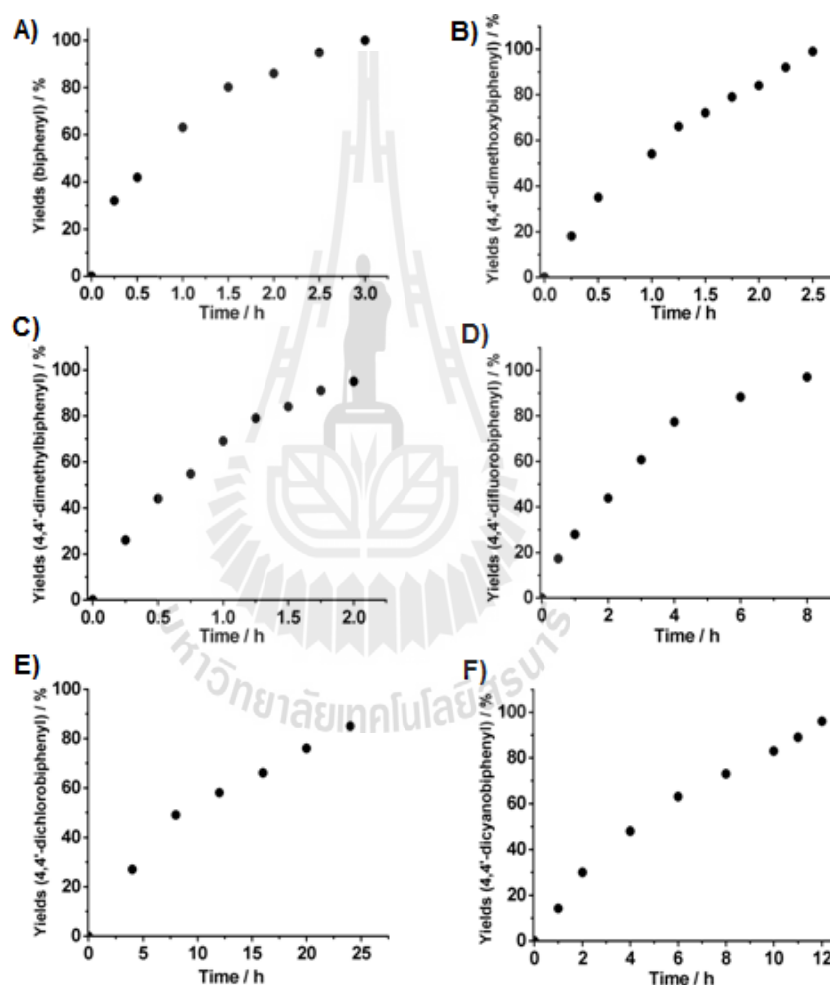


Figure D-3 Plot of yield of the biphenyl products versus reaction time intervals by using Au_{0.81}Pd_{0.19}/chit as a catalyst. (A) phenylboronic acid, (B) *p*-methoxy phenylboronic acid, (C) *p*-methyl phenylboronic acid, (D) *p*-fluoro phenylboronic acid, (E) *p*-chloro phenylboronic acid and (F) *p*-cyano phenylboronic acid.

Figure D-4 shows the time course of conversion of *p*-substituted phenylboronic acids. The rate constant was estimated from the slope of $-\ln(1-C)$, where *C* is conversion of *p*-substituted phenylboronic acids. Hammett plots were obtained by plotting $\ln k/(h-1)$ against σ – or σ constants (Murugadoss, A. and Sakurai, H., 2011).

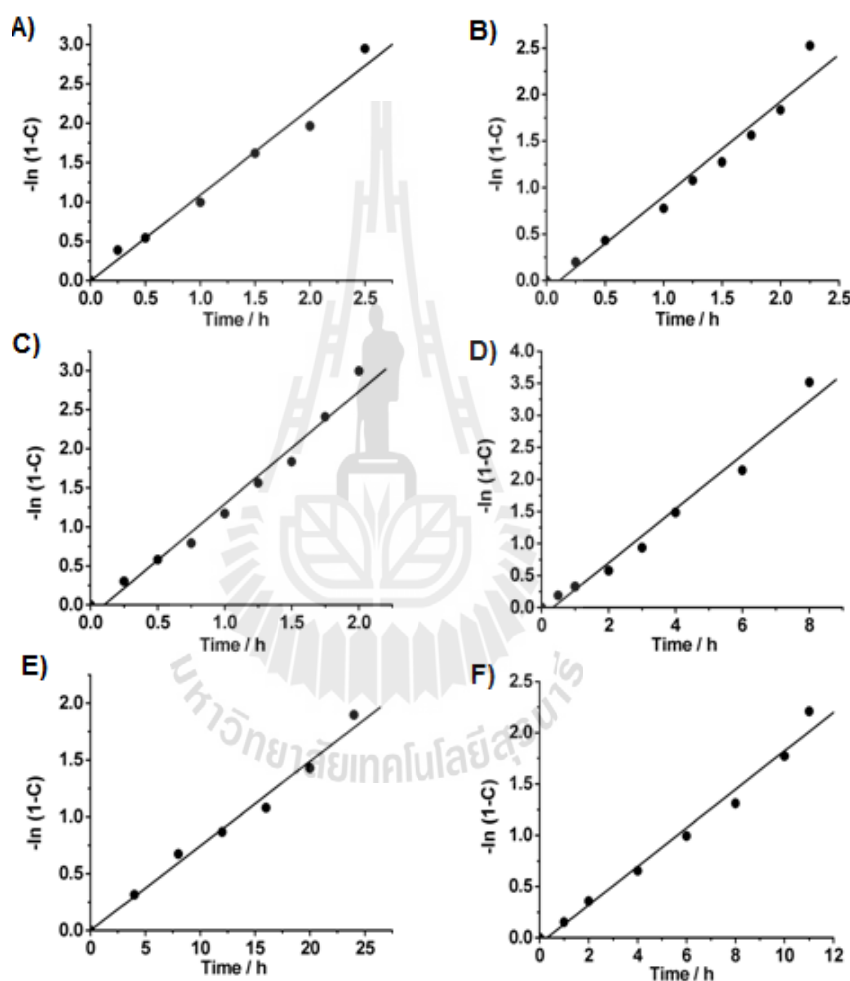


Figure D-4 Plot of $-\ln(1-C)$ against the time conversion of *p*-substituted phenylboronic acids using $\text{Au}_{0.81}\text{Pd}_{0.19}/\text{chit}$ as a catalyst. (A) phenylboronic acid, (B) *p*-methoxy phenylboronic acid, (C) *p*-methyl phenylboronic acid, (D) *p*-fluoro phenylboronic acid, (E) *p*-chloro phenylboronic acid and (F) *p*-cyano phenylboronic acid.

Reference:

Murugadoss, A. and Sakurai, H. (2011). Chitosan-stabilized gold, gold–palladium, and gold–platinum nanoclusters as efficient catalysts for aerobic oxidation of alcohols. **Journal of Molecular Catalysis A: Chemical**. 341: 1-6.

The Hammett substituent constants were taken from reported literature: Hansch, C., Leo, A., Taft, R. W. (1991). A survey of Hammett substituent constants and resonance and field parameter. **Chemical Reviews**. 97: 165-195.



CURRICULUM VITAE

ONSULANG SOPHIPHUN

Address:

18 Moo 11, Klangarwut road, Muang District, Ubonratchatane, Thailand, 34000

E-mail Onsulang_111@hotmail.com

Education

2009 B. Sc. (Chemistry) Second class honors, Ubonratchatane University, Thailand

2009 – 2015 Ph. D. student in Chemistry, Suranaree University of Technology, Thailand

Scholarships

2006 – 2009 Thai Science Scholar Project (TSSP) of Thai government

2009 – 2014 The Program Strategic Scholarships for Frontier Research, the Office of the Higher Education Commission, Thai government

2011 JENESYS Programmed by the Japan Society for the Promotion of Science (JSPS).

Publication:

Sophiphun, O., Wittayakun, J., Dhital, R.N., Haesuwannakij, S., Murugadoss, A. and Sakurai, H. Gold/palladium bimetallic alloy nanoclusters stabilized by chitosan as highly efficient and selective catalysts for homocoupling of arylboronic acid, Australian Journal of Chemistry, 3 (2012) 1238-1243.